

ABSTRACT

Title of Document: AN EXPERIMENTAL INVESTIGATION ON
SOLUTE NATURAL CONVECTION IN A
VERTICAL HELE-SHAW CELL

Dana Ehyaei, Doctor of Philosophy, 2014

Directed By: Professor Kenneth T. Kiger
Department of Mechanical Engineering

An experimental analogue was developed to investigate instability propagation of a multicomponent fluid system in porous media. This type of flow pattern has been observed in a broad range of applications from oil enhanced recovery to geological storage of byproduct materials such as CO₂. The main focus of this study is on the engineering instrumentation and implementation of experimental measurement techniques in microfluidic systems, more specifically in a thin-gap device that is used as a model for a saturated porous medium. Initially, quantitative in-plane velocity measurement by means of particle image velocimetry (PIV) within thin gap devices subject to a large depth-of-focus and Poiseuille flow conditions is studied extensively. The temporal velocity measurement is then coupled with a simultaneous concentration measurement by means of LED induced fluorescence (LIF).

The primary obstacles to a reliable quantitative PIV measurement are due to the effects of the inherent wall-normal velocity gradient and the inertial migration of particles in the wall-normal direction. After quantification of both effects, a novel measurement technique is proposed to make quantitative velocity measurement in microfluidic systems and narrow devices by manipulating the particles to their equilibrium position through inertial induced migration. This single camera technique is significantly simpler and cheaper to apply comparing to the existing multi-camera systems as well as micro-PIV implementations, which are restricted to a small field-of-view. A demonstration of a reliable PIV measurement under appropriate parameter design is then discussed for diffusive Rayleigh-Bénard convection in a Hele Shaw cell.

For concentration measurements, the main difficulty of making LIF quantitative is its highly sensitive response to the experimental settings due to extreme sensitivity of the fluorescence to the environment factors and illumination conditions. A calibration procedure is required prior to performing any meaningful quantitative measurements. Additionally, the effect of photobleaching can be significant, which impairs the measurement as will be discussed later in further detail. Eventually after calibration and correction methods for velocity and concentration measurement techniques, a simultaneous PIV/LIF is performed to quantify the behavior of instability fingers in the developed experimental system.

AN EXPERIMENTAL INVESTIGATION ON SOLUTE NATURAL
CONVECTION IN A VERTICAL HELE-SHAW

By

Dana Ehyaei

Dissertation submitted to the Faculty of the Graduate School of the
University of Maryland, College Park, in partial fulfillment
of the requirements for the degree of
Doctor of Philosophy
2014

Advisory Committee:
Professor Kenneth T. Kiger, Chair
Assistant Professor Amir Riaz
Professor James Duncan
Professor Michael Zachariah
Professor Srinivasa Raghavan

© Copyright by
Dana Ehyaei
2014

Table of Contents

Table of Contents	ii
List of Tables	iii
List of Figures	iv
Chapter 1: Introduction to the problem.....	1
Problem statement.....	1
Literature review	5
Chapter 2: Velocity measurement in narrow channels	11
Introduction.....	11
Experimental and simulation procedure	23
Result and discussion.....	31
Effect of non-uniform velocity with uniform tracer concentration	31
Effect of non-uniform tracer concentration	39
Interpretation of Roudet et al. (2011)	45
Possible solutions.....	46
Chapter 3: Rayleigh-Benard convection in Hele Shaw cell.....	49
Problem statement.....	49
Design parameters.....	55
Chapter 4: Quantitative concentration measurement in Narrow Channels	58
Experimental setup.....	58
Caliberation procedure.....	66
Data Reduction.....	69
Chapter 5: Simultaneous Velocity and Concentration measurements of Rayleigh Benard convection in Hele Shaw	75
Result and discussion.....	75
Chapter 6: Final Thoughts	94
Conclusion	94
Ideas for future	98
Appendix A.....	100
Bibliography	101

List of Tables

Table 4.1 diffusion coefficient for different species present in the fluid mixture in water	61
Table 5.1 experimental parameters	79

List of Figures

Figure 1.1 enhanced oil recovery using CO ₂	4
Figure 1.2 a schematic of CO ₂ solution trapping in saline aquifers and the effect of cap rock	4
Figure 1.3 a schematic of a reservoir	6
Figure 1.4 the density of methanol and ethylene-glycol (MEG) mixed with water, for MEH solutions with 61% (weight percent) ethylene-glycol	9
Figure 2.1 sample of correlation map for one interrogation window of a unidirectional flow (figure from synthetic images with number of particles of $N_I=9$)	14
Figure 2.2 schematic of a volumetrically illuminated narrow channel, illustrating the variability in velocity due to random location of particles across the gap	15
Figure 2.3 (a) micro-PIV implementations; in its simplest form it includes a volumetric illumination of the test setup, a microscope and a suitable objective lens to capture the motion of markers within a narrow region of the device (δz) (b) a schematic of defined depth-of-field and depth-of-correlation in micro-PIV implementations	19
Figure 2.4 the physical system of microsphere migration within a channel	21
Figure 2.5 three different criteria for velocity profile and particle concentration distribution across the gap	23
Figure 2.6 a schematic of the single component flow setup for large field of view PIV	26
Figure 2.7 (a), (b), (c) are samples of correlation maps while (d) is the calculated ensemble average correlation map	29
Figure 2.8 middle slice of the correlation map for different particle sizes from simulation in comparison with autocorrelation of particle images used in experiments	29
Figure 2.9 synthetic particles (a) $d_\tau=4$ [px], (b) experimental images, (c) $d_\tau=10$ [px]	30
Figure 2.10 (a) Probability distribution function of streamwise displacements for a Poiseuille flow, sampled across the wall-normal direction. (b) autocorrelation of	

experimental particle images (c) convolution of the autocorrelation with flow displacement PDF	33
Figure 2.11 ensemble average of correlation maps for a uniformly sampled Poiseuille flow (particle image size, $d_\tau = 4$ pixels, maximum displacement $\Delta x_m = 25$ pixels) measured in experiments at $x' = 5 \times 10^6$, and given by the convolution of the particle image autocorrelation function with the theoretical distribution shown in figure 10.2a. Displacements are normalized by the peak centerline displacement	33
Figure 2.12 PIV interrogation correlation function as a function of particle image size for a) large centerline displacements ($\Delta x_m = 15$ pixels) and b) small displacements ($\Delta x_m = 1$ pixel). c) PIV displacement estimate scaled with centerline velocity, ($\Delta x_{piv} / \Delta x_m$) as a function of particle image size d_τ and maximum displacement, Δx_m , for uniform tracer particle concentration	37
Figure 2.13 Valid detection probability for the displacement correlation peak as a function of the effective number of particle images within an interrogation window ($N_I F_I F_\Delta$). Note that three expected integer peak locations are tracked near the maximum displacement (no sub-pixel interpolation), and compared to the results of a uniform displacement (shown in red)	39
Figure 2.14 normalized averaged correlation functions, depicting their evolution due to combined effects of velocity gradient and particle concentration inhomogeneity, (a) experimental, (b) simulation	41
Figure 2.15 a) Streamwise alignment of tracer particles for large x' values. The effect of the directional arrangement of tracer particles on the experimental correlation peak in: b) stream- wise direction, c) lateral direction	44
Figure 2.16 illustration of hydrodynamic focusing	48
Figure 3.1 a schematic of the experimental setup for velocity measurements in Hele shaw cell. The pressure tanks were designed to hold a deformable cup inside them to hold the seeded fluids. Details of the setup can be found in appendix A	50
Figure 3.2 schematic of the test setup for diffusive Rayleigh-Bénard convection a) (MEG 61 wt% is shown in green and water in the bottom layer is transparent). b) Image of convective fingering instability, 1000 seconds after isolation	52

Figure 3.3 (a) instantaneous velocity field, (b) a more focused view of velocity field and (c) vorticity field for the diffusive Rayleigh-Bénard convection with large depth of field PIV ($Ra_\delta \approx 3$, $\delta = 0.127 \text{ mm}$)	54
Figure 3.4 (a) interrogation window size as a function of Hele-Shaw gap thickness (b) required development length needed during filling to ensure Case III conditions as a function of Hele-Shaw gap thickness and particle size ($Re_c = 2.3$). Current operating conditions are noted by the red star. Dashed line indicates $d > 0.1 \delta$	56
Figure 4.1 a Jablonski diagram and corresponding spectra, demonstrating the fluorescence process: initial creation of an excited state by absorption and subsequent emission of fluorescence at a higher wavelength	60
Figure 4.2 (a) spectral characteristic of the LED (blue light; $\lambda_{\text{max}}=462 \text{ nm}$), (b) fluorescence properties of the dye ($\lambda_{\text{max-excitation}}=490 \text{ nm}$)	62
Figure 4.3 schematic of the experimental setup from above. Camera 1 is used for PIV measurements, and camera 2 records the fluorescence while the optical filter extracts the pumping light	63
Figure 4.4 the long-pass optical filter performance, cut-on of 515 nm	63
Figure 4.5 a schematic of the experimental setup.....	64
Figure 4.6 snapshot images of the field of view at $t=1000 \text{ s}$. image a from camera 1 is used for velocity measurements while the second image is used for fluorescence	65
Figure 4.7 effective fluorescence for Fluorescein in water.....	68
Figure 4.8 effective fluorescence for Fluorescein in MEG 61%	68
Figure 4.9 different fluorescence behavior of the dye in different solvents	69
Figure 4.10 (a) averaged offset image (cell filled with pure water) \bar{I}_{offset} (b) averaged maximum intensity image (MEG and uniform dye concentration of 0.05 (mg/ml)); \bar{I}_{max} (c) raw instability image $I_1(\vec{x}, t = 0)$	71
Figure 4.11 a sample of measured concentration field at $t^* = 1000$ seconds	74
Figure 4.12 (a) mean concentration over region 2; \bar{c}_2 , (b) a focused view of \bar{c}_2 demonstrating its periodic behavior, (c) mean concentration over region 3 \bar{c}_3	73
Figure 5.1 a focused view of the Hele shaw cell cross section. The microspheres are manipulated to a known location across the gap before reaching to the field of view	75

Figure 5.2 calculated velocity and concentration from processing recorded images from camera 1 and 2 respectively	77
Figure 5.3 mapping raw images from camera 1 to corresponding images taken from camera 2 after transformation	78
Figure 5.4 Rayleigh-Bénard flow evolution obtained from LIF concentration measurements	80-86
Figure 5.4 interface tracking by thresholding ($c_f=0.8$).....	88
Figure 5.5 temporal fingers generation profile at the interface (a) ($0 < t < 22$) (b) ($0 < t < 7.5$)	88-89
Figure 5.6 normalized amount of MEG convecting into the reservoir	89
Figure 5.7 normalized volumetric flow rate of the MEG convecting. The maximum rate of interface retraction reaches to $2 \mu\text{m/s}$	90
Figure 5.8 vorticity field extracted from velocity measurement (a) and concentration measurement (b) at $t^*=1000$ seconds	91
Figure 5.9 dominant wavenumber of the instability plumes at different heights (except the red curve that corresponds to the wavenumber at the interface all the other plots are associated with a fixed vertical positions down the reservoir)	92
Figure 5.10 energy spectrum associated with Fourier transform of the averaged vorticity field.....	93
Figure 5.11 Combined dominant mode extracted from the averaged vorticity fields	93
Figure 6.1 the proposed experimental setup to investigate the effect of a variable permeability	99

Chapter 1: Introduction

1.1 Problem Statement

Understanding the governing mechanisms and physics of multiphase fluid transport in porous media has remained a challenging problem in fluid dynamics research community despite its great interest in a wide range of industry applications such as hydrology, secondary oil recovery, filtration and storage of byproduct materials. Recently there has been a great interest in mixing process of carbon dioxide and brine following CO₂ injection in deep saline aquifers as a reliable means of long term storage. Increasing concentrations of CO₂ in the atmosphere is believed to negatively affect the environment energy balance by increasing the greenhouse effect, thereby exerting a warming influence at the Earth's surface [1]. Therefore, the major motivation behind capturing and storage of CO₂ (CCS; Carbon Capture and Storage) is to reduce CO₂ emission and eventually its long term isolation from the atmosphere.

The primary sources of carbon dioxide production are big industrial processes such as power plants, cements production companies and refineries. The emitted CO₂ from these firms is concentrated at high pressure and transported to a nearby storage site. Pipelines are the most common transportation method, while other methods such as ship transportation, road or rail tankers are also considered depending on the volume of CO₂ being transported as well as the distance to the storage site. There are three primary storage types that are of interest for current use: oil and gas reservoirs, deep saline formations and unmineable coal beds. In all cases, CO₂ is injected into a porous rock formation below the earth's surface that is capable of holding the fluid in

place for long duration of time. This process is currently done both onshore and offshore. In case of sequestration within oil reservoirs, the sequestered CO₂ can also be used to enhance oil recovery from oil fields (EOR) (figure 1.1). The other option is to inject CO₂ into suitable coal fields where it will be adsorbed to the coal and will be held in place permanently. Finally and perhaps most significantly, there are vast and deep saline formations that can be used as a suitable storage site. In these aquifers salt water has been locked up by rock formation called “cap rock,” for long durations of time. This cap rock effect acts as a thick and low permeability cover to provide a restraint for the injected CO₂ preventing it from leaking back [2].

To ensure technical feasibility as well as long term stability of the storage reservoir, various aspects of the problem need to be addressed. When CO₂ is injected into an aquifer, it forms an immiscible CO₂-rich supercritical phase, while small amount of CO₂ dissolves in the brine [3]. In the temperature and pressure range encountered in geological CO₂ storage, the density of the supercritical CO₂ is less than the density of the brine; the result is its accumulating on top of the brine [4]. As the two fluids undergo diffusive mixing at the interface, a thin boundary layer develops that is heavier than either of the fluids. At some point this layer becomes gravitationally unstable and results in the onset of convective plumes. This phenomena results in an increase in the bulk mixing of the two layers due to shortening of the effective diffusion length scales by increasing the total interface area along with carrying rich CO₂ plumes into contact with fresh brine water. This process is called solution trapping of CO₂. The favorable outcome of this

phenomenon is a more stable system and a successful long-term entrapment of CO₂ (figure 1.2).

The current work is motivated by a goal to obtain quantitative temporally-resolved velocity and concentration measurements of diffusive Rayleigh-Benard convection observed in the process of solution trapping. For this purpose a laboratory experimental model was designed containing an analogous working fluid system in a mathematical equivalent geometry of two-dimensional homogeneous porous media (Hele Shaw cell) to produce the mixing behavior of CO₂ in brine. In this study, a combined particle image velocimetry (PIV) and LED-induced fluorescence (LIF) technique were used to provide velocity and concentration fields simultaneously. The primary goal would be to estimate the scalar flux density ($\vec{J} = \vec{J}_{convection} + \vec{J}_{diffusion} = \vec{u}c - D\nabla c$). In chapter 2 challenges associated with performing a reliable velocity measurement in narrow channels and microfluidic systems are introduced and a practical guideline is proposed to make PIV quantitative for these cases. In the succeeding chapters, the velocity measurement is accompanied by simultaneous concentration measurements. More specifically, in chapter 4, the instrumentation and calibration procedure for determining the concentration field from fluorescence is discussed. The measured velocity and concentration field is then used to investigate the physics of the flow mechanisms governing the instability growth and propagation in chapter 5. The final chapter (Chapter 6) includes the conclusion of the work as well as ideas for future work on the subject and instrumentation.

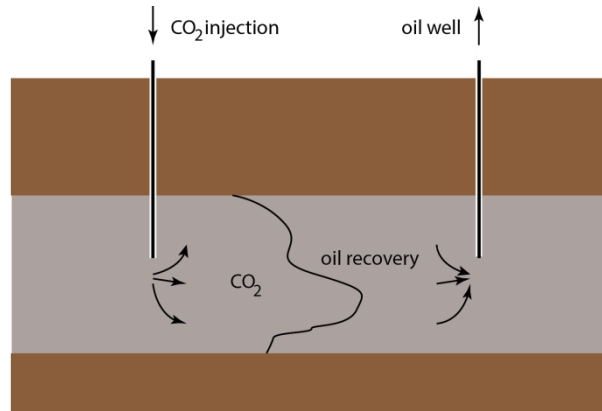


Figure 1.1 enhanced oil recovery using CO₂

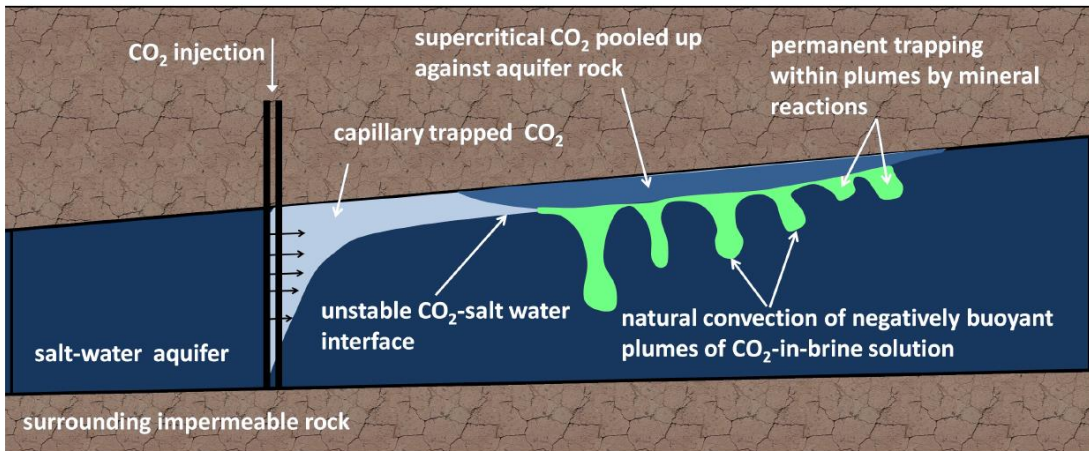


Figure 1.2 a schematic of CO₂ solution trapping in saline aquifers and the effect of cap rock (Riaz et al)

1.2 Literature Review

The equations describing the convection behavior of the dissolved CO₂ in the brine within porous media are:

$$\nabla^* \cdot \vec{u}^* = 0 \quad 1.1$$

$$\vec{u}^* = -\frac{K}{\mu} (\nabla^* P^* - \rho g \hat{y}) \quad 1.2$$

$$\phi \frac{\partial c}{\partial t^*} = -\vec{u}^* \cdot \nabla^* c + \phi D \nabla^{*2} c \quad 1.3$$

$$\rho = \rho_0 + \Delta \rho c \quad 1.4$$

$$\rho = \rho_0 + \Delta \rho c \quad 1.5$$

$$\mu = \mu_0 + \Delta \mu c \quad 1.6$$

Where \vec{u}^* is the velocity, K is the permeability, μ is the effective dynamic viscosity of the mixture, g is the acceleration due to gravity, D is the effective binary diffusivity of the two fluids, c is the saturation and ϕ is the porosity. Variables with the superscript * are dimensional and all others are non-dimensional, except for the obvious dimensional variables, ρ , μ , D , g , K and H . Now dimensionless variable are defined as below (figure 1.3):

$$U = \frac{K \Delta \rho g}{\Delta \mu} \quad 1.7$$

$$P' = \frac{\Delta \mu U H}{K} = \Delta \rho g H \quad 1.8$$

$$t' = \frac{\phi H}{U} = \frac{\phi H \Delta \mu}{K \Delta \rho g} \quad 1.9$$

$$\nabla = H \nabla^* \quad 1.10$$

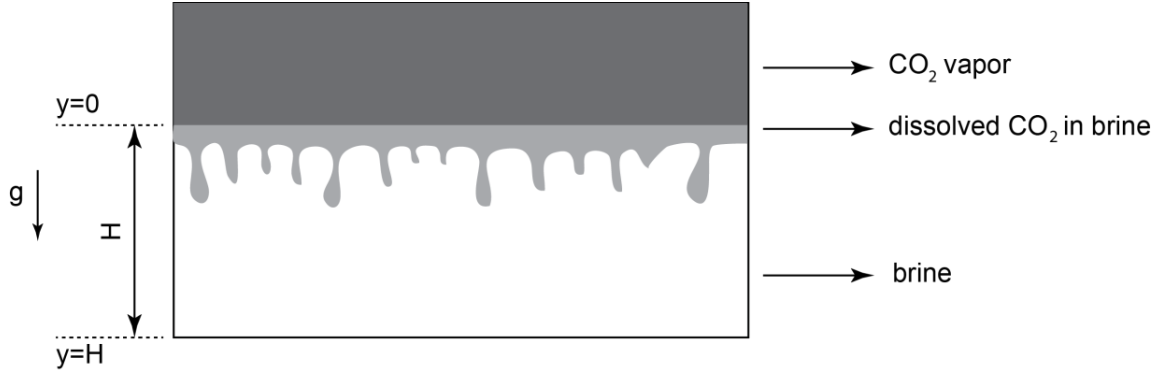


Figure 1.3 a schematic of a reservoir

Based upon the scaling variables defined above, equations 1.1-1.3 are reduced to:

$$\nabla \cdot \vec{u} = 0 \quad 1.11$$

$$\vec{u} = -\frac{\Delta\mu}{\mu} [(\nabla P - \frac{\rho_0}{\Delta\rho} \hat{y}) - c\hat{y}] \quad 1.12$$

$$\frac{\partial c}{\partial t} = -\vec{u} \cdot \nabla c + \frac{\Delta\mu}{\mu} \frac{1}{Ra} \nabla^2 c \quad 1.13$$

$$Ra = \frac{K\Delta\rho gH}{\phi D\mu} \quad 1.14$$

Where Ra , is the only dimensionless parameter governing the flow, which shows the relative importance of buoyancy to viscosity forces. Due to complexity of the system and variety of parameters involved, an analogous experimental model is used in this study to model the behavior of the flow. To be able to visualize the flow, a Hele-

Shaw cell is used as an analogue of porous media. This device that is formed by two flat plates of narrow gap δ can be shown to be equivalent to a two-dimensional homogeneous porous medium with permeability of $\delta^2/12$ ($\phi=1$). The Hele-Shaw cell is recognized as a convenient laboratory analogue to investigate geophysical fields, thermal convection and multiphase fluid displacement in porous media. In this section, Hele-Shaw flow is derived from Navier-stokes equation for single-phase, incompressible flow (neglecting external body forces):

$$\rho \frac{D\vec{u}}{Dt} = -\nabla P + \mu \nabla^2 \vec{u} \quad 1.15$$

Assuming that $w=0$ and provided that the rates of variation of u , v with respect to x , y can be neglected in comparison with their rates of variation with respect to z , equation 1.15 is reduced to:

$$\nabla^* \cdot \vec{u}^* = 0 \quad 1.16$$

$$\frac{\partial P}{\partial x} = \mu \frac{\partial^2 u}{\partial z^2} \quad 1.17$$

$$\frac{\partial P}{\partial y} = \mu \frac{\partial^2 v}{\partial z^2} \quad 1.18$$

$$\frac{\partial P}{\partial z} = 0 \quad 1.19$$

Equation 1.19 indicates that P is not a function of z and thereby, $\partial P/\partial x$ and $\partial P/\partial y$ are not functions of z either. Therefore equations 1.17 and 1.18 imply that u and v should be polynomials of degree two at most. Using the boundary conditions, the equations are reduced to:

$u, v=0$ for $z = -\frac{\delta}{2}, +\frac{\delta}{2}$:

$$u = \frac{1}{2\mu} \left(\frac{\partial P}{\partial x} \right) \left(z^2 - \frac{\delta^2}{4} \right) \quad 1.20$$

$$v = \frac{1}{2\mu} \left(\frac{\partial P}{\partial y} \right) \left(z^2 - \frac{\delta^2}{4} \right) \quad 1.21$$

The averaged velocity over the gap ($\bar{u}_i = \frac{1}{\delta} \int_{-\delta/2}^{\delta/2} u_i dz$) then is:

$$\bar{u} = -\frac{\delta^2}{12\mu} \left(\frac{\partial P}{\partial x} \right) \quad 1.22$$

$$\bar{v} = -\frac{\delta^2}{12\mu} \left(\frac{\partial P}{\partial y} \right) \quad 1.23$$

As can be seen from equations 1.22 and 1.23 the Hele-Shaw equation $\vec{u} = -(\delta^2/12\mu)\nabla P$ is similar to Darcy's law $\vec{u} = -(K/\mu)\nabla P$ that relates the flux (discharge per unit area, with units of length per time) and pressure gradient in a porous medium (k is the permeability of the medium). From Darcy's law, the flux divided by porosity gives the average velocity to account for the fact that only a fraction of the total formation volume is available for flow. Therefore the flow in Hele-Shaw cell is analogous to flow in a saturated porous media (porosity=1) with a permeability $k_{ij} = \delta^2/12$ ($i, j=1, 2$). For fluid transport in a Hele-Shaw cell, equation 1.2 reduces to:

$$\vec{u} = -\frac{\delta^2}{12\mu} \left[\nabla P + \rho \vec{g} \right] \quad 1.24$$

To reproduce the mixing behavior of CO₂ in brine, an analogue fluid system was used. The system contains the mixture of ethylene glycol and methanol (MEG) mixing with water [5]. The initial conditions for the experiment consist of the two

stably stratified stationary fluids of different density, which exhibit the property that the resulting mixture has a greater density than either two of the original fluids. As the two fluids undergo diffusive mixing at the interface, a thin layer develops that is gravitationally unstable, resulting in the onset of convective plumes and an increase in the bulk mixing of the two layers. MEG solutions containing less than 68 wt% ethylene-glycol are less dense than water, but the density of MEG-water mixtures exceeds that of water, with a maximum about 45 wt% MEG, dependent on the ethylene-glycol content of the MEG mixture. In this study MEG 61 wt% is used due limited design freedom as will be discussed in chapter 3.

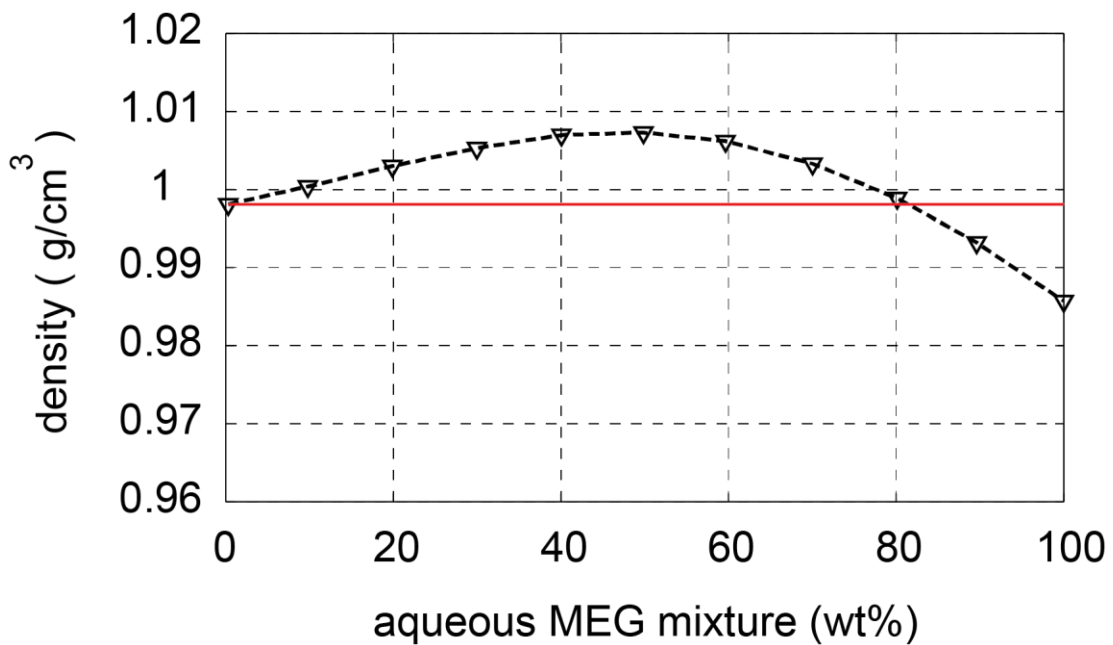


Figure 1.4 the density of methanol and ethylene-glycol (MEG) mixed with water, for MEG solutions with 61% (weight percent) ethylene-glycol (Neufeld et al 2010)

In a previous work by Backhaus et al. (2011) [6], a similar experimental model was developed consisting of a water column locating vertically above propylene glycol

(PPG) in Hele-Shaw geometry. The concentration field was then visualized by optical shadowgraph and the normalized mass flux (Nu) based on the amount of water being mixed was extracted from the interface erosion rate. Tests were conducted under different conditions, and the bulk mixing rate was reported for different Ra . Based on the permeability of each specific reservoir (different K), the mass flux was then estimated by calculating Ra . Backhaus et al. (2011) proposed a power-law in the form of $Nu = (0.045 \pm 0.025)Ra^{0.76 \pm 0.06}$:

$$Nu = \frac{\dot{m}}{\rho(D/H)\delta L} \quad 1.25$$

$$\dot{m} = \rho \dot{A} \delta \quad 1.26$$

$$Nu = Ra \frac{d(A/LH)}{dt} \quad 1.27$$

Previous investigations on the physics of gravity driven solubility trapping process have shown that convection does not start immediately when CO_2 is brought into contact with aquifer brine [7]. This delay time is suggested to be due to competing mechanisms of diffusive damping and the rate of growth of unstable perturbations.

A similar behavior was reported from experimental studies (Backhaus et al). However due to limited resolution of the experimental techniques this delay time scale could not be determined. The starting point for this study was to conduct large field of view velocity and concentration measurements to fill this gap in the literature.

In previous studies, a “critical time” for the onset of linear instability was proposed in by Riaz et al (2006) who used linear instability theory [8]

$$t_c^* = 146 \frac{\phi \mu^2 D}{(K \Delta \rho g)^2} \quad 1.28$$

Tilton et al [9] also looked at the onset of nonlinear instability and reported the solute flux magnitude in time:

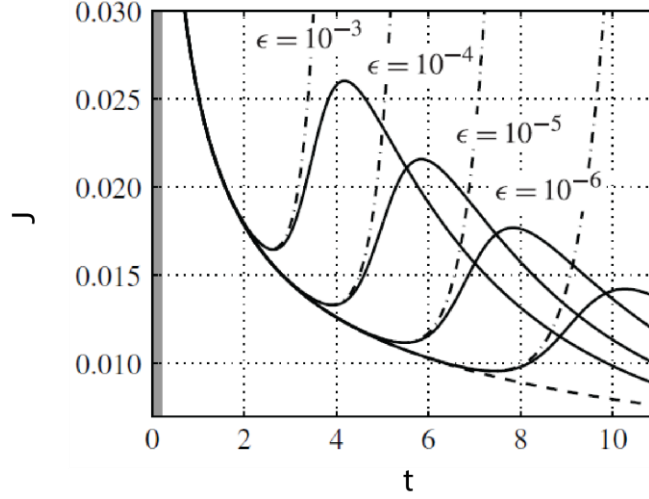


Figure 1.5 DNS calculations reporting the magnitude of solute flux with time for different initial perturbations (Tilton et al 2014)

In the current work, the novelty of the experimental measurement technique (simultaneous PIV-LIF) allows for the estimation of mixing rate as well as both the diffusive and advective fluxes:

$$\Phi_d = \frac{1}{A} \iint \mathcal{D}\nabla c \cdot \hat{n} dS \quad 1.29$$

$$\Phi_a = \frac{1}{A} \iint c' \vec{u}' \cdot \hat{n} dS \quad 1.30$$

$$c = \langle c \rangle + c' \quad \vec{u} = \langle \vec{u} \rangle + \vec{u}' \quad 1.31$$

The averaging operator is the spatial average over the area of interest.

Chapter 2: Velocity Measurement in Narrow Channels

2.1 Introduction

This section investigates the challenges associated with performing quantitative particle image velocimetry (PIV) in a planar thin-gap channel flow with a large field of view. Currently, velocity measurements in thin-gap flows are performed using microscopic-PIV with high magnification objectives that severely restrict the field-of-view. However a large field-of-view is required in certain microfluidic applications, where it is desired to examine a large region of the device rather than in a single channel; for instance, in biotechnology applications for measurements in microfluidic manifolds and cell culture devices, or systems investigating a blood vessel network [10]. In addition to microsystems, maintaining a large field-of-view is necessary in flow measurements within a Hele-Shaw cell. In this case, a large field-of-view becomes necessary to observe the evolution of the flow pattern within the device. After reviewing the problem in details and proposing a practical guideline to make PIV quantitative, the velocity measurement of the desired Rayleigh-Bénard instability flow pattern is demonstrated in the following chapter.

In a typical planar PIV measurement, fine tracer particles are added to a fluid that is illuminated by a thin light sheet. These tracer particles act as markers to illustrate the local flow pattern. The motion of these marker particles within the sheet is projected to a series of images through a lens camera imaging system. A local region of the image is selected (interrogation region), and the image pattern is correlated to the neighboring regions in the second image to find the statistically most

likely displacement for the small group of tracer particle images. The local fluid displacement is then estimated by locating the cross correlation peak at each spot or interrogation region. In order to perform a reliable measurement, it is critical for both the planar and depthwise displacement variations to be negligible within the interrogation volume. For this reason, in most cases the displacement variations are minimized either by refining the size of the interrogation windows or modifying the experimental setup such as the illumination sheet thickness [11].

Assuming that the tracer particles accurately follow the carrier fluid, their motions depict the local motion of the fluid.. The PIV algorithm is based on finding the maximum correlation for that interrogation region for consecutive intensity images on the same spot. More specifically, if the intensity values of an interrogation region is mapped to a random variable $x(k)$, where k represents elements in the interrogation window space, the problem is reduced to finding an interrogation region $y(k')$ on the second image that yields the highest correlation coefficient; $R(\vec{s})$. The local displacement in that spot at that instant t would be the distance from the two interrogation regions from the successive images that showed the largest correlation.

$$R(\vec{s}) = |\rho_{xy}| \quad 2.1$$

$$\rho_{xy} = \frac{C_{xy}}{\sigma_x \sigma_y} \quad 2.2$$

$$C_{xy} = \iint (x - \mu_x)(y - \mu_y) p(x, y) \quad 2.3$$

$$p(x, y) = \text{prob}[x(k) \leq x \text{ and } y(k) \leq y] \quad 2.4$$

$$\mu_x = \text{mean}[x(k)] \quad , \quad \sigma_x^2 = \int_{-\infty}^{\infty} (x - \mu_x)^2 p(x) dx \quad 2.5$$

The correlation coefficient ρ_{xy} is between -1 and +1 ($|C_{xy}| \leq \sigma_x \sigma_y$), therefore its absolute value lies between 0 and +1. If the highest calculated correlation is +1 then the two variables have a perfect correlation and on the other hand, if its value is zero, the two interrogated windows are not correlated at all. Theoretically if we consider a completely unidirectional, uniform flow, the correlation coefficient should return a value of +1. However, since there are always velocity variations at each interrogation volume, there wouldn't be a complete correlation and the estimated velocity would be an average of sampling marker velocities. In order to increase the reliability of the measured velocity at each spot, the processing algorithms and experimental parameters need to be designed accordingly to obtain the highest possible correlation coefficient.

As explained earlier, recorded images are interrogated via a subset of local windows (interrogation window); the size and shape of this window defines the extent of spatial averaging at that spot. For instance, a large interrogation window can lead to reduction in spatial resolution due to spatial averaging over a larger area and hence neglecting the smaller length scales of the flow. The accuracy of the measured velocity is also a function of number of particle images at each interrogation window. Too few particles due to insufficient tracer particle concentration or very small interrogation windows results in a lack of samples that produces a diminished signal to noise ratio and an increase in likelihood of spurious velocity vectors. A sample of interrogation region (64 [pixel] \times 64[pixel]), and a sample correlation map is demonstrated in figure 2.1.

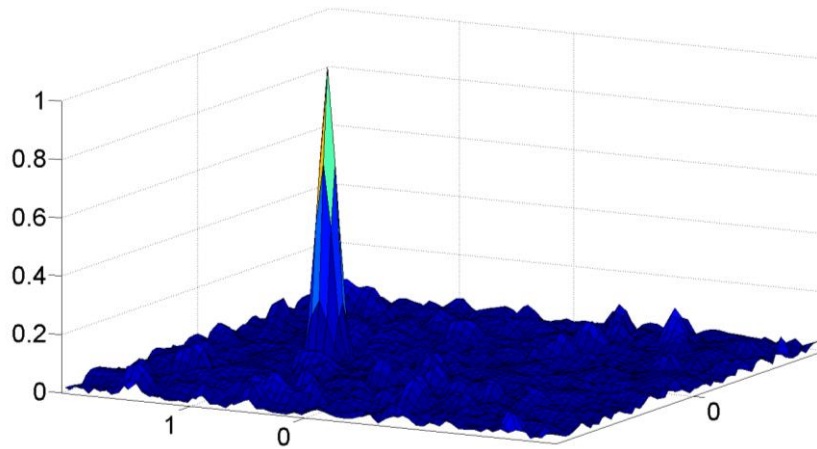
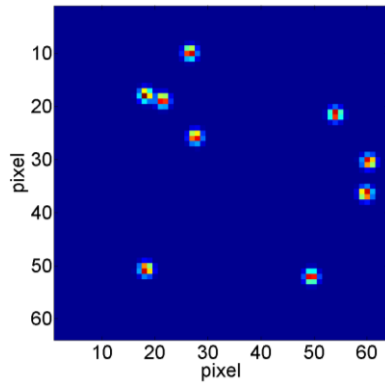


Figure 2.1 a sample of correlation map for one interrogation window of a unidirectional flow (figure from synthetic images with number of particle images of $N_I=9$)

Prior to interrogation optimization step, experimental design parameters can be modified to decrease the velocity variations being mapped on the image plane. This can be achieved by refining the optics to provide a narrower illumination sheet thickness to limit the out of plane velocity gradients. In some cases, providing a thin light sheet is not practical. One example is in micro-geometries or thin gap channel flows where optical access is limited to one axis or providing a laser sheet narrower

than the gap thickness is not practical. This problem is aggravated where the sheet thickness uniformity needs to be maintained over a relatively larger region of the device, as in the case of Hele shaw cell. Alternatively, in most of these cases the entire volume of the device is illuminated. This means that the tracer particle distributed across the entire gap of the device is illuminated. The local Poiseuille flow across the gap thickness, combined with the volume illumination, immediately implies a significant displacement variation within a single interrogation region (figure 2.2). As explained earlier, this displacement variation decreases the correlation peak amplitude that leads to a lower degree of confidence and more spurious vectors.

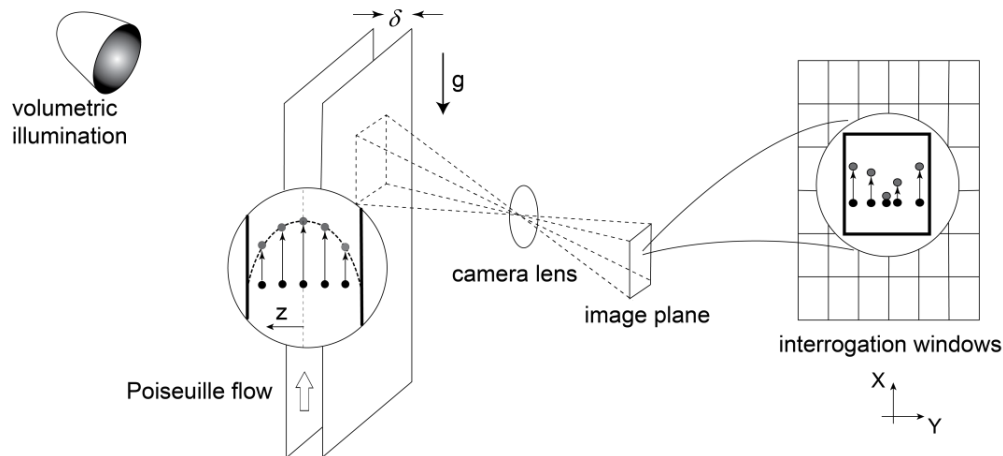


Figure 2.2 Schematic of a volumetrically illuminated narrow channel, illustrating the variability in velocity due to the random location of particles across the gap

In response, researchers started using micro-PIV to minimize the effect of displacement variations across the depth of the flow domain. In micro-PIV applications, a narrow depth of focus objective lens is used to set the thickness of the displacement distribution being sampled; (figure 2.3a) [12]. The depth-of-field is then

defined as a range in z-direction where the particle image size remains independent of z; equation 2.6. If δz is chosen narrow enough such that out-of-plane gradients (z-direction) are negligible, the entire local velocity profile can be quantified based on the relative location of the selected slice across the channel gap in addition to a prior knowledge of velocity profile distribution; in this case a parabolic velocity profile. In more complicated microfluidic devices, where there are 3 dimensional flows, this procedure needs to be repeated across the entire gap, scanning velocity magnitudes as a function of z-locations.

At high magnifications where a small depth-of-focus relative to the channel depth can be maintained, this implementation works well and extensive studies have been carried out successfully using this technique such as the work of Santiago et al. (1998). They studied the Pressure-driven Hele–Shaw flow in a 120 μm square flow field with a central cylindrical obstruction using 300 nm polystyrene particles. However, these methods are restricted to small field-of-views and will not work for cases where a large field-of-view is necessary. In order to enlarge the field-of-view, the magnification must necessarily be decreased that results in a larger depth-of-field and therefore larger velocity variations within each interrogation region due to significant velocity gradient in z-direction (with a constant sensor size d_s , field of view FOV has an inverse relationship with magnification $M_0 = FOV^{-1} \times d_s$). In addition, by increasing the depth of field, inevitably out of focus particles influence the measurement accuracy. In these cases, a “Depth of Correlation (*DOC*)” is defined to describe the thickness where particles contribute to the correlation map at each interrogation region. By decreasing magnification the *DOC* increases and introduces

a bias error due to the defocused particles and an extended depth of sampling volume. Therefore, to perform a reliable measurement an accurate estimate of *DOC* at a known wall-normal location within the device becomes necessary; equation 2.7 [13]. The theoretical equation for *DOC* values is reported for simple optical configurations (one objective lens) but different optical arrangements and additional instrumental features specific to each experimental setup (multiple lenses or possible immersion in oil), result in deviation of the actual *DOC* from its theoretical value [14]. In addition, preprocessing algorithms used on PIV images such as median filters and background subtraction might also affect the particle image characteristics and inevitably the effective *DOC* [15].

Kloosterman et al. (2011) [14] performed micro-PIV measurements with low magnifications in a round capillary (148 μm in diameter) for different types of microscopes. They considered two microscopes: a conventional inverted epifluorescent microscope in combination with different interchangeable objectives to obtain different magnifications (Zeiss, Axiovert 200) and an upright epifluorescent microscope with zoom function in combination with a single objective to obtain different magnifications (Leica MZ 16 FA). They reported that the measured velocity deviates with using different instrumentations and also that the measured velocity appears to be lower than the maximum velocity. According to their work, this underestimation of the maximum velocity for low-magnification measurements can get as high as 25%. This is with magnification of 3.5 and a field-of-view about 2 mm by 2.5 mm. For lower magnifications essential for obtaining a larger field-of-views as

needed for applications such as Hele-shaw cells and microfluidic systems, this implementation becomes problematic, considering its complexity and inaccuracy.

For relatively lower magnifications, it is much more convenient to set the depth of field of the system δz , larger than the channel gap spacing so that the tracer particles across the entire gap are mapped identically in the image plane ($\delta < \delta z$) and thereby eliminating the severe underestimation due to defocusing effect. The instrumentations can also be reduced to a single lens and camera system. However as it was explained earlier, in the implementation for current work, large velocity variation within each interrogation window is inevitable due to presence of a Poiseuille flow and needs to be addressed. The work in this section is focused on addressing how to conduct quantitative velocity measurements within planar thin-gap Poiseuille channel flows, subject to imaging conditions that require a large field-of-view. Specifically, this latter constraint is interpreted to mean that the magnification is small, $M < 1$, and the numerical aperture is also very small, $NA = 0.5/f\# \ll 1$.

$$\delta z = 4 \left(1 + \frac{1}{M_0} \right)^2 f^{\#2} \lambda \Rightarrow \delta z = 4 \left(1 + FOV^{-1} d_s \right)^2 f^{\#2} \lambda \quad 2.6$$

$$DOC = 2 \left[\frac{1 - \sqrt{\varepsilon}}{\sqrt{\varepsilon}} \left(f^{\#2} d_p^2 + \frac{5.95(M_0 + 1)^2 \lambda^2 f^{\#4}}{M_0^2} \right) \right]^2 \quad 2.7$$

where $f\#$ is the aperture number of the lens, d_p is the tracer particle diameter, M_0 is the magnification, λ is the wavelength of light scattered by the particle, and ε is a threshold value for the intensity of particle images that contribute to the measured spatial correlation (typically ε is chosen to be 0.01).

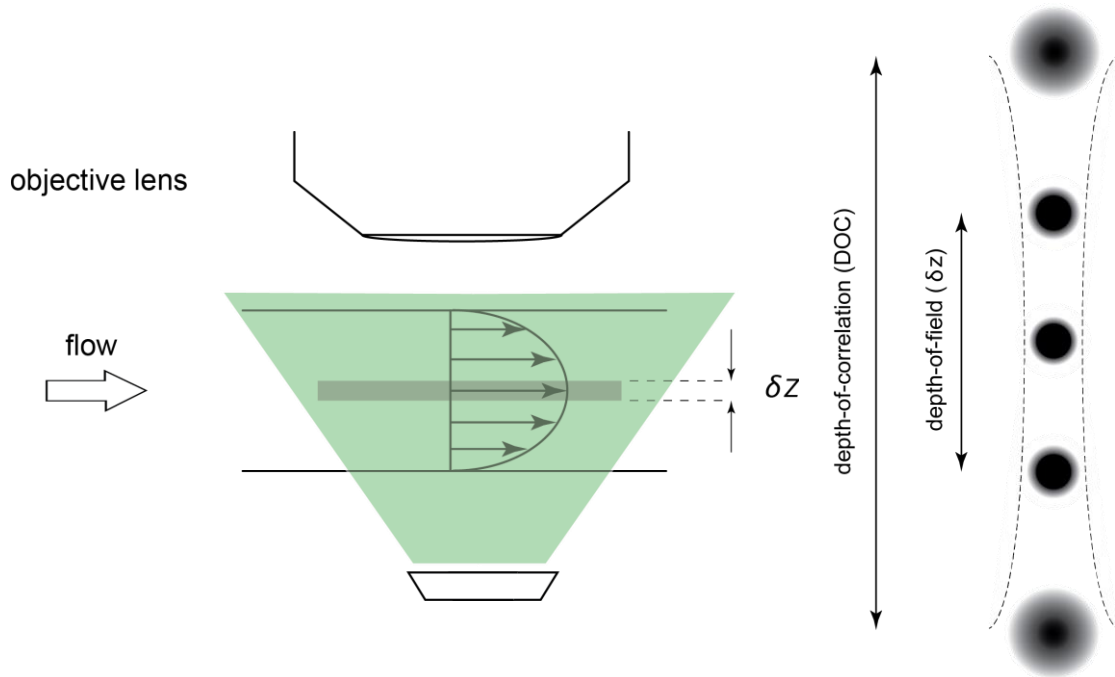


Figure 2.3 micro-PIV implementations; in its simplest form it includes a volumetric illumination of the test setup, a microscope and a suitable objective lens to capture the motion of markers within a narrow region of the device (δz) along with a schematic of defined depth-of-field and depth-of-correlation in micro-PIV implementations

As a final point, the influence of the gap velocity profile changes when particles migrate across the gap due to shear induced forces, producing a non-uniform sampling of the velocity distribution. In this case, accurate velocity estimation in micro-geometries and Hele-Shaw cell can become even more demanding where there is wall-normal particle migration across the gap. When the homogeneous mixture of fluid and the tracer particles are injected into the device, the convecting particles immediately start to migrate in the wall-normal direction until they reach a stable equilibrium position, as observed by Segre and Silberberg (1962) and later analytically predicted by Ho and Leal (1974) [16,17]. This migration is suggested to

be owing to lift forces acting on the particle due to small inertia and presence of walls [18].

The trajectory of the particles is illustrated in figure 2.4 from the theory developed by Ho and Leal. In their work the streamwise location (x') of a neutrally buoyant rigid sphere is related to its position across the channel (x' is normalized by a migration length X); equation 2.8.

$$x' - x'_0 = \int_{s_0}^s \frac{s''(1-s'')}{G(s'')} ds'' \quad 2.8$$

$$x' = \frac{x}{X} \quad 2.9$$

$$X = 36\pi\delta \left(\frac{\delta}{a}\right)^3 \text{Re}_c^{-1} \quad 2.10$$

$$\text{Re}_c = \frac{V\delta}{\nu} \quad 2.11$$

Where δ is the gap thickness and a is the radius of the spherical particles.

The normalized streamwise location variable (x') is used later in the result section to present the effect of this lateral migration on PIV correlation. In equation 2.8, s represents the wall normal position within the gap ($0 < s < 1$) and $G(s)$ was reported in their table 4. For neutrally buoyant particles and for $\text{Re}_c < 30$, the equilibrium position was reported to be 0.3δ from the centerline. For large Re_c , the equilibrium position migrates closer to the wall, as noted in the previous work by Asmolov (1999) [18].

Typically in PIV measurements within thin devices, neutrally buoyant particles are used for seeding the fluid to minimize the settling of tracers on the boundaries due to small scales of the device. However, any deviation in particle

densities results in a different equilibrium position across the channel. In addition to velocity variations discussed earlier, the inertial induced migration that results in significant particle concentration inhomogeneity across the gap makes a reliable PIV measurement even more demanding. Particle concentration inhomogeneity across the gap results in bias sampling of the velocity probability distribution function (*PDF*), which its effect needs to be investigated and is discussed in more details in the next section.

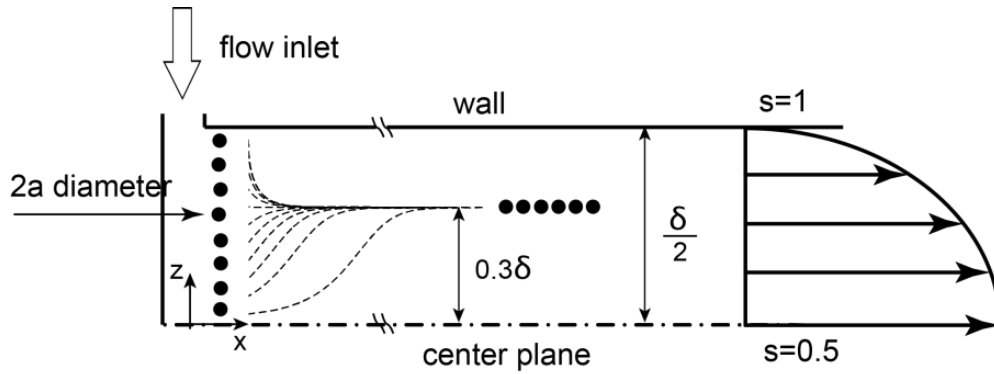


Figure 2.4 the physical system of microsphere migration within a channel

As mentioned above, the main difficulty in making quantitative measurements lies in the effects caused by the strongly non-uniform velocity gradient that exists across the gap, and the potential bias caused by the migration of particles in the wall-normal direction. This point has been recently documented and outlined by Roudet et al. (2011) [19], who demarked the possible flow conditions that can be encountered on the basis of a viscous diffusion time, T_p (which represents a time scale for the Poiseuille flow to become fully developed), and a particle migration time, T_m , all

given in reference to an initially quiescent and uniformly seeded fluid state. These key timescales were defined as:

$$T_p = \frac{(\delta/2)^2}{\nu} \quad 2.12$$

$$T_m = 2.66\pi \left(\frac{z_{eq}}{V} \right) \left(\frac{\delta}{a} \right)^3 Re_c^{-1} \quad 2.13$$

where δ is the gap width, ν the kinematic viscosity, V is the gap-averaged velocity, z_{eq} is the equilibrium migration position of the tracer particles, a is the particle radius, and $Re_c = V\delta/\nu$. The above scales were then used to define the following three regimes:

- 1) Case I: at short times when $t \ll T_p$, the flow across the width of the gap is still uniform, and the PIV measurement unambiguously returns this value.
- 2) Case II: when $t \ll T_m$, the migration of the particles has not had time to develop, regardless of the flow development. Roudet et al. (2011) observed empirically that their PIV interrogation returned a value close to the mean value of the wall-normal profile.
- 3) Case III: $t > T_m$ and $t > T_p$, implying that the particles have migrated to their equilibrium positions, and so the PIV measurement returns a velocity corresponding to the value given by the equilibrium position in the wall-normal Poiseuille profile.

Details of measurements using the Case I criterion is explained in Roig et al. (2012) [20]. In this study, they investigate the dynamics of a bubble rising in a Hele-Shaw cell. Since the time scale of the flow is small, they suggest a uniform flow

profile across the gap. The current work focuses on clarifying and quantifying the details associated with conducting experiments for conditions described by Case II and III (figure 2.5). In what follows, we first examine the effect of the non-uniform Poiseuille flow in the presence of a uniform concentration, followed by a subsequent accounting for the transient evolution of the particles. This is addressed by examining the effects of the particle image size, interrogation window size and maximum allowed displacement on the bias and random errors produced in the correlation function.

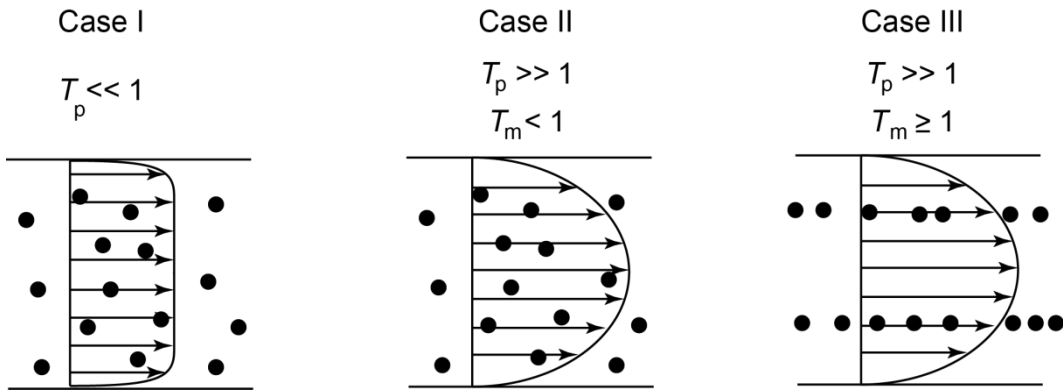


Figure 2.5 three different criteria for velocity profile and particle concentration distribution across the gap

2.2 Experimental and Simulation Procedures

Both PIV experiments and numerical simulations of a simple fully developed Poiseuille flow were conducted to quantitatively describe the effects of the non-uniform velocity and tracer concentration on the correlation function. Initially, the case II conditions are examined, where particles are uniformly scattered across the

gap, followed by the conditions leading to case III where the particles migrate partially or completely towards their equilibrium position.

The experiments were conducted using a vertically oriented Hele-Shaw cell, as shown in figure 2.6. The gap was formed by two rectangular tempered glass plates (12.7 mm thick), a U-shaped shim of known thickness (varying between 0.1 to 0.7 mm), and a supporting frame. The spacer was pressed between the plates by the steel frame, with a bolt spacing of 5 cm along the perimeter to ensure a uniform compression and a constant gap thickness. The shape of the gasket gave a fluid domain with a development length of up to $H = 457$ mm and a width of $W = 76.2$ mm. A precision syringe pump (NE-1000 X) was used to provide the device with a steady flow through a single inlet machined at the bottom of the cell, while the top boundary remained open to the atmosphere. To decrease the potential for particle migration in the feed system and manifold, a relatively short flexible tube was used for connecting the pump to the device (Inner diameter of 3 mm and length of 125 mm). The gap based Reynolds numbers were ranged between $0.7 < Re_c < 15$ for all experiments, where $Re_c = V\delta/\nu$.

Monodisperse Polystyrene microspheres (Phosphorex, #120) with a typical diameter of $d = 2a = 15$ μm and a standard deviation of less than 1.1 μm were used as tracer particles. These particles were nearly neutrally buoyant ($\rho_p/\rho_{\text{H}_2\text{O}} = 1.05$), and remained well dispersed in water. Polystyrene particles are commonly used in microscopic systems as marker tracers. The particles need to be chosen small enough to follow the flow faithfully without interfering with the flow field and clogging the microdevice. However, the particles must be large enough so that they scatter

sufficient light and also to dampen out Brownian motion. A first order estimate of the error associated with Brownian motion relative to the displacement in x-direction is given by Santiago et al. (1998) [12].

$$\varepsilon_B = \frac{1}{u} \sqrt{\frac{2D_b}{\Delta t}} \quad 2.14$$

Where D_b is the Brownian diffusion coefficient, u is the characteristic velocity, and Δt is the time delay. In microPIV implementations, typically, small fluorescent tracer particles, with a diameter of 0.1-0.5 μm are used. For instance, Meinhart et al. (1999) used fluorescently labeled polystyrene particles with diameters of 200 nm to measure the near-wall flow velocity in a microchannel [21]. In this study due to relatively larger size of the particles used, pure scattering was found to be sufficient and the effect of Brownian motion is negligible.

A camera (Phantom v640, sensor region used = 1080 x 1920 pixels, $d_r = 10$ μm pixel size) recorded images of a 35 x 62 mm region ($M_0=0.31$) using a zoom lens ($f\# = 8$) while a 600 W halogen light with a Fresnel collimating lens was placed approximately 2 m away on the far side of the Hele-Shaw cell, providing a uniform oblique forward scatter illumination of the entire flow volume. The depth of field of the system, δz was set larger than the channel gap spacing so that the tracer particles across the entire gap were mapped identically in the image plane as particle images in this region is dominated by refraction ($\delta z = 2.5$ mm).

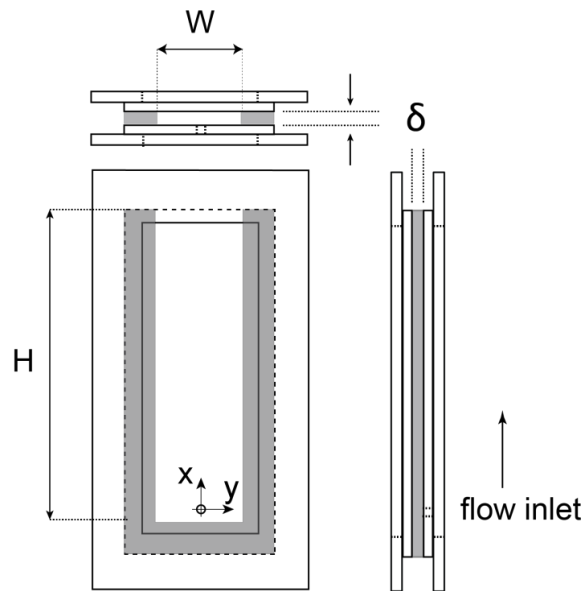


Figure 2.6 a schematic of the single component flow setup for large field of view PIV

The magnification and lens configuration gave particle images that were approximately 4 pixels in diameter, as measured by width of the autocorrelation function at a magnitude that is 15% of the peak value, and divided by $\sqrt{2}$ to account for stretching of the peak by the convolution process [11,15]. It should be noted that the autocorrelation map is constructed by determining the cross correlation of an interrogation window with itself. Since there is no displacement, the autocorrelation peak is just a representative of particle image size. As explained earlier, after the images are recorded they are interrogated into smaller sub-regions called “interrogation windows”. The choice for size and shape of this interrogation window need to be optimized for each specific case as it depends on various parameters. The aim is to obtain velocity information that is both reliable and accurate for the smallest possible interrogation window size, D_I [11]. The PIV interrogations were performed using a 100 x 140 pixel interrogation window, using a direct cross-correlation with

background subtraction and no image-shifting. The windows were selected to be longer in the direction of the flow in this case to increase the spatial resolution of the correlation map.

The results for the fully-developed Poiseuille flow were calculated using ensemble correlation averaging over a sample of $N = 300$ correlations to remove the effects of random correlation noise [22]. The instantaneous correlation maps contain significant amounts of noise that can lead to inaccurate or unreliable measurements. This noise can be significantly reduced by averaging the correlation maps from each interrogation region, and then determining the location of the signal peak location ;figure 2.7.

$$\langle R(\vec{s}) \rangle = \frac{1}{N} \sum R(\vec{s}) \quad 2.15$$

Initial simulations were conducted with particles scattered uniformly across the depth of the gap. For migrating flows, the analytical results of Ho and Leal were used to calculate the wall-normal location of each individual tracer particle (s), which was assigned to that particle. The location of this particle on the following images was then calculated from theory of Ho & Leal, allowing for a realistic and gradual migration to be observed. In those results where a converged average correlation function is examined, ensembles of effectively 10000 particles were used with a particle image density of 12. The autocorrelations from the experimental particles and synthetic images with different particle sizes are compared in figure 2.8. Since the autocorrelation is symmetric about the line of the mean displacement direction, only the central slice middle slice of the function is shown.

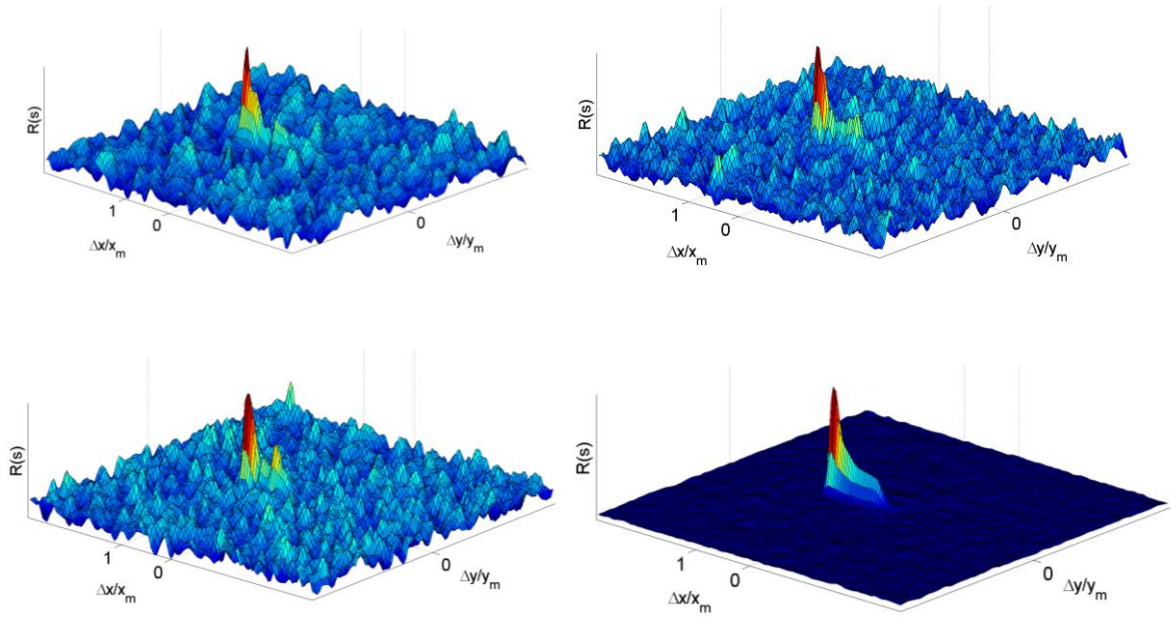


Figure 2.7 samples of correlation maps along with the calculated ensemble averaged map

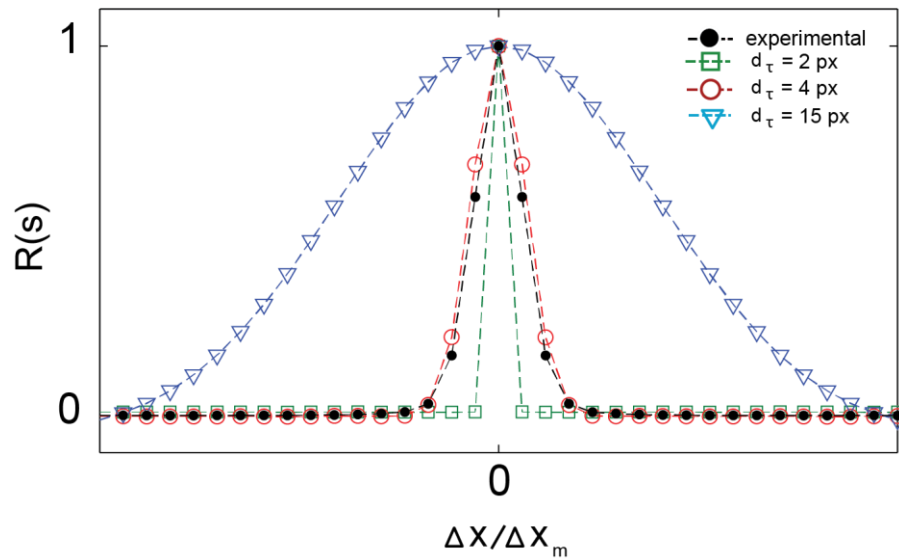


Figure 2.8 middle slice of the autocorrelation function for different particle sizes from simulation in comparison with autocorrelation of particle images used in the experiments

In this study the particle image diameter d_τ is determined by twice the distance from the location of Gaussian mean to where the intensity value of the Gaussian distribution is reduced to e^{-2} of the center. For the numerical simulations of the correlation function evolution, artificial PIV images need to be created with a known velocity distribution and a given particle image size and intensity. Each particle image is created individually by forming a square grid A_p of 65 by 65 pixels on the synthetic image (3200 by 3200 pix) with its center at $(X_0, Y_0)_P$ where the center of a particle image (P) is located. In-plane position of a particle image $(X_0, Y_0)_P$ is chosen randomly, resulting in a homogeneous concentration distribution everywhere on the image. The intensity field for a single particle in grid A_p was defined as follows:

$$I(X, Y) = \exp\left(\frac{-(X - X_0)^2 - (Y - Y_0)^2}{(\frac{1}{8})d_\tau^2}\right) \quad 2.16$$

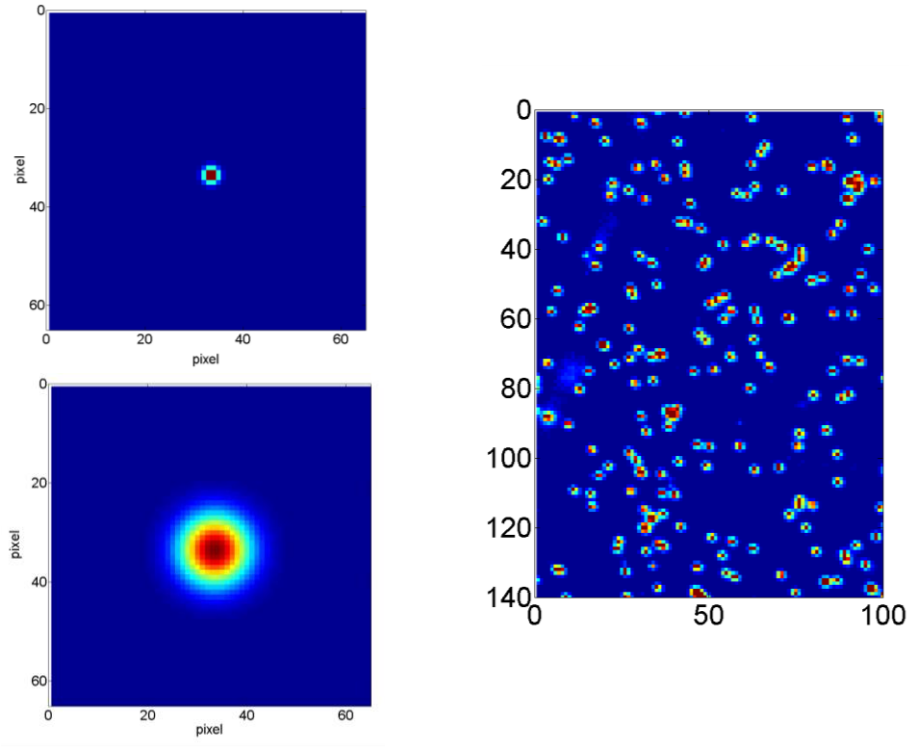


Figure 2.9 synthetic particles (a) $d_\tau=4$ [px], (b) experimental particle images, (c) $d_\tau=10$ [px]

2.3 Results and Discussion

2.3.1 The effect of particle size in the presence of non-uniform velocity and uniform concentration

The large variation in the displacement distribution due to the random sampling of velocities across the gap results in a bias of the of flow velocity Probability Distribution Function (PDF), as shown in figure 2.10. For a PIV interrogation, the correlation map function can be decomposed into three components.

$$R(\vec{s}) = R_C(\vec{s}) + R_F(\vec{s}) + R_D(\vec{s}) \quad 2.17$$

$$R_C(\vec{s}) = \left| \rho_{\langle x \rangle \langle y \rangle} \right| \quad 2.18$$

$$R_F(\vec{s}) = \left| \rho_{\langle x \rangle y'} \right| + \left| \rho_{x' \langle y \rangle} \right| \quad 2.19$$

$$R_D(\vec{s}) = \left| \rho_{x'y'} \right| \quad 2.20$$

The first component (R_C) is the correlation of the mean background intensity over the interrogation window pair. The second term (R_F) represents the correlation of the fluctuating intensity in the first interrogation window with the mean intensity of the second window and vice versa. Finally the displacement component (R_D) is the correlation of the fluctuating image intensities of the interrogation window pair. The highest peak in R_D corresponds to the displacement-correlation peak (equations 2.17-2.20). This component of the correlation function is often modeled as a convolution of the velocity PDF, the autocorrelation of the particle images, and a random noise component due to the limited number of particle samples within the interrogation volume (Olsen et al. 2000 [13]; Wereley et al. 2007 [23]). For an ensemble correlation interrogation of the flow (or conditions where a very large number of

particles existing within the interrogation window), this results in a correlation function that has a peak that is broadened due to the variation of the velocity PDF (see figure 2.10). Given these conditions, one would predict that the location of the correlation peak will represent the maximum velocity in the gap, as suggested by prior studies on the effect of velocity gradients on the correlation function (Wereley et al. 2007 [23]; Westerweel 2008 [24]), since the velocity maxima within the profile increases the likelihood of sampling velocities near the extrema magnitude. Both the experiments and numerical simulations confirm this fact (figure 2.11), which is in contrast to the observations given by Roudet et al. (2011), who reported that their measurements gave the gap-averaged velocity ($U_{piv} = 2V_{max}/3$), and not the peak value. We believe this discrepancy to be due to the fact that Roudet *et al.* were observing combined effects of a bias due to their particle image size and the early stages of particle migration, and that a much more stringent criterion for the particle migration time should be used to determine the boundary of the case II conditions. Details on this particular point will be discussed in the next section, which addresses the effect of non-uniform particle concentration.

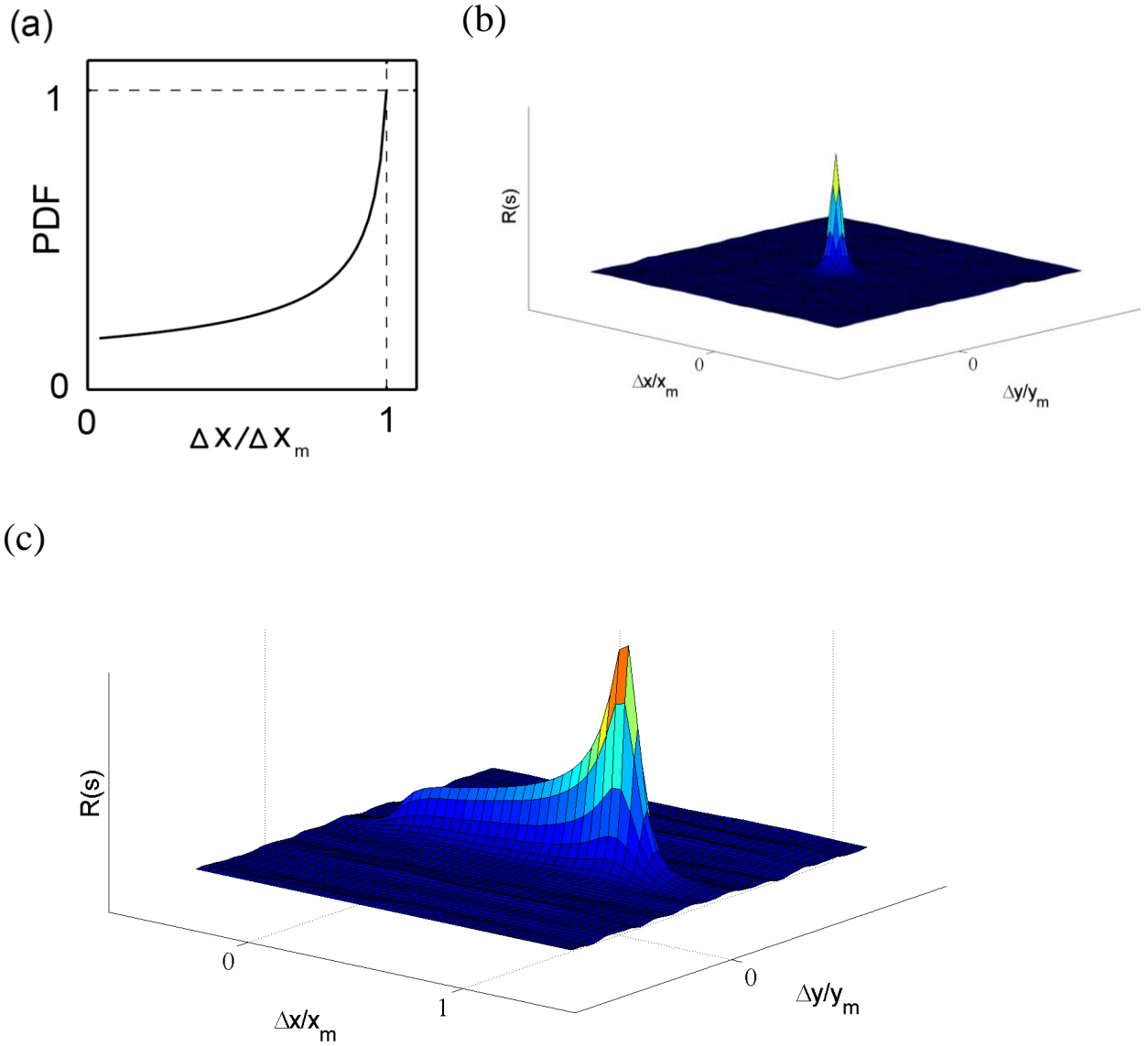


Figure 2.10 (a) Probability distribution function of streamwise displacements for a Poiseuille flow, sampled across the wall-normal direction. (b) autocorrelation of experimental particle images (c) convolution of the autocorrelation with flow displacement PDF

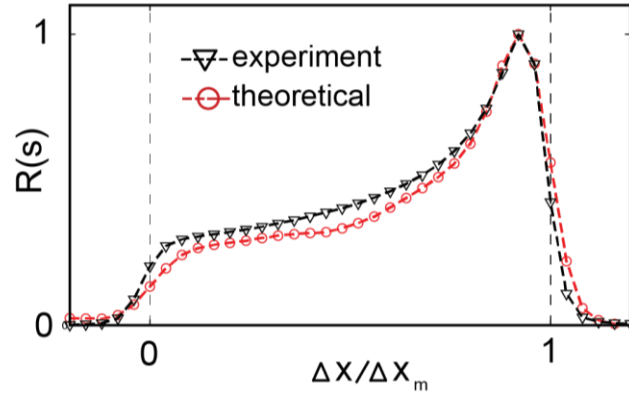


Figure 2.11 ensemble average of correlation maps for a uniformly sampled Poiseuille flow (particle image size, $d_t = 4$ pixels, maximum displacement $\Delta x_m = 25$ pixels) measured in experiments at $x' = 5 \times 10^6$, and given by the convolution of the particle image autocorrelation function with the theoretical distribution shown in figure 10.2a. Displacements are normalized by the peak centerline displacement

In examining the correlation functions shown in figure 2.11, it is immediately noticed that the convolution of the sampled velocity distribution with the particle images produces a broadening and shift in the location of the correlation peak towards slightly lower values than the true maximum displacement. This introduces a systematic bias in the measured value that will depend on the particle image size and the relative maximum displacement magnitude, which was explored using synthetic PIV images for a range of particle image size and relative displacements (figure 2.12). A small particle image size in comparison to the maximum displacement will provide the most accurate representation of the original velocity PDF, due to the minimal distortion this creates to velocity PDF. The larger the particle size in comparison to the maximum displacement, however, the greater the distortions of the PDF, introducing a bias shift in the effective peak location, as shown in figure 2.12a. For smaller relative displacement, the coarse discretization of the velocity distribution

results in a strong bias across even the smaller particle sizes (figure 2.12b). Note that Brownian motion would also tend to cause a broadening of the correlation function. In the current work, this effect has been neglected. A summary of particle-size bias error for a range of particle image size (d_r) and maximum displacement (Δx_m) is shown in figure 2.12c. For the largest displacement (red line with square symbols, $\Delta x_m=15$ pixels), the bias tends towards zero for the smallest particles sizes, and increases to just over 30% for a particle with an image diameter that is close to half the interrogation window size. Conversely, for small displacements (such as $\Delta x_m=1$ pixel or smaller) the bias error is such that the true peak is underestimated by 20 to 30% for all particle sizes.

Note that effects of particle imaging bias and non-uniform displacements on PIV interrogations have been reported previously by Fouras et al (2007) [25] and Kloosterman et al (2011) [14]. In the work of Fouras et al (2007), this effect was discussed in the context of x-ray PIV that has a depth-of-field very large in comparison to imaged flow, but with a velocity dependent particle intensity due to the exposure behavior of the x-ray imaging system. This produced a larger weighting to the slower moving particles in the distribution, which is significantly different from the current uniform-intensity observation conditions. Nevertheless, a similar effect due to particle size would be present, but was not discussed. This is most likely due to the fact that their particle image diameter was small and the maximum displacement was large ($d_r \sim 2$ pixels and $\Delta x_m \sim 64$ pixels), leading to errors of only a few percent.

In the work of Kloosterman et al (2011), a detailed analysis was performed on the particle imaging characteristics of two different microscope systems and its

resulting influence on the correlation functions interrogated from an axisymmetric Poiseuille flow. The work examined these effects across a range of magnification, spanning from $3 < M_0 < 38$, with a peak bias error due to the depth of correlation (DOC) reaching 25% for the low magnification images with the largest DOC (see figure 11 from Kloosterman et al 2011). The current study presented in figure 2.12 complements their results in that it expands the variables considered to include the nominal particle size and the displacement distribution, but for the more restrictive case of uniform particle size and intensity that one would expect from a large field-of-view imaging conditions. The closest case for comparison between our results and that of Kloosterman et al (2011) would be the case for “upright combi-microscope” imaged at magnifications of 3, 4, and 5, which had a DOC that was greater than or equal to their tube diameter. They reported particle image diameters of $d_r \sim 10-13$ pixels (product of 3 to 3.7 μm particle image size with $M_0=3.5$) for all three of these magnifications and adjusted their timing such $\Delta x_m \sim 10$ pixels for all cases. Their result of $\Delta x_m / \Delta x_{true} \sim 0.75$ is indicated in Fig 12.2c (shaded rectangle), which falls very close to the present results.

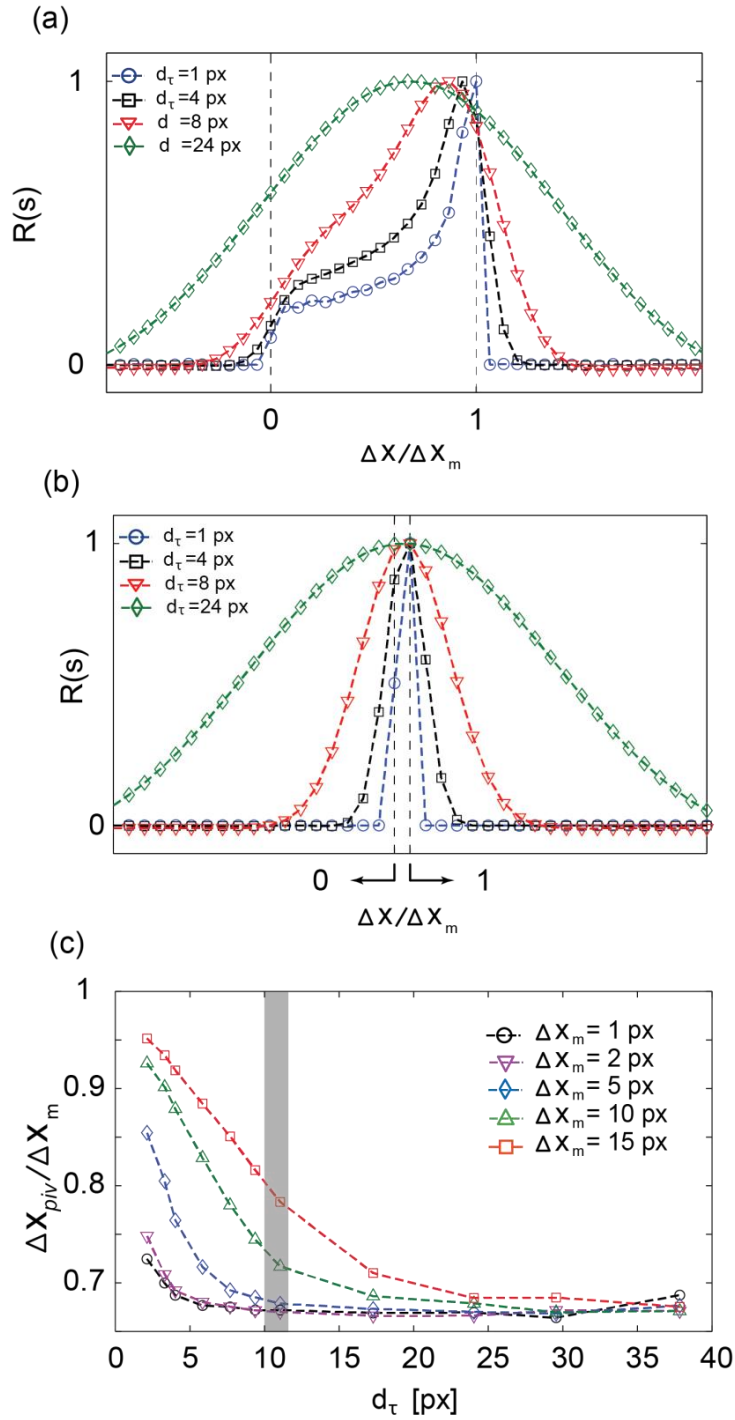


Figure 2.12 PIV interrogation correlation function as a function of particle image size for (a) large centerline displacements ($\Delta x_m = 15$ pixels) and (b) small displacements ($\Delta x_m = 1$ pixel). (c) PIV displacement estimate scaled with centerline velocity, ($\Delta x_{piv}/\Delta x_m$) as a function of particle image size d_τ and maximum displacement, Δx_m , for uniform tracer particle concentration

The above bias effect due to particle size presents a challenge in terms of experimental design, even before considering random noise correlation and particle migration effects. Ideally, one would like to have a region of the parametric space where even though the bias may exist; it can be minimized, or at least reliably compensated across the full range of particle displacements. At first glance, it would seem that targeting very small particles would be desirable, as this provides a minimal bias error. For example, having a particle image of 2 pixels, with a maximum centerline displacement of 15 pixels would give a bias error of only a few percent. However, in regions of the flow where the average velocity was slower than the expected maximum, the bias error would shift, increasing close to 30% as the displacement dropped to smaller values. For large particle sizes ($d_\tau > 15$ pixels), the errors consistently give a bias of 30%, returning a value close to the gap-averaged value of $2\Delta x_m/3$. While this consistency is an improvement, we note that this requires relatively large particles in comparison to the window size, forcing one to sacrifice precision in the sub-pixel interpolation (which has an optimal near $d_\tau = 2$ pixel (Westerweel 2000 [26]) and increases in proportion to the particle size) or to push the particle concentrations to unreasonably high levels due small interrogation windows (i.e. a 2 pixel particle diameter would require an interrogation window of no greater than 6 pixels in width). It should be noted that the latter could be effectively achieved in steady flows through the use of ensemble correlation.

In addition to the particle-size bias error, measurements resulting from a single interrogation will have random correlation noise due to a small effective image particle density, $N_I F_I F_\Delta$. The effective image density consists of N_I , which is the

particle image density, F_I represents the loss of correlation pairs due to in-plane translation, and F_Δ represents the loss of correlation due to in-plane gradients. The random correlation component is a well-documented and important effect in traditional thin-light sheet PIV, and has led to the standard guideline of maintaining an average of 8 to 10 particle images in an interrogation region to ensure a yield of 95% valid vectors (Kean and Adrian 1992 [27]; Adrian and Westerweel 2010 [11]). The highly non-uniform velocity PDF greatly increases this requirement if one is to ensure that the interrogation peak will repeatedly occur at a known position (either near the maximum displacement or perhaps at a known biased value, as was shown to be the case in figure 2.12). The numerical simulations were used to quantify the likelihood of a valid detection from a single interrogation depending on the effective image density, $N_I F_I F_\Delta$, the results of which are shown for the case of $\Delta x_m = 15$ pixels and $d_t = 4$ pixels in figure 2.13. The most likely peak location for these conditions was 1 pixel less than the peak displacement ($\Delta x_m - 1$) due to the particle size bias effects mentioned above (note that no sub-pixel interpolation was used). Even so, including approximately 100 particles within the interrogation window produced only an 83% probability of making measurement that would provide even a biased estimate. If one were to consider the neighboring displacements of Δx_m and $(\Delta x_m - 2)$ also as a “valid” measurement, this would increase the likelihood to approximately 94% (black curve). This does not give one confidence in making a very reliable measurement under these conditions, as one must sacrifice considerable spatial resolution to attain such a high effective seeding density. These simulations are also optimistic, in that effects of sensor noise and particle non-uniformities are not

accounted for, which would further decrease the probability of a valid measurement. Results for simulation of a uniform displacement for all particles are shown in the figure for comparison.

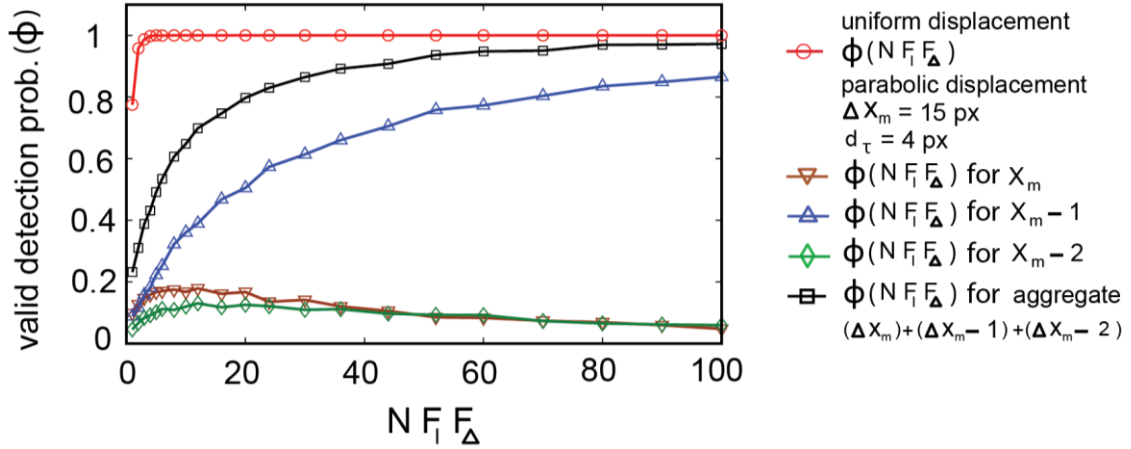


Figure 2.13 Valid detection probability for the displacement correlation peak as a function of the effective number of particle images within an interrogation window ($N F_l F_d$). Note that three expected integer peak locations are tracked near the maximum displacement (no sub-pixel interpolation), and compared to the results of a uniform displacement (shown in red).

2.3.2 Effect of non-uniform tracer concentration

As mention in the introduction, the correlation peak is also influenced by any non-uniform distribution of tracer particles across the gap, which is expected to occur gradually throughout the flow evolution. Indeed, in small depth-of-focus systems, its influence has been used to extract both velocity and concentration profiles (Nguyen et al. 2011). The prior work by Roudet et al. (2011) delineated an expected evolution time required for the particles to migrate to their stable equilibrium positions, $T_m = 2.66\pi z_{eq} \delta^3 / V Re_c a^3$. However, this was shown to be only a rough indication, as the net influence of the particle concentration field on the correlation is the true measure

of how it will influence the PIV interrogation. To observe this effect experimentally and numerically, tests were conducted to interrogate the flow under different development stages, over a range of $10^{-6} < x' < 10^{-1}$ (Note that x' and T_m are related by $t/T_m = 27\delta x'/2 z_{eq}$). Fig 2.14 shows the results of the experiments, alongside results produced from synthetic images of tracer particles migrating according to the theory of Ho and Leal (1974).

Starting from an effectively homogeneous concentration distribution ($x' < 10^{-6}$), a broad correlation function is found with a maximum value corresponding to the centerline velocity across the gap, as discussed in the previous section. The correlation function starts to evolve as particles begin to migrate across the channel, providing a biased sampling of the velocity distribution and distorting the correlation function relative to the uniformly seeded condition. A second peak emerges as the particles rapidly move away from the wall, becoming clearly visible around $x' \sim O[10^{-4}]$, exceeding the peak corresponding to the centerline velocity by $x' > 10^{-3}$. As the particles subsequently migrate from the center plane in later times, the two peaks eventually merge into a single sharp and symmetric peak ($x' \sim 10^{-2}$). This occurs when the majority of the tracers have reached their equilibrium position located close $z_{eq}/\delta = 0.3$. Downstream of this position, the correlation remains unchanged, with a peak value that would predict $U_{piv} = 0.64V_{max}$.

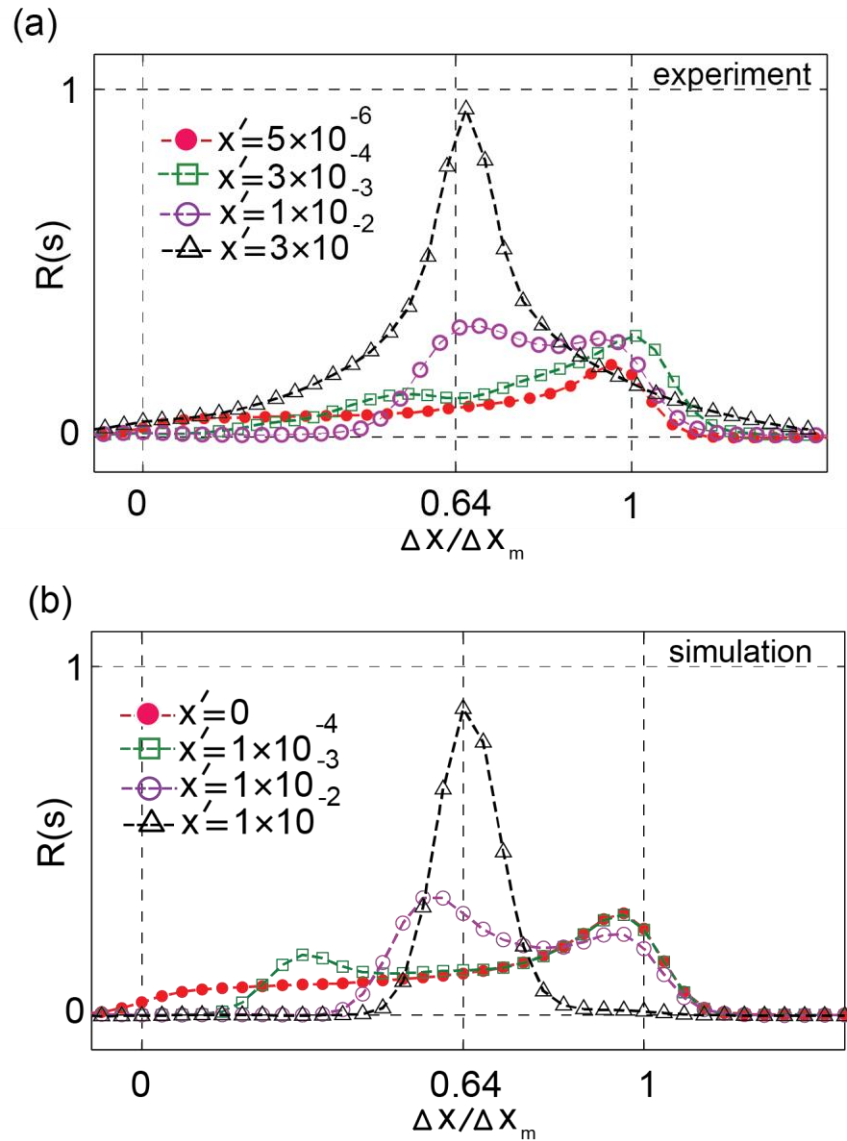


Figure 2.14 normalized averaged correlation functions, depicting their evolution due to combined effects of velocity gradient and particle concentration inhomogeneity, (a) experimental, (b) simulation

Starting from an effectively homogeneous concentration distribution ($x' < 10^{-6}$), a broad correlation function is found with a maximum value corresponding to the centerline velocity across the gap, as discussed in the previous section. The correlation function starts to evolve as particles begin to migrate across the channel,

providing a biased sampling of the velocity distribution and distorting the correlation function relative to the uniformly seeded condition. A second peak emerges as the particles rapidly move away from the wall, becoming clearly visible around $x' \sim O[10^{-4}]$, exceeding the peak corresponding to the centerline velocity by $x' > 10^{-3}$. As the particles subsequently migrate from the center plane in later times, the two peaks eventually merge into a single sharp and symmetric peak ($x' \sim 10^{-2}$). This occurs when the majority of the tracers have reached their equilibrium position located close $z_{eq}/\delta = 0.3$. Downstream of this position, the correlation remains unchanged, with a peak value that would predict $U_{piv} = 0.64V_{max}$.

Although a similar evolution was observed in both the experimental and simulation correlation functions, only approximate matching of x' values was possible, most likely due to a small amount of migration occurring prior to entry into the Hele-Shaw cell. Multiple particle interactions could also have a significant effect, but were neglected in the simulations. The analysis of Ho and Leal (1987) gives the condition that multiple particle effects on particle migration can typically be neglected provided that $\Phi < (a/\delta)^{3/2}$, where Φ is the particle volume fraction. One example of particle-particle interaction effects that can occur for long development lengths and higher particle concentration is illustrated in figure 2.15, where the particles have aligned themselves into ordered chains or clusters of particles in the flow direction, similar to that reported by Matas et al (2004) [28]. In this case, neighboring interaction between clusters of particles in the same plane resulted in the formation of linear streamwise-aligned particle arrays. Matas et al (2004) showed that these clusters occur more frequently with larger Reynolds number, and likely result

from a reversed streamlines created by the disturbance flow due to the leading particle. The rearrangement of the tracer particles did not affect the location of the correlation peak, but broadened the low amplitude tails of the distribution along the streamwise direction due to the non-random anisotropic ordering of the particles (figure 2.15). The chains themselves were found to be unstable and slowly diffuse once the uniform streaming flow was stopped).

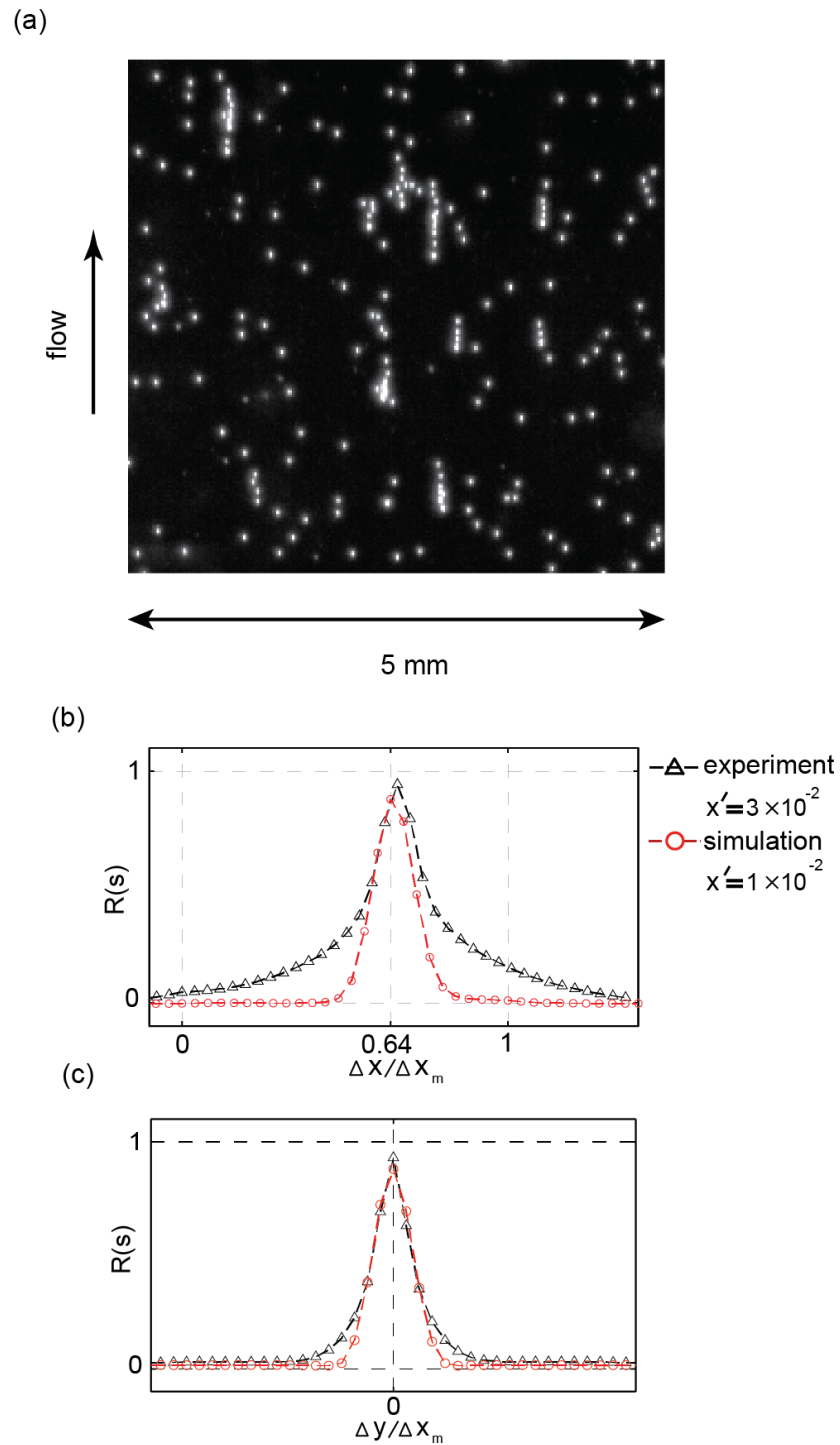


Figure 2.15 (a) streamwise alignment of tracer particles for large x' values. The effect of the directional arrangement of tracer particles on the experimental correlation peak in: (b) stream-wise direction, (c) lateral direction

2.3.3 Interpretation of findings of Roudet et al. (2011)

In the work of Roudet et al. (2011), they showed empirically for their Case II test conditions that a PIV interrogation returned a velocity magnitude equal to the average gap velocity ($U_{piv} = V = 2V_{max}/3$) when the channel Reynolds number is small ($Re_c < 80$). Our findings are not in agreement with this as a universal conclusion, as one would expect based solely on the velocity PDF that the PIV interrogation would return an expected value close to the centerline velocity. The discussion in the previous section would suggest that although migration may not have completed for their flow conditions, perhaps the evolution was sufficient for the secondary correlation peak to surpass the amplitude produced by the centerline flow. The experiments and simulations in the prior section suggest that this should occur for $x' > 10^{-3}$, which would correspond to a flow time $t/T_m > 0.045$ (taking $V = x/t$). This condition was satisfied only for the largest Re_c cases and largest particle sizes used in Roudet et al. experiments, rendering this cause unlikely for the smaller Re_c conditions. This is also in agreement with their suggested speculations.

The question remains, then, as to what caused the unexpected result of $U_{piv} = V$? We contend that this was most likely due to the particle size bias summarized in figure 2.12. For Roudet et al. (2011) PIV measurements, they stated an image size of 3 pixels with an interrogation window of 32 pixels. They also state that the interframe timing was adjusted such that the maximum displacements were between 1/20 and 1/8 of an interrogation cell

($1.6 < \Delta x_m < 4$ pixels, assuming the displacements were those observed from the interrogations, which were shown to be the gap-averaged displacements). Examining figure 12.2, this produces a bias error that is 25 to 33%, giving an expected measurement result of $1.0 < U_{piv}/V < 1.13$, which is quite close to their observed values of ~ 1.05 shown in their figure 6. Thus we would suggest that their observations are actually the result of a particle image size bias effect as explained in section 2.3.1.

2.3.3 Possible Solutions

The presence of multiple and shifting peaks within the expected correlation function due to particle migration makes the probability of choosing a consistent and meaningful displacement for Case II conditions unlikely as a generalized testing point. The exception to this would be for carefully controlled transient conditions where one can ensure that measurements are stopped prior to significant migration, as was the case for the measurements by Roudet et al. (2011). Even so, one would have to restrict the maximum displacement or use quite large particle images relative to the interrogation window size (as noted in section 3.1) to remain in a consistent measurement region due to particle image size effects. Both of these restrictions reduce the effective dynamic range for the measurement, either through the integer displacement or uncertainty in the subpixel estimation (i.e. for the case of Roudet et al. (2011), their peak displacement of 1.5 to 4 pixels with a 0.1 pixel uncertainty in the subpixel interpolation gives an effective dynamic range for a single measurement of 40:1 to 15:1).

This leaves Case I and Case III as more reliable solutions for quantitative measurement. Case I is likely difficult to achieve in many flow conditions, as it only applies to early times when $t < (\delta/2)^2/\nu$ and the parabolic velocity profile is far from being established. This leaves Case III as the most general condition to provide a reliable measurement, as it removes the disadvantages incurred by the wall-normal velocity gradient and having an unknown and changing sampling of the velocity distribution due to particle migration. The challenges with Case III, however, are in how to manipulate the particles into their equilibrium positions prior to making the intended measurements. The simplest case would be to extend the geometry of the thin-gap flow cell to ensure sufficient evolution such that the particles have reached their segregated state, corresponding to $x' \sim O[10^{-2}]$. We have conducted experiments where the Hele-Shaw cell was designed with an extra length section to provide sufficient development length during filling to ensure full segregation, as will be presented in chapter 3. Alternatively, if a longer filling length could not be accommodated, generating an oscillatory flow within the gap could be used to drive the particles toward their equilibrium position by using numerous short strokes in alternating directions; provided the Womersley number was kept small enough to ensure a quasi-steady parabolic profile ($Wo < 1$).

$$Wo = \frac{\delta}{2} \sqrt{\frac{2\pi f}{\nu}} \quad 2.21$$

Where δ is the gap thickness, f is the strokes frequency in cycles and ν is the kinematic viscosity of the fluid.

Finally, work of Mielnik et al. (2006) [29] could also be adapted for this purpose, who introduced selective seeding of thin particle “sheets” into their channel

by manipulating the flow through a series of T-junction inflow channels, confining the particle laden flow to a specific cross-gap location. While this has the added complication of a complex inflow supply manifold, it has the advantage of being able to seed a particle sheet to almost any cross-stream location, obviating the need for a significant development region. All of these solutions would allow for use of what is known about standard thin-sheet PIV measurement, and hence take advantage of the demonstrably improved accuracy and resolution that is possible under uniform displacement conditions. However, since these measurements rely on the fluid flow profile and particle position across the gap to be known *a priori*, they become insufficient in cases of more complicated micro-fluidic devices with 3-dimensional flow fields. In these cases, performing a large field of view measurement becomes impossible unless local fluid flow and tracer particle concentration distribution across the gap are available. On the other hand, there are a variety of techniques such as confocal scanning microscopy or astigmatism that are capable of measuring a 3-dimensional velocity field over much smaller regions (Cierpka et al. 2011) [30].

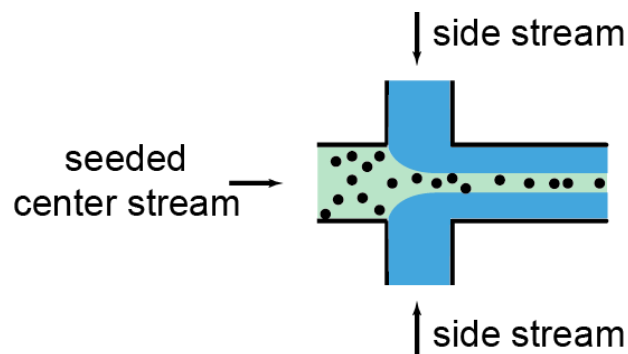


Figure 2.16 principle of hydrodynamic focusing

Chapter 3: Rayleigh-Bénard convection in a Hele-Shaw cell,

PIV demonstration

3.1 Problem Statement and experimental setup

This section presents a sample measurement utilizing Case III conditions that were generated through the manipulation of the filling conditions to ensure particle migration to their equilibrium position prior to measurement. The flow of interest is the onset of solutal driven Rayleigh-Bénard convection in a Hele-Shaw cell, which is used as an analog for similar behavior in porous media in the context of carbon dioxide sequestration in saline aquifers. The initial conditions for the experiment consist of two stably stratified stationary fluids of different density, which exhibit the property that the resulting mixture has a greater density than either two of the original fluids. As the two fluids undergo diffusive mixing at the interface, a thin layer develops that is gravitationally unstable, resulting in the onset of convective plumes and an increase in the bulk mixing of the two layers (figure 3.1).

The experimental setup consists of the Hele shaw cell similar to the previous setup with the same gap thickness ($\delta=127\ \mu\text{m}$). The U-shaped shim was replaced with a closed rectangular shim. A disadvantage of a pump is the pulse, which disturbs the filling process. In this phase of the project, the syringe pump was also replaced with pressure cups to fill the cell smoothly and provide a sharp, steady interface during filling procedure. Both tanks were fed with the same compressor, but the pressure at each tank could be slightly adjusted using separate pressure regulators for each tank.

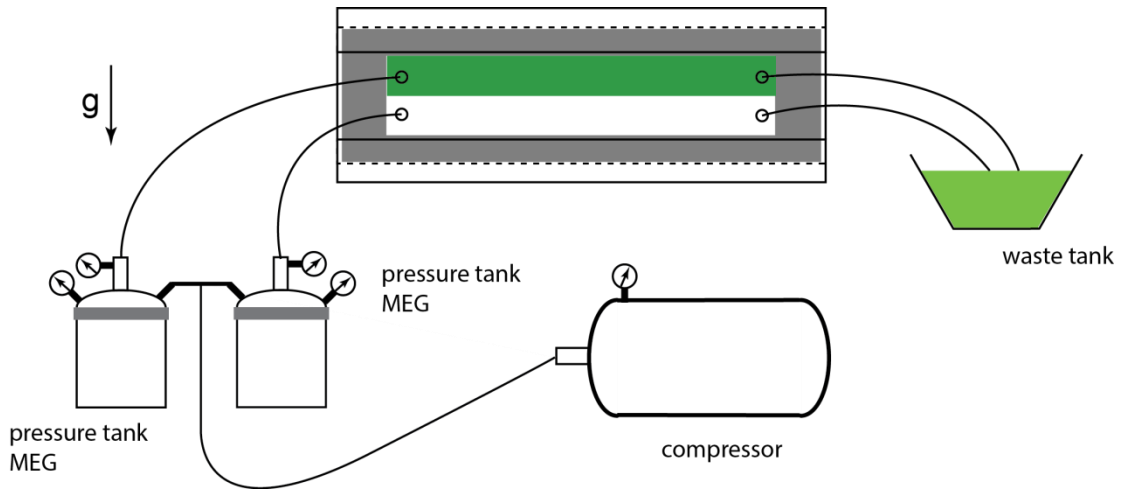


Figure 3.1 a schematic of the experimental setup for velocity measurements in Hele shaw cell. The pressure tanks were designed to hold a deformable cup inside them to hold the seeded fluids. Details of the setup can be found in appendix A.

The initial conditions for the experiment consist of two stably stratified stationary fluids of different density, which exhibit the property that the resulting mixture has a greater density than either two of the original fluids. As the two fluids undergo diffusive mixing at the interface, a thin layer develops that is gravitationally unstable, resulting in the onset of convective plumes and an increase in the bulk mixing of the two layers. It should be noted that for the analog between the Hele-Shaw cell and porous media to be valid, the density driven currents must maintain a parabolic velocity profile across the gap. Fernandez et al. (2002) [31] reported that this condition will be met if the Rayleigh number based on the gap thickness is restricted to values $Ra_\delta < O[100]$, where $\Delta\rho$ is the driving density difference, g is the acceleration due to gravity, D is the effective binary diffusivity of the two fluids, and ν is the effective dynamic viscosity of the mixture.

$$Ra_{\delta} = \frac{\Delta\rho g \delta^3}{12D\mu} \quad 3.1$$

The working fluids are methanol/ethylene-glycol (MEG) and water, which has been used in similar studies in porous media (Neufeld et al. 2010 [5]). The example shown in figure 3.2 used a MEG solution that was 61% Methanol by weight ($\rho_{MEG} = 972.5 \text{ kg/m}^3$, $\mu_{MEG} = 0.003 \text{ kg/m.s}$) mixing with water ($\rho_{H2O} = 997.0 \text{ kg/m}^3$, $\mu_{H2O} = 0.001 \text{ kg/m.s}$), producing a maximum specific gravity of approximately 1.01. The cell was designed with an extended streamwise development length ($L = 300 \text{ mm}$) to ensure that the tracer particles present within the mixtures have migrated into their known stable position before reaching to the measurement window. The difference in viscosity between the two streams necessitated different flow rates to produce a similar pressure drop in each liquid layer, which was required to maintain a straight interface between the two fluids. The filling process and measurement location were such that the particles migrated to their equilibrium wall-normal position, which was checked by sampling the correlation function of a PIV interrogation during the filling process and confirming that a single symmetric correlation function was obtained (see figure 2.14). Although particle streaks formed in the more fully evolved water layer, these quickly dissipated into a random field as the particles gradually settled during onset of convection and during the cross-stream motion of the convective fingers.

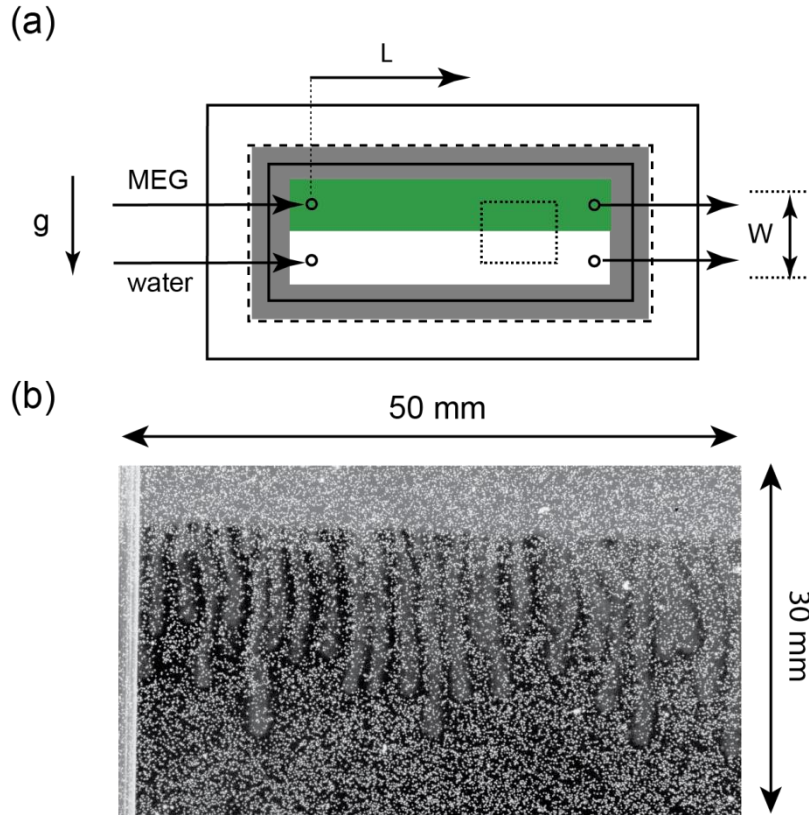


Figure 3.2 schematic of the test setup for diffusive Rayleigh-Bénard convection (a) (MEG 61 wt% is shown in green and water in the bottom layer is transparent), (b) Image of convective fingering instability, 1000 seconds after isolation

Measurements were then performed after stopping the flow and isolating the cell from surroundings by a combination of toggle/check valves. Images were acquired with the same camera and light system used in the earlier experiments. The magnification was set $M_0=0.35$ (38 pixel/mm), with an effective particle image size measured to be approximately 5 pixels. A decreasing size_multipass interrogation was applied, used in conjunction with adaptive correlation windowing (Wieneke and Pfeiffer, 2010 [32]), starting from 48x48 and reducing to 24x24, with a 75% overlap (Note that the adaptive masking gives a minimum interrogation width of effectively

12 pixels in high shear regions). No ensemble averaging was used, since this flow is inherently unsteady and spatially non-uniform. A sample measurement of the convection under these conditions is illustrated in figure 3.3. From this figure, it can be seen that the convective plumes are approximately 2 mm in width, setting a desired spatial resolution of approximately 0.25 mm, with peak velocities on the order of 60 $\mu\text{m/s}$ in the measurement plane.

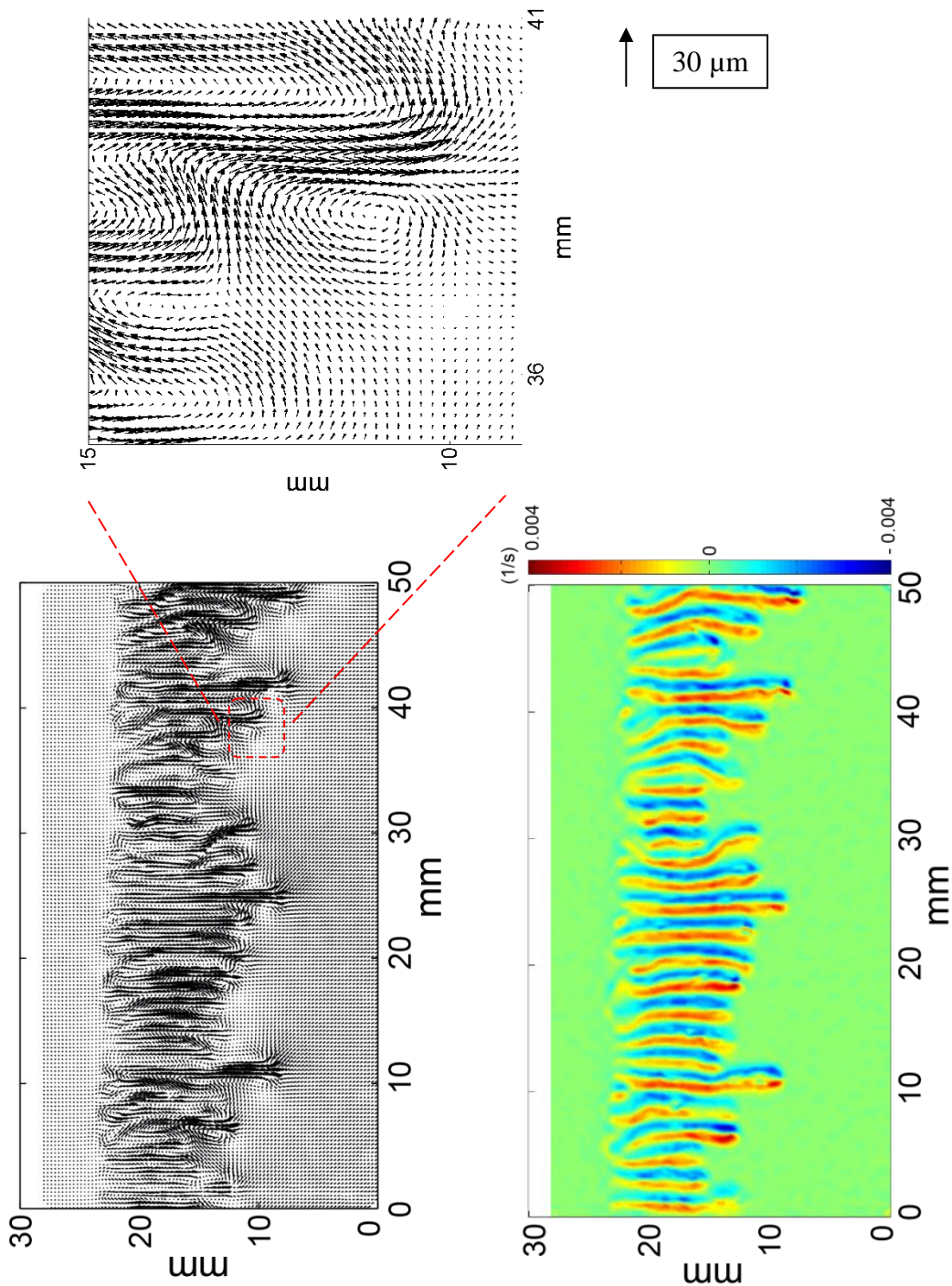


Figure 3.3 (a) instantaneous velocity field, (b) a more focused view of velocity field and (c) vorticity field for the diffusive Rayleigh-Bénard convection with large depth of field PIV ($Ra_\delta \approx 3$, $\delta = 0.127 \text{ mm}$)

3.2 Design parameters

The execution of such an experiment requires a careful tradeoff in the test cell design and particle selection in order that Case III conditions can be attained. First and foremost is determination of a suitable gap thickness, as once the working fluids have been selected, this sets the gap Rayleigh number (Ra_δ) and the length scales of the convective plumes. These considerations are summarized in figure 3.4, which bounds the limits on the desired interrogation window size, D_I , as a function of the gap length, δ . The first constraint is the assumption of $Ra_\delta < 100$, which ensures that one is well within the recommended region for Poiseuille flow to be maintained within the unstably stratified gap (Fenandez et al., 2002 [33]). (Here we have taken mixture values for the properties of $\mu=0.002$ kg/m.s, $\Delta\rho= 10$ kg/m³, and $D=1.2\times 10^{-9}$ m²/s). A second constraint is provided by requiring D_I to be smaller than the relevant length scale of the flow, which we specifically take to be

$$D_I < \frac{M_0 \lambda}{4} \quad 3.2$$

In the current problem, the initial wavelength is well predicted by linear stability theory to be (Riaz, et al., 2006 [8]):

$$\lambda = \frac{24\pi}{0.07} \frac{\mu D}{\Delta\rho g \delta^2} \quad 3.3$$

Giving:

$$\frac{D_I}{d_r} < \frac{6\pi}{0.07} \frac{\mu D M_0}{\Delta\rho g d_r} \quad 3.4$$

when accounting for the image magnification and expressing it in terms of image pixels. A third constraint is given by the minimum particle image density needed to have a high probability of a successful interrogation, typically assumed to be $N_I > 10$. For the Case III conditions, an upper bound on the concentration that can be used

exists due to the fact that all of the particles must be eventually packed into two parallel planes of the channel. Assuming the particles should remain separated by at least 5 diameters ($s = 5d$) to prevent significant hydrodynamic interactions gives the constraint:

$$\frac{D_I}{d_r} > \sqrt{10} M_0 \frac{s}{d_r} \quad 3.5$$

The current experimental conditions are indicated by the symbol (red star) in figure 3.4, indicating that not much margin remains for improvement of the measurement conditions when using the current working fluids.

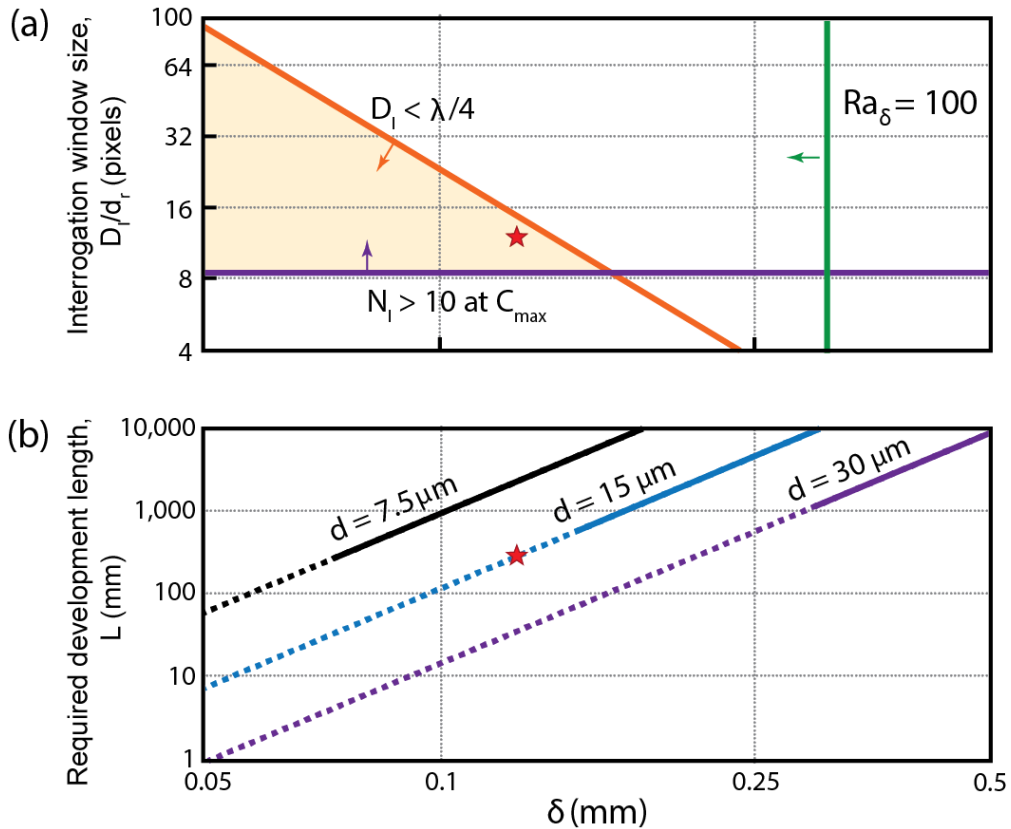


Figure 3.4 (a) interrogation window size as a function of Hele-Shaw gap thickness (b) required development length needed during filling to ensure Case III conditions as a function of Hele-Shaw gap thickness and particle size ($Re_c = 2.3$). Current operating conditions are noted by the red star. Dashed line indicates $d > 0.1\delta$

The particles then need to be selected such that they reach their terminal migration position within a reasonable length, which is controlled by the Reynolds during filling and $(a/\delta)^3$. Using the condition that $L/X > 0.01$ from figure 2.14 for complete migration, the required flow development lengths are given in Fig 10b. This gives a required length of:

$$L = 0.36\pi \left(\frac{\delta}{a}\right)^3 \frac{\delta}{Re_c} \quad 3.6$$

For the more conservative conditions of the flow in the MEG layer, the current conditions ($d = 2a = 15 \mu\text{m}$, $\delta = 127 \mu\text{m}$, $Re_c = 2.3$) give a required development length of $L = 303 \text{ mm}$. The lower viscosity of the water layer requires a higher Reynolds number to produce the same pressure drop, leading to a development length of 46 mm. Going to a smaller particle size would lead to a much larger development length (e.g. using half the diameter would require a channel length of 2.4 m), while going larger would require particles that are rapidly becoming a significant fraction of the gap width.

Chapter 4: Quantitative concentration measurement in narrow channels

4.1 Experimental Setup

The motivation for this part of the project is to quantify the temporal concentration field of Rayleigh-Bénard convection in a Hele-Shaw cell and eventually couple it with velocity measurement to estimate the total flux density of MEG in water. Backhaus et al. (2011) [6] developed an experimental model with a different fluid system and performed optical shadowgraph to determine the wave number selection, the time scale, the finger width, and the mass transport rate. Hartline et al (1970) [33] applied pH-indicator method to visualize the convection pattern of thermal convection in a Hele-Shaw cell and confirmed the critical Rayleigh number for the onset of convection to be $4\pi^2$.

There are various other measurement techniques that have been used previously to quantify the scalar transport within multi-component fluidic systems (See Walker et al. 1987 [34]). Measurement of concentration based on induced fluorescence is a common technique that was also used in this study to quantify the concentration profile within the system. For instance, Koochesfahani et al (1986) [35] used LIF to investigate the entrainment and mixing in reacting and nonreacting turbulent mixing layers or the work Ferrier et al (1993) [36] that discusses the use of the measurement technique and methods of corrections to study plumes in stratified fluids in details.

In a general LIF experiment (Laser/LED induced Fluorescence), the dye is excited by an illumination light source whose wavelength closely matches the excitation frequency of the dye. The intensity of light emitted from a dyed region of flow is proportional to the intensity of excitation energy and to the concentration of dye. If the excitation energy is locally uniform, then the emitted light intensity will be linearly related to the dye concentration. By performing a calibration procedure as will be discussed in the following section, the emitted light intensity can be directly converted to dye concentration.

To perform a reliable concentration measurement by means of LIF, multiple steps need to be taken to overcome the challenges inherent to fluorescence. These practical steps are the subject of this chapter. The challenges include:

- Maintaining linear relationship between intensity of emitted light and concentration
- Perform correction methods due to non-uniformity of illumination across the field of view and background intensity variations
- Sensitivity to environment effects (solvent effect)
- Photobleaching due to exposure to light

The fluorescence process consists of three stages: First, a photon is absorbed by the fluorophore, increasing its energy to an excited state. Second, the fluorophore remains in this excited state for a finite period, called the fluorescent lifetime, which lasts typically 1–10 ns (very small relative to the flow time scales $O(10 \text{ seconds})$). Third, the fluorophore releases a photon of energy, and returns to its ground state (figure 4.1). The released photon is then detected by a sensor, a CCD camera detector in this case. Due to energy dissipation during the excited state lifetime (non-radiative

relaxation), the energy of this photon is lower, and therefore of longer wavelength, than the excitation photon (for detail discussions on fluorescence, refer to Principles of fluorescence spectroscopy by J. Lakowicz [37] or Practical fluorescence by G. Guilbault [38]). The energy difference is related to the Stokes shift, which is the wavelength difference between the absorption and emission maximum:

$$\Delta\lambda_{\text{stokes}} = \lambda_{\text{emission}} - \lambda_{\text{absorption}} \quad 4.1$$

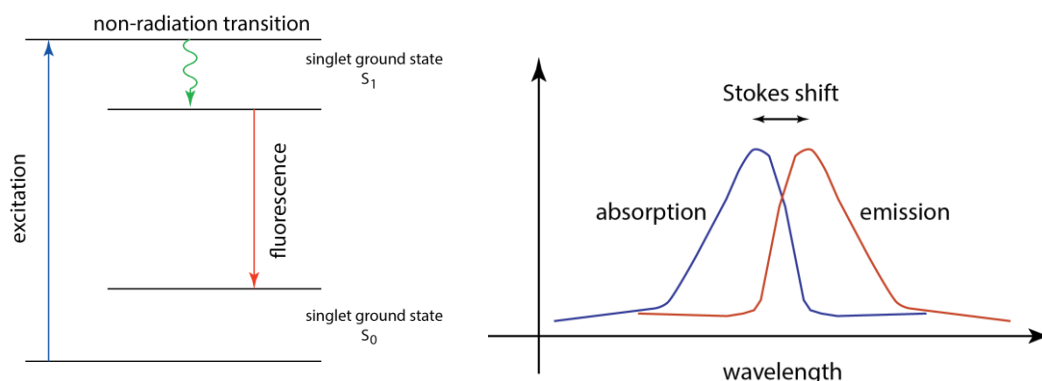


Figure 4.1 a Jablonski diagram and corresponding spectra, demonstrating the fluorescence process: initial creation of an excited state by absorption and subsequent emission of fluorescence at a higher wavelength

Although LIF has been widely used for determining the scalar transport and mixing of multicomponent fluid systems, there are also drawbacks to this technique that necessitates a well calibrated measurement setup. Relevant to this work is photobleaching of fluorescent molecules that is a process by which exposure to excitation light chemically alters a fluorophore rendering it non-fluorescent. The rate of photobleaching of a fluorescent dye depends on the photon flux, and may be caused by large excitation light intensities over short periods or lower intensities over

long periods. Photobleaching is a common problem in fluorescence-based experiments like this study where the fluorophore remains excited for long durations.

The experimental test setup was modified to be able to extract temporal velocity as well as concentration fields simultaneously. However, this chapter focuses on calibration procedure for concentration measurement while the coupling of the concentration and velocity measurements will be the subject of the next chapter. In addition to polystyrene microspheres that were used as tracer particles for velocity measurement in both of the fluids, a known amount of Fluorescein sodium salt ($C_{20}H_{10}Na_2O_5$ Sigma-Aldrich F6377) was added to the fluid reservoir containing the mixture of Ethylene glycol and Methanol (MEG), to be used as tracers for concentration measurements. The diffusivity of the dye into water is close to the diffusivity of Ethylene glycol in water, while the diffusivity of Methanol in water is 4 times larger. Molecular diffusivity (\mathcal{D}) of the different species and the dye in water is listed in table 4.1.

Diffusion Coefficient for the Different Species	
Ethylene glycol [39]	$0.37 \times 10^{-9} \text{ (m}^2/\text{s)}$
Methanol [40]	$2 \times 10^{-9} \text{ (m}^2/\text{s)}$
Fluorescein [41]	$0.52 \times 10^{-9} \text{ (m}^2/\text{s)}$

Table 4.1 diffusion coefficient for different species present in the fluid mixture in water

To excite the fluorescence tracers, the halogen light was replaced by a high-power LED illuminator (IL-106X-Blue, HARDsoft) in continuous mode. Spectral

characteristics of the light source and the dye are presented in figure 4.2. A second camera was also added to the system to record the magnitude of fluorescence from a similar field-of-view as of camera 1 (figure 4.3). The cameras and the lenses used in the setup were identical (Imager pro X 4M, sensor size = 2048 x 2048 pixels, $d_r = 7.4$ μm pixel size) and recorded images of about 75 x 75 mm region ($M_0 \sim 0.2$), using 105 mm lenses ($f_1\# = 8$ and $f_2\# = 2.6$; *Exposure time*₁ = 0.05s and *Exposure time*₂ = 0.1s). The depth of field of the system, δz was set larger than the channel gap spacing as before so that the tracer particles across the entire gap were mapped identically in the image plane ($\delta z_1 = 4$ mm, $\delta z_2 = 0.5$ mm). An optical long-pass filter with a transition wavelength of 515 nm was inserted close to camera 2 in its optical axis to separate the fluorescence emission photons that form the final image on detector 2 from the excitation light and scattering particles (MELLES GRIOT 03FCG083-rectangular 50.8x50.8 mm²) (figure 4.3). As explained in previous chapters, polystyrene particles are manipulated into the equilibrium position before they reach to the desired field of view.

The experiments were conducted using a vertically oriented Hele-Shaw cell similar to previous setup but the all-round supporting frame that was found vulnerable to buckling was replaced by two edge-to-edge supporting clamps, holding the fixture on the top and bottom (figure 4.5). The two rectangular tempered glass plates were also replaced by longer pieces (12.7 x 610 x 127 mm³) to ensure full segregation of tracer particles in the field of view (L=330 mm) and also to avoid regions of any possible non uniform behavior at the outlets (refer to appendix A). The spacer shim was pressed between the plates by the designed aluminum clamps, with a bolt spacing

of 8 cm along the top and bottom edges to ensure a uniform compression and a constant gap thickness ($\delta=0.127$ m; the bolts were fastened by a torque wrench by a value of 1700 N-mm). Sample images recorded simultaneously by the two cameras, are presented in figure 4.6.

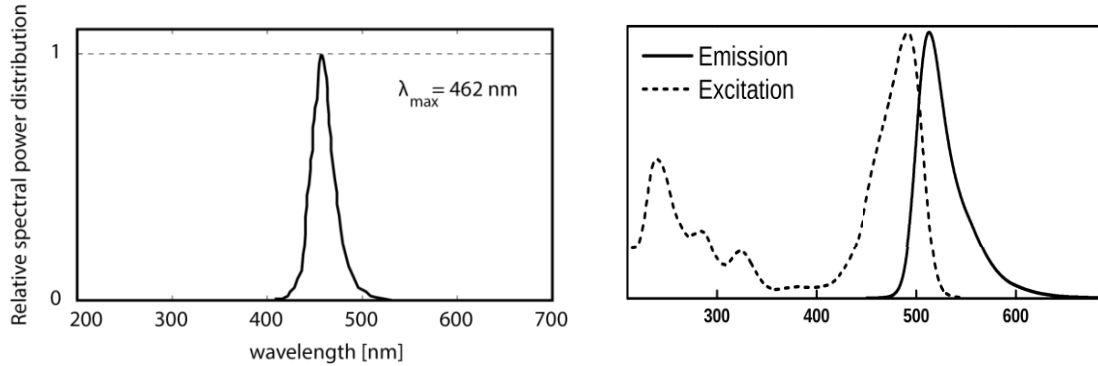


Figure 4.2 a) Spectral characteristic of the LED (blue light; $\lambda_{max}=462$ nm), b) Fluorescence properties of the dye ($\lambda_{max-excitation}=490$ nm)

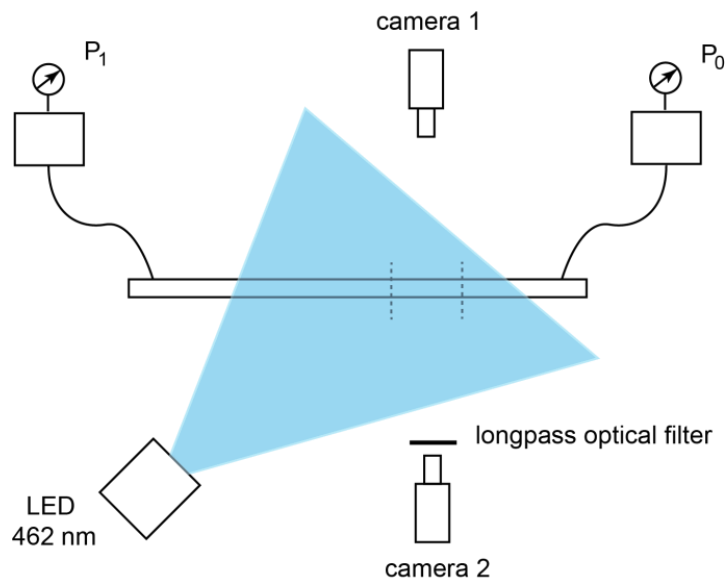


Figure 4.3 Schematic of the experimental setup from above. Camera 1 is used for PIV measurements, and camera 2 records the fluorescence while the optical filter extracts the pumping light

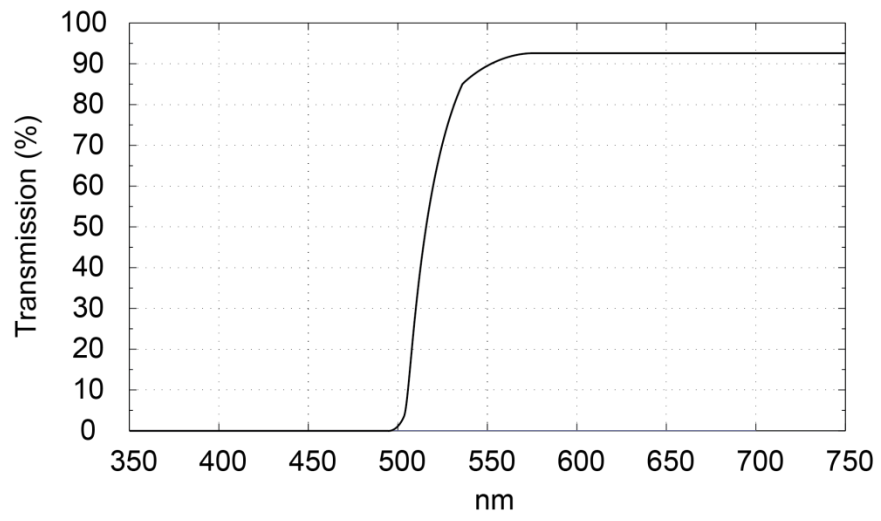


Figure 4.4 the long-pass optical filter performance, cut-on of 515 nm

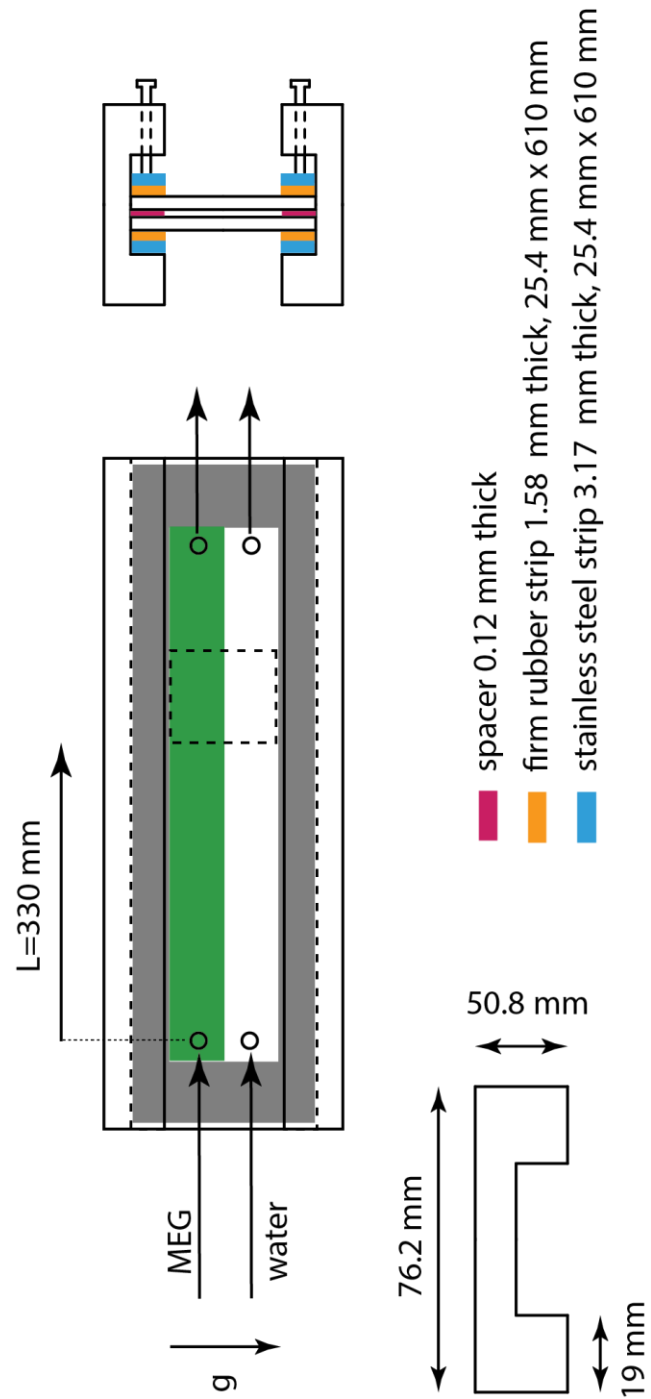


Figure 4.5 a schematic of the experimental setup

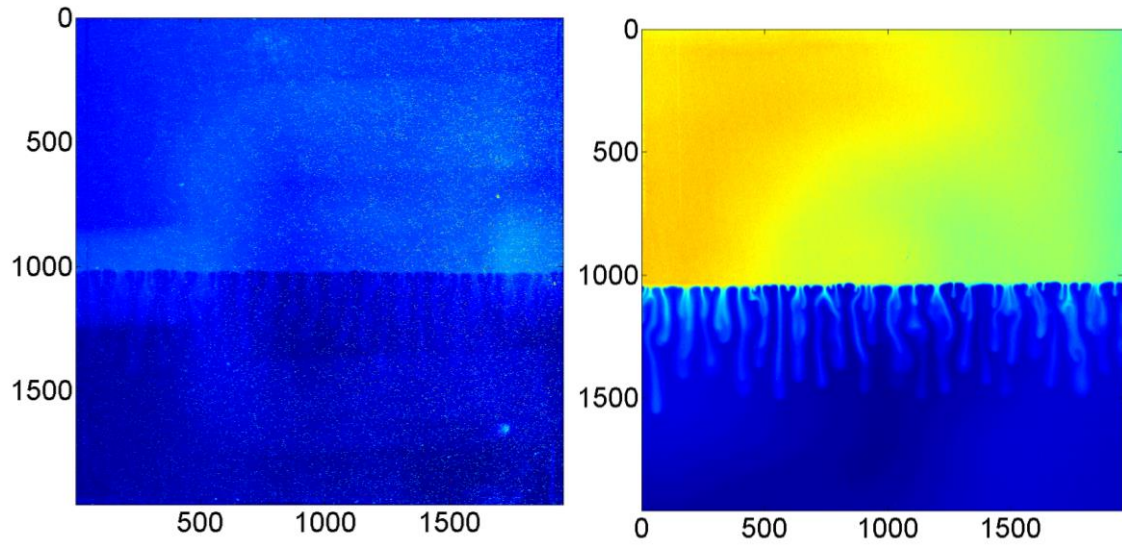


Figure 4.6 Snapshot images of the field of view at $t=1000$ s. Image a from camera 1 is used for velocity measurements while the second image is used for fluorescence

4.2 Calibration procedure

Details of the execution of a reliable velocity measurement is covered in the previous chapters, however extraction of temporal concentration field from raw images recorded from the second camera requires a calibration procedure to quantitatively relate the intensity and absolute concentration field. If attenuation of the illumination light within the cell is negligible and the concentration of the dye is low enough that there is no saturation (both fluorescence and detector), then the detected fluorescence would be proportional to intensity of the excitation illumination and local concentration of the fluorophore (Walker et al 1987 [34]).

$$I_f^n(\vec{x}, t) = \alpha I_i^n(\vec{x}) c(\vec{x}, t) \quad 4.2$$

In this equation, $x (x_1, x_2)$ represents both the position in the object plane and image plane (since a mapping presumably exists between object and image plane). The excitation power distribution field generated by the LED is shown as $I_i(\vec{x}, t)$. The detected fluorescence $I_f(\vec{x}, t)$ is related to I_i and the average dye concentration distributed across the gap of the cell by the proportionality factor α .

$$c = \frac{1}{\delta} \int_0^\delta c(x_1, x_2, z, t) dz \quad 4.3$$

Initially, a series of calibration experiments were performed to determine the range of linear response of fluorescence intensity to its concentration variations. A known concentration of the dye was added to 200 ml of deionized water and the well stirred mixture was then pumped through the cell. The recorded images from camera 2 were averaged over the entire field-of-view after background subtraction and then were temporally averaged over 1000 images recorded at 1Hz. For all the tests the cell

and LED were kept fixed to the optic table carrying the experimental setup and the LED power was also kept constant. It can be observed from figure 4.7 that the relationship between the effective fluorescence and the fluorophore concentration under conditions described above becomes nonlinear at around 0.5 (mg/ml). In order to be able to use equation 1, the concentration of the dye needs to be smaller than this critical value. It should be noted that a larger $f\#$ and smaller exposure time was used in the calibration test to avoid any possible camera saturation ($f\#4$ and $Exposure\ time_2=0.03\ s$). However a smaller $f\#$ and a larger exposure time were used to obtain a greater dynamic range with a conservative concentration value of 0.05 (mg/ml) for the rest of the experiments ($f\#2.6$ and $Exposure\ time_2=0.1\ ms$).

As explained in previous chapters, the initial condition for the experiment consists of stably stratified stationary fluid columns of MEG at the top and water at the bottom. Both of the fluids are seeded with microspheres for velocity measurements, and additionally MEG is also seeded with dye tracers with a concentration of 0.05 (mg/ml) for which the fluorescence shows a linear behavior in its vicinity (figures 4.7 and 4.8). As the dye tracers diffuse into water from the MEG column, the fluorescence is expected to deviate due to the change in solvent. A series of dilution tests were performed by providing different aqueous MEG mixtures, pumping them into the cell and recording the fluorescence as described in previous calibration tests (figure 4.9). For instance, the data point describing 0.2 aqueous MEG mixture is the result of mixing 40 g MEG from the original batch of MEG with a dye concentration of 0.05 (mg/ml) and 160 gr deionized water; the resultant mixture then contains a dye concentration of 0.01 (mg/ml). Due to dependency of fluorescence to

environmental factors such as viscosity, a linear function was found to be a poor estimate of the fluorescence behavior in the aqueous MEG mixture ($\mu_{MEG} = 0.003$ kg/m.s and $\mu_{water} = 0.001$ kg/m.s; effective fluorescence in water is 0.95 of fluorescence in MEG; black square symbol). It should be noted that temperature fluctuation was less than 1°C during the entire measurement period.

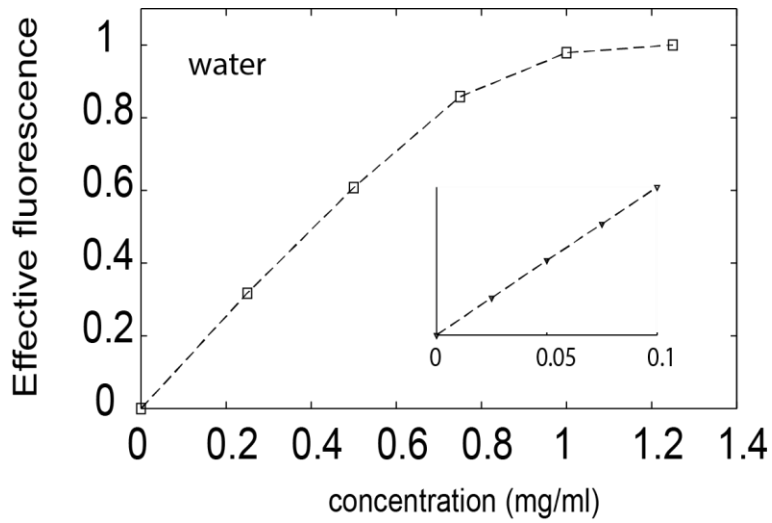


Figure 4.7 effective fluorescence for Fluorescein in water

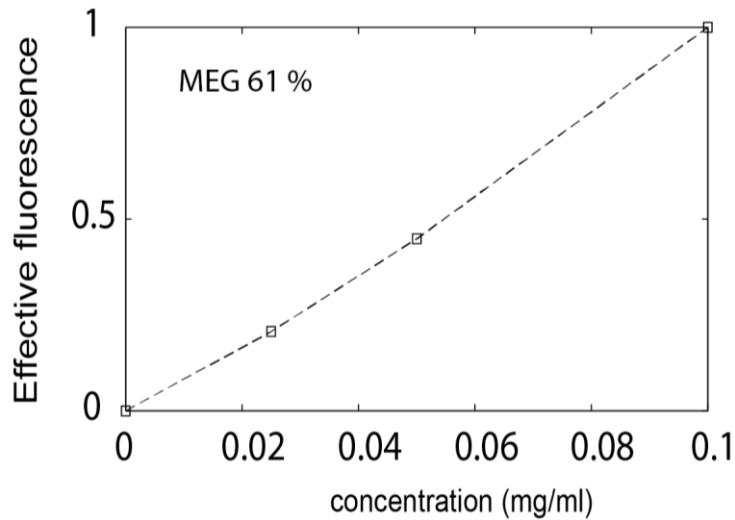


Figure 4.8 effective fluorescence for Fluorescein in MEG 61%

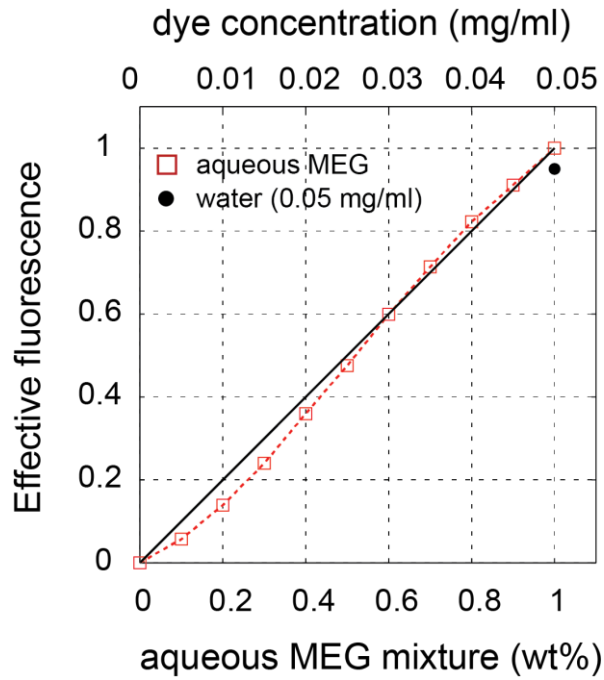


Figure 4.9 different fluorescence behavior of the dye in different solvents

4.3 Data Reduction

Following the data acquisition, the images need to be processed to obtain concentration information based on the detected intensity field from camera 2. The experimental procedure starts with performing the instability test with the appropriate design conditions as was explained in previous chapters and recording the intensity field; $I_{raw}(\vec{x}, t)$. To take into account for the image background intensity, a series of images were then recorded from the same field of view and similar conditions to the initial test after flushing the cell with deionized water multiple times; $I_{offset}(\vec{x}, t)$. In the final step, the distribution of light intensity across the field of view was quantified by obtaining 1000 consecutive images when the cell was filled with only MEG and uniform dye concentration of 0.05 (mg/ml); $I_{max}(\vec{x}, t)$. Several sub-regions were

defined and used for normalization purposes (as shown in figures 4.10-4.13) to make the concentration measurements quantitative. The calculation procedure is as follows:

$$\bar{I}_{offset}(\vec{x}) = \frac{1}{N} \sum I_{offset}(\vec{x}, t), N = 1000, \bar{I}_{max}(\vec{x}) = \frac{1}{N} \sum I_{max}(\vec{x}, t), N = 1000 \quad 4.4$$

$$I_i(\vec{x}) = \bar{I}_{max}(\vec{x}) - \bar{I}_{offset}(\vec{x}) \quad 4.5$$

$$\langle I_{i-R1} \rangle = \frac{1}{N_1} \sum_{region1} I_i(\vec{x}), N_1 = 50 \times 50 \quad 4.6$$

$$I_i^n(\vec{x}) = \frac{I_i(\vec{x})}{\langle I_{i-R1} \rangle} \quad 4.7$$

$$I_f(\vec{x}, t) = I_{raw}(\vec{x}, t) - \bar{I}_{offset}(\vec{x}) \quad 4.8$$

$$\langle I_{f-R1}(t) \rangle = \frac{1}{N_1} \sum_{region1} I_f(\vec{x}, t), N_1 = 50 \times 50 \quad 4.9$$

$$I_f^n(\vec{x}, t) = \frac{I_f(\vec{x}, t)}{\langle I_{f-R1}(t = 0) \rangle} \quad 4.10$$

$$I(\vec{x}, t) = \frac{I_f^n(\vec{x}, t)}{I_i^n(\vec{x})} \quad 4.11$$

$$c(\vec{x}, t) = \frac{I(\vec{x}, t)}{\alpha} \quad 4.12$$

$$I_i(\vec{x}) = \bar{I}_{max}(\vec{x}) - \bar{I}_{offset}(\vec{x}) \quad 4.13$$

$$\langle c_2(t) \rangle = \frac{1}{N_2} \sum_{region2} c(\vec{x}, t), N_2 = 50 \times 500, \langle c_3(t) \rangle = \frac{1}{N_3} \sum_{region3} c(\vec{x}, t), N_3 = 50 \times 500 \quad 4.14$$

$$c'(\vec{x}, t) = c(\vec{x}, t) - \langle c_3 \rangle_{\text{constant}} \quad 4.15$$

$$c_f(\vec{x}, t) = \frac{c'(\vec{x}, t)}{[\langle c_2(t) \rangle - \langle c_3 \rangle_{\text{constant}}]} \quad 4.16$$

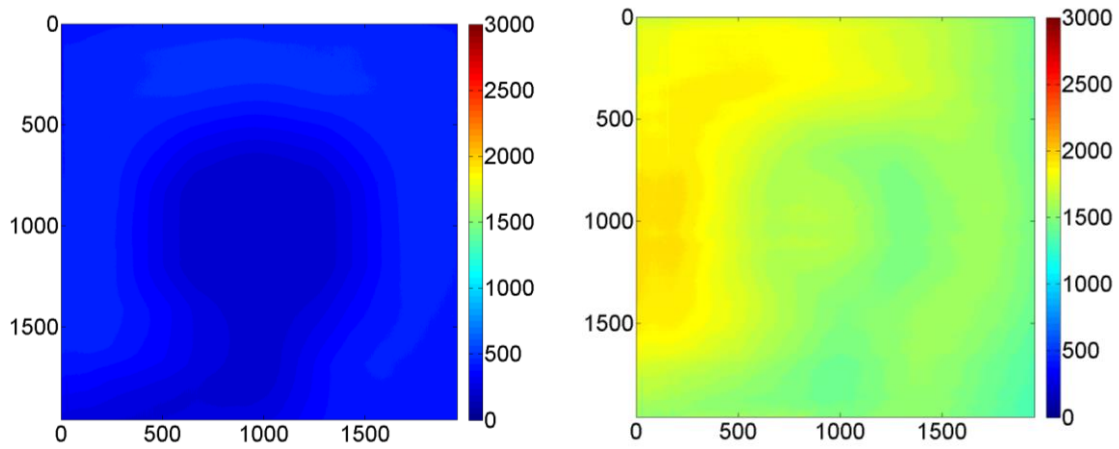


Figure 4.10 $\bar{I}_{offset}(\vec{x})$ on the left and $\bar{I}_{max}(\vec{x})$ on the right

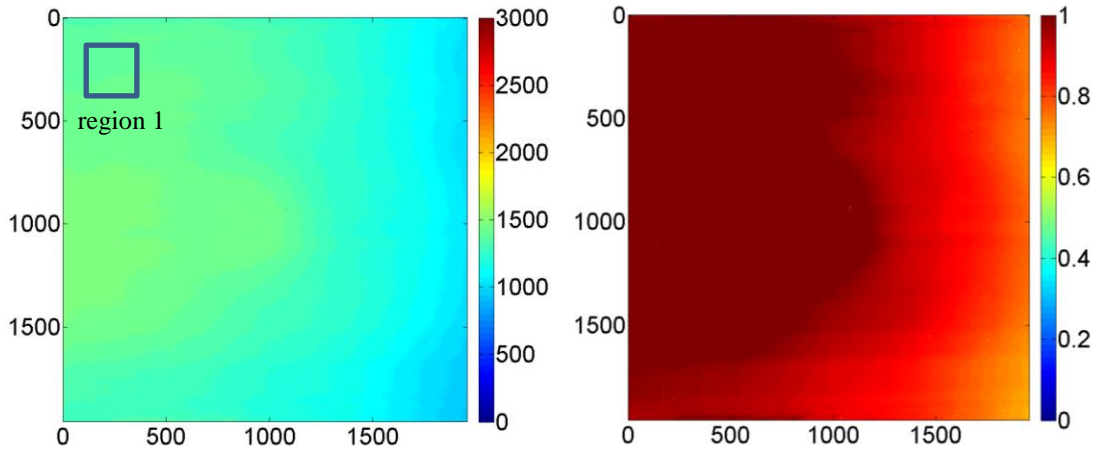


Figure 4.11 $I_i(\vec{x})$ on the left and $I_i^n(\vec{x})$ on the right

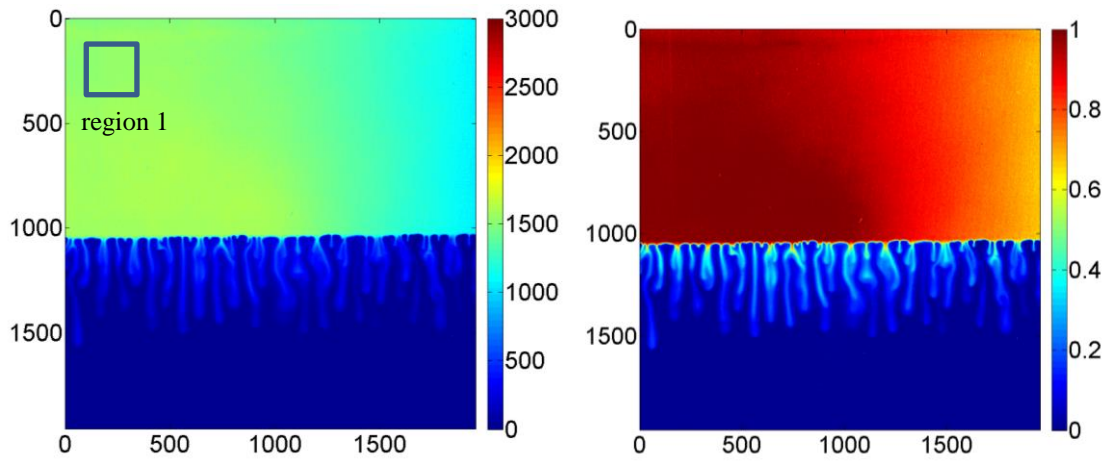


Figure 4.12 $I_f(\vec{x}, t = 1000 \text{ s})$ on the left and $I_f^n(\vec{x}, t = 1000 \text{ s})$ on the right

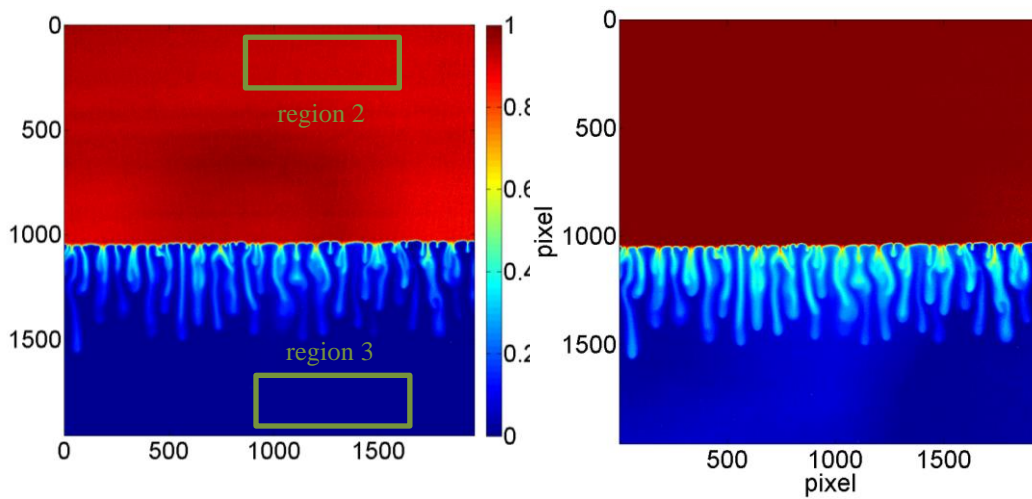


Figure 4.13 $c(\vec{x}, t = 1000 \text{ s})$ on the left and $c_f(\vec{x}, t = 1000 \text{ s})$ on the right

Equation 4.7 represents the normalized field for the illumination power, while equation 4.10 corresponds to the normalized detected fluorescence. In the final step, the intensity value c can be related to the concentration of the dye by data points collected previously to quantify the dye fluorescent behavior in different fluid components (figure 4.9). Presuming that the dye, methanol and ethylene glycol all stay in nearly the same proportions as they diffuse in water, the detected fluorescence represents the propagation of MEG in water. In theory, $c(\vec{x}, t)$ should change from 0 corresponding to zero concentration of the dye and 1, representing the initial concentration of the dye (0.05 (mg/ml)). However, in practice, there is a continual decrease of fluorescence intensity of the dye due to the exposure to light, i.e. photobleaching that negatively affects the measurements. The mean concentration calculated from equation 4.14 over region 2 is presented in figure 4.14. Since there is pure MEG in this region during the entire experiment, the estimated concentration mean is expected to remain constant, provided that the temporal variations of illumination power remains constant.

This decrease in fluorescence intensity due to photo-bleaching can be significant (5% in the time scale of the tests) and is undesirable as it could be incorrectly interpreted as a reduction in concentration. A simple method to avoid photo-bleaching is to pulse the LED rather than a continuous illumination to decrease the effective period of time fluorophore particles are exposed to the light. However in the pulse mode due to the device limitations, the required light pulse width could not be achieved with an appropriate power levels to excite the dye particles. The second option was to correct the images by first choosing an arbitrary region in the upper

layer where there always exists pure MEG (region 2) and calculating the mean concentration value in this area $\langle c_2(t) \rangle$. Then choosing an arbitrary region in the bottom layer and calculating the mean concentration value in this area $\langle c_3(t) \rangle$ (region 3). And finally, normalizing the concentration field by $c_2(t)$ after subtracting the offset value $c_3(t)$. A snapshot of the calculated concentration field is shown in figure 4.13 (on the left) by correcting the images. The offset value $c_3(t)$ doesn't remain constant during the entire experiment as fingers containing the dye particles reach to the bottom of the cell but during the initial phase where there is pure water, light intensity remains constant and this value was used as the offset value for the entire set $\langle c_3 \rangle_{constant}$ (figure 4.14)

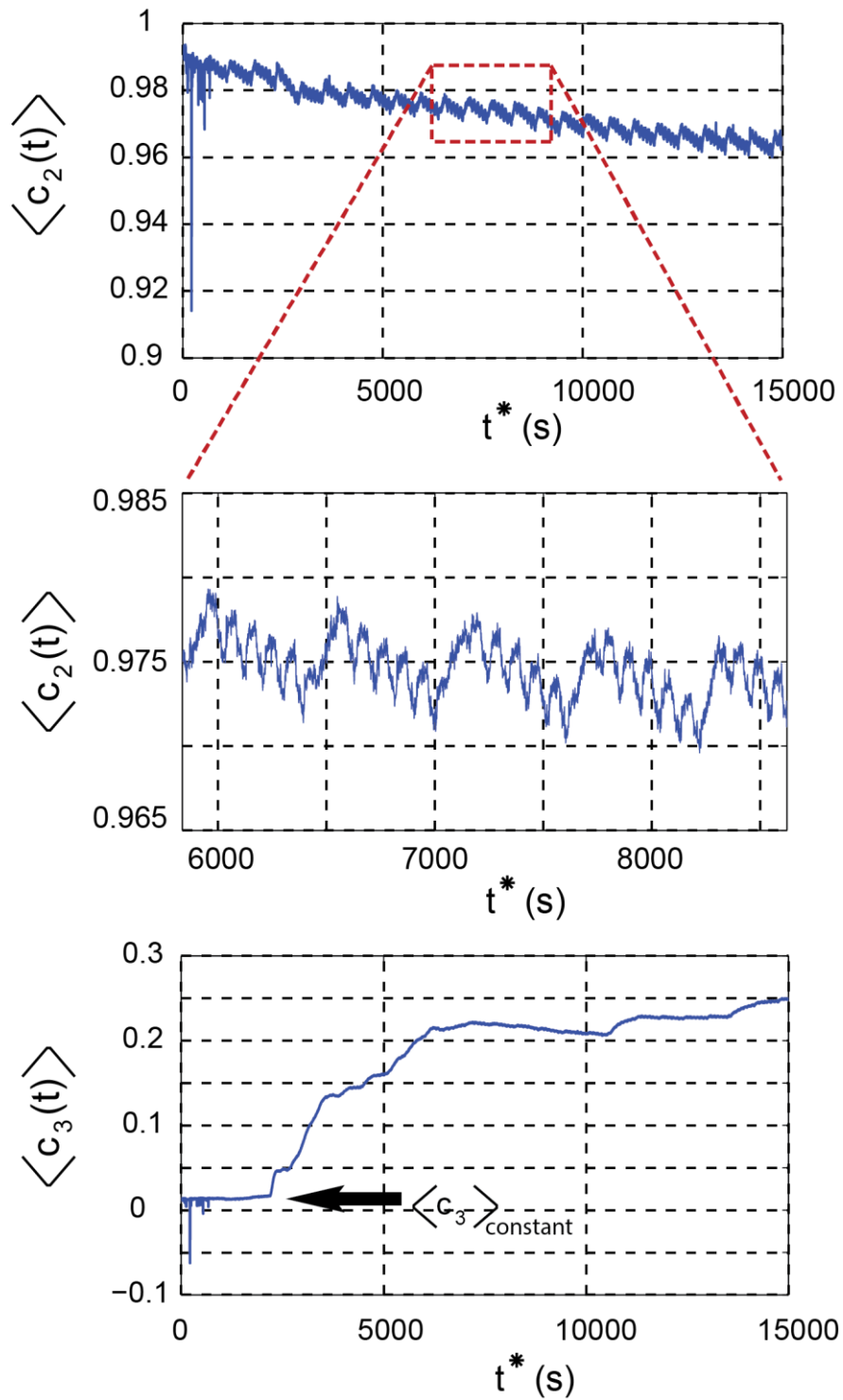


Figure 4.14 (a) mean concentration over region 2; $\langle c_2(t) \rangle$ (b) a focused view of $\langle c_2(t) \rangle$ demonstrating its periodic behavior, (c) mean concentration over region 3; $\langle c_3(t) \rangle$

Chapter 5: Quantitative concentration measurement in narrow channels

5.1 Result and Discussion

Challenges associated with performing quantitative particle image velocimetry (PIV) and LED-induced fluorescence (LIF) in thin gap channels were discussed in details in previous chapters. In this chapter, the results for a simultaneous velocity and concentration measurement for Rayleigh-Bénard convection in a Hele-Shaw cell are discussed in further detail. Specifics of the experimental setup were covered in the previous chapter, a simple schematic of the experimental setup is presented here in figure 5.1.

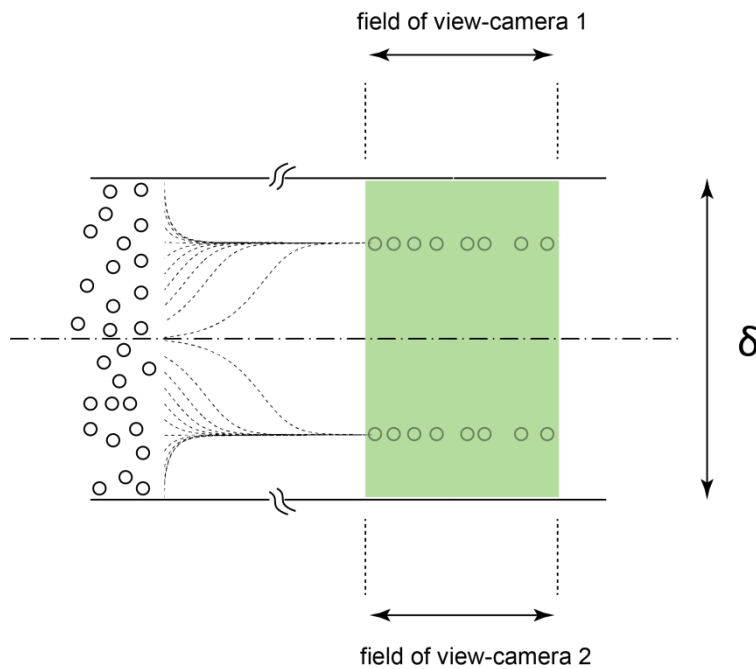


Figure 5.1 a focused view of the Hele shaw cell cross section. The microspheres are manipulated to a known location across the gap before reaching to the field of view

Figure 5.2 shows a snapshot of images from both velocity and concentration cameras at $t^*=1000$ s or using the scaled time of $t=1.45$ using equation 1.9. Due to the in line positions of the cameras facing each other, the corresponding images from the two cameras are reversed. As explained in previous chapters, a simultaneous velocity and concentration measurement of a determined region of the device can lead to estimations of the flux from the top layer to the bottom layer ($\vec{J} = \vec{J}_{convection} + \vec{J}_{diffusion} = \vec{u}c - D\nabla c$). There are two printed vertical lines on one of the glass walls with a distance of 70 mm used for determining the region of interest of the flow pattern. This region is defined far enough from the inlets to ensure a sufficient development length required for particle manipulation (L). The lines are printed on the outer side of the glass so they don't interfere with the flow (due to change in surface energies, implementing the lines in contact with the flow resulted in formation of bubbles on the lines). Although field-of-view of both cameras include the designated area between the vertical lines but since each camera was calibrated separately, they were not perfectly aligned and did not share a common optical axis. Subsequently, one further processing step and determining a transformation procedure was needed to match each pixel on the images from camera 1 with the corresponding pixel on the image taken from camera 2 at each time. The transformation consists of a linear magnification, a planar translation and a planar rotation. Figure 5.2 b and c demonstrates the combined images to report a well matched pattern.

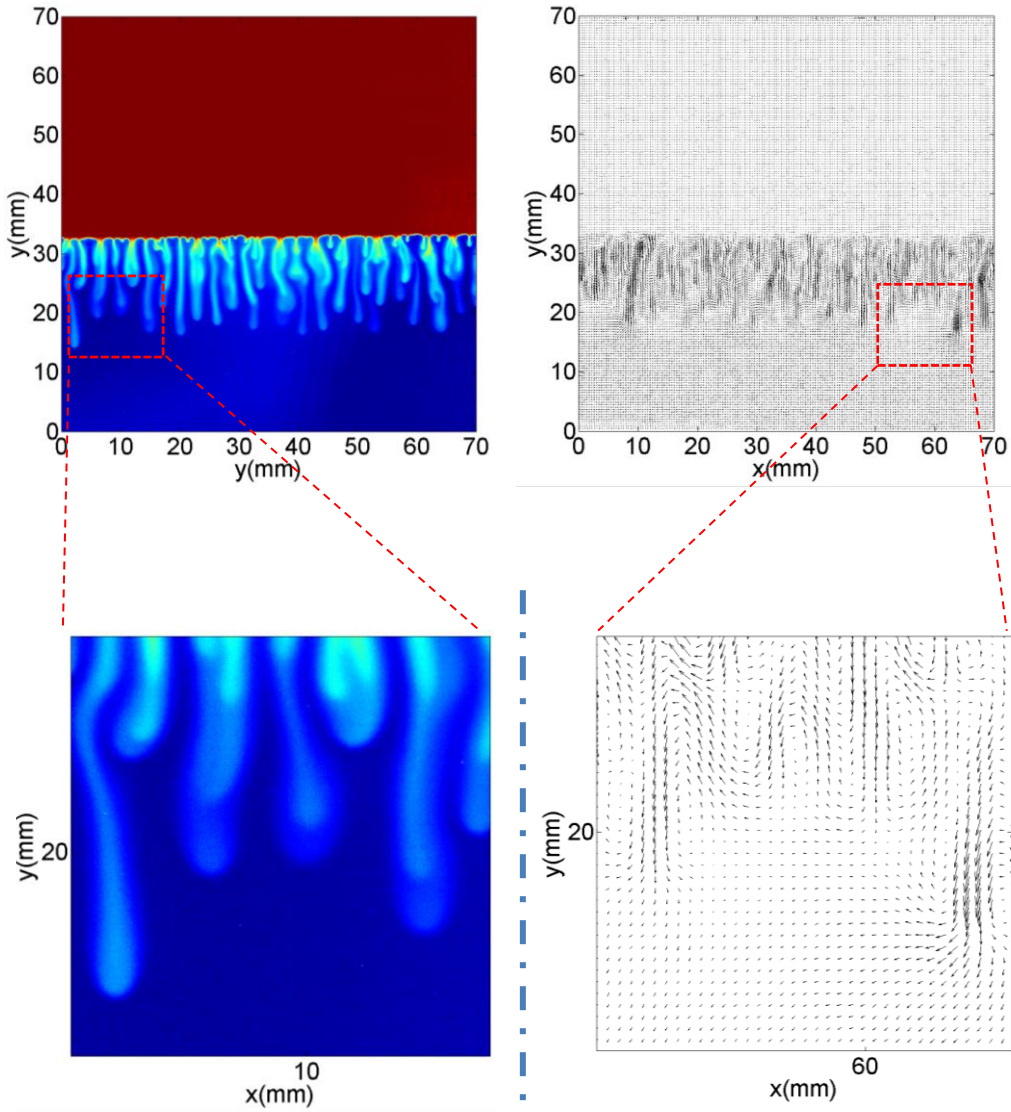


Figure 5.2 calculated velocity and concentration from processing recorded images from camera 1 and 2 respectively

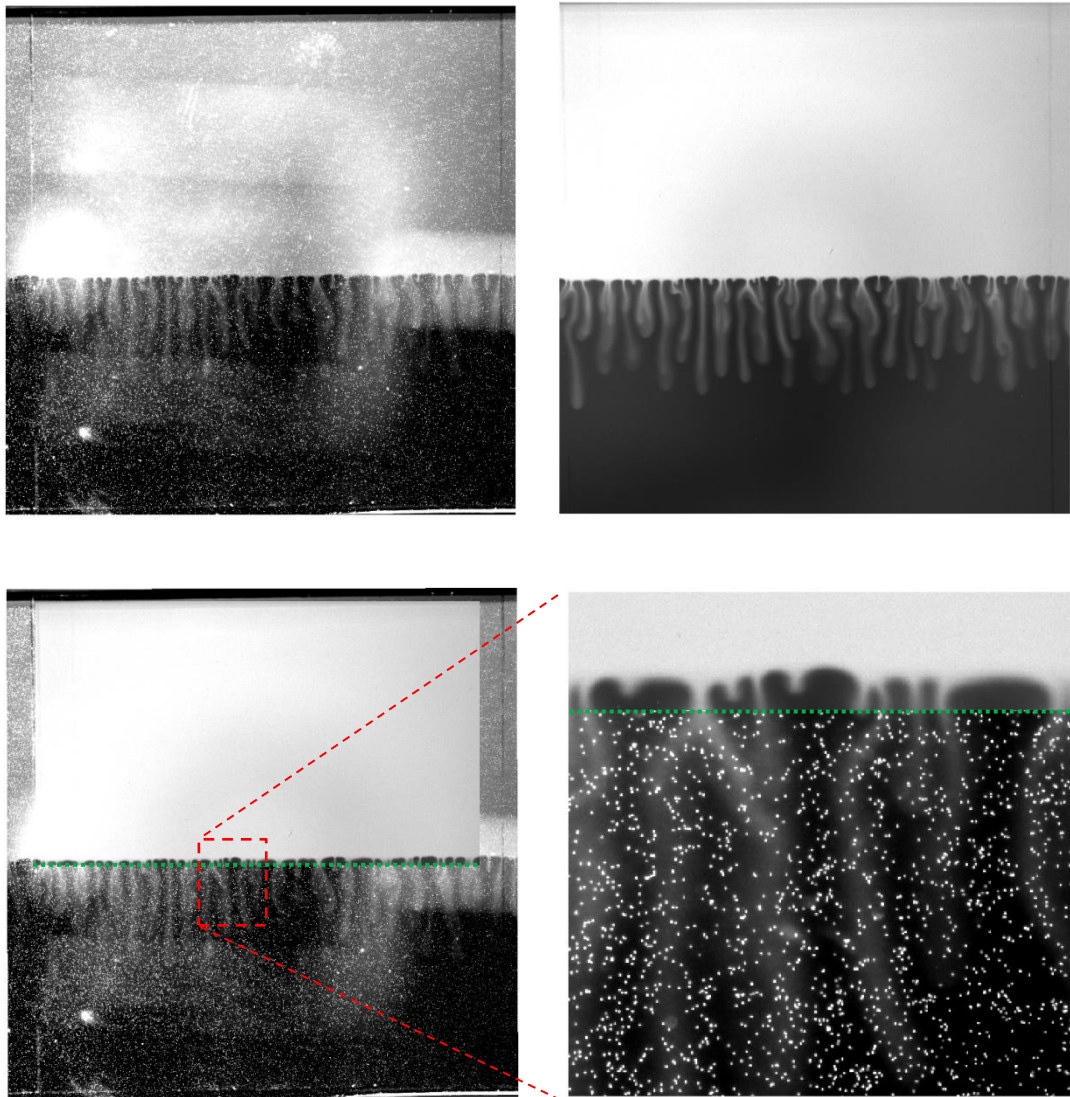


Figure 5.3 mapping raw images from camera 1 to corresponding images taken from camera 2 after transformation

In the figure series 5.3, the estimated concentration field is presented for different time scales to investigate the flow behavior at different regimes. As discussed in the previous chapter concentration field is a value from 0 where there is water to 1 where there is pure MEG. To track instability plumes, a region of the flow where there are instability fingers was determined by defining a concentration

threshold values e ($0.2 < c_f < 0.8$). It should be noted that all the variables are non-dimensionalized with the scaling parameters as discussed in chapter 1. Important scaling parameter values are as follows:

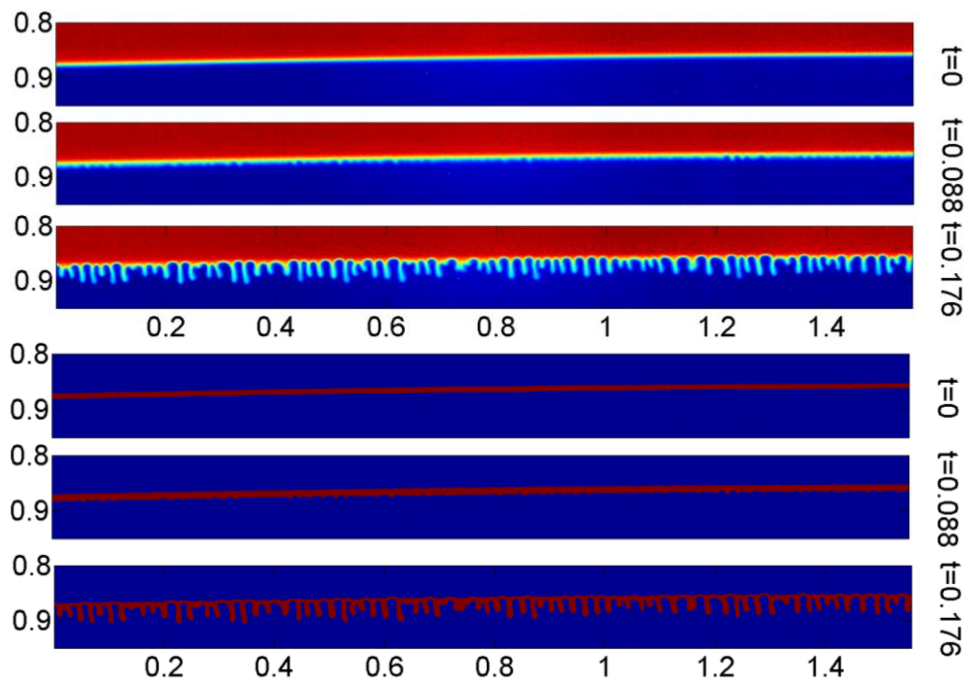
Experimental parameters	
H	0.045 m
t'	682.57 s
Ra	2472.3
Ra_δ	3

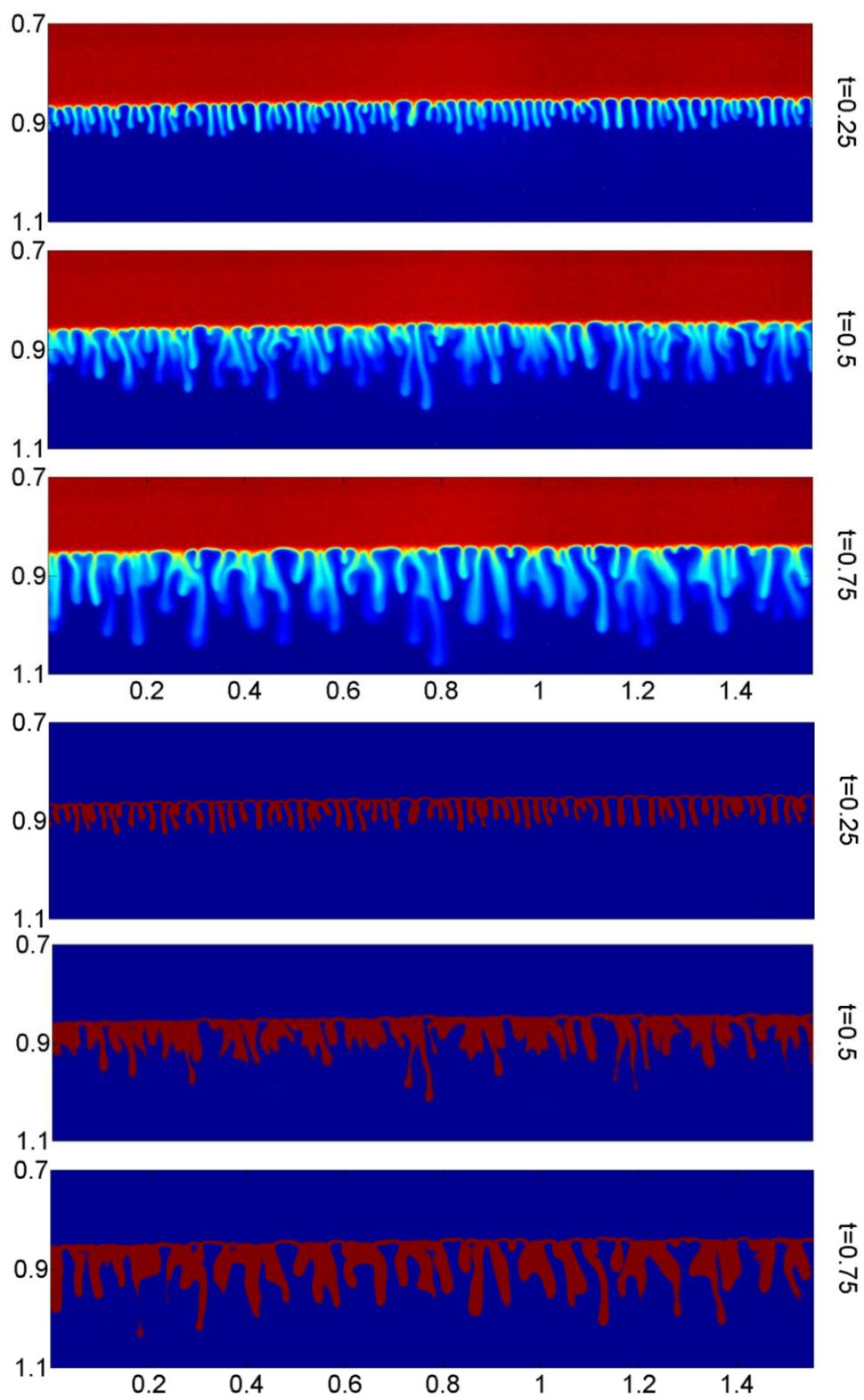
Table 5.1 experimental parameters

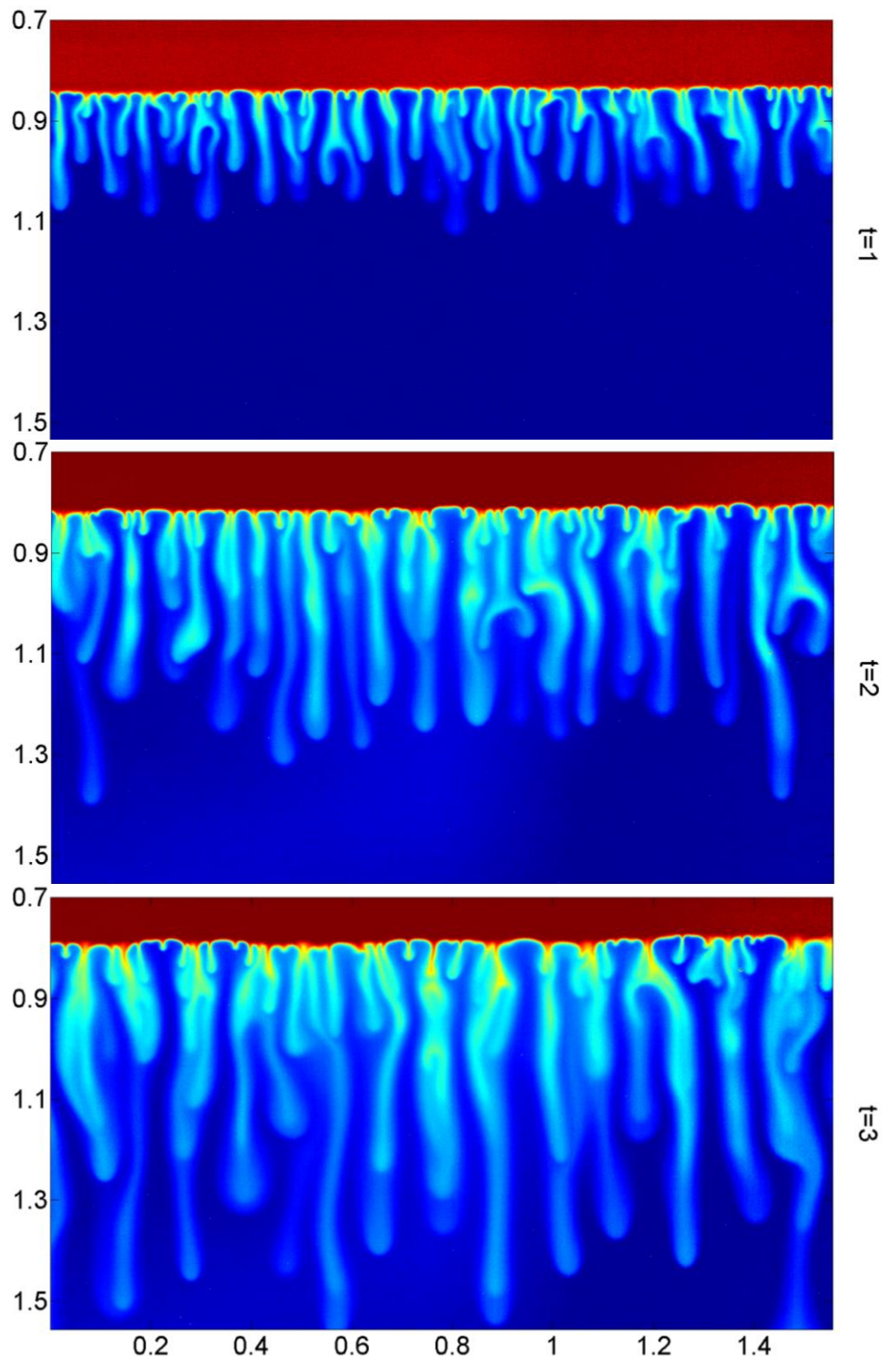
The experiment starts with a sharp interface at $t=0$. As the top column diffuses into the water, the boundary layer becomes thicker until it reaches to a point where it becomes unstable and instability plumes in the form of fingers start to propagate downward. From the analytical work of Riaz et al (2006), the critical time is estimated to be around 4 seconds (equation 1.28), however in this work initial fingers are not observable before $t=0.088$ ($t^*=60$ s). The average wavelength of the fingers at $t=0.176$ ($t^*=120$ s) is close to 1 mm across the entire field-of-view. After some time, neighboring fingers tend to merge together and form thicker plumes ($t=0.5$). This is probably due to presence of stronger rising plumes and the existing vorticity pattern. After a while a new set of fingers start to develop at the interface ($t=0.75$) that become absorbed in existing fingers. The total number of fingers at the interface decreases continuously, for instance at $t=0.75$ ($t^*=510$ s) the average wavelength of fingers increases to about 1.63 mm. The number of fingers at different heights for a

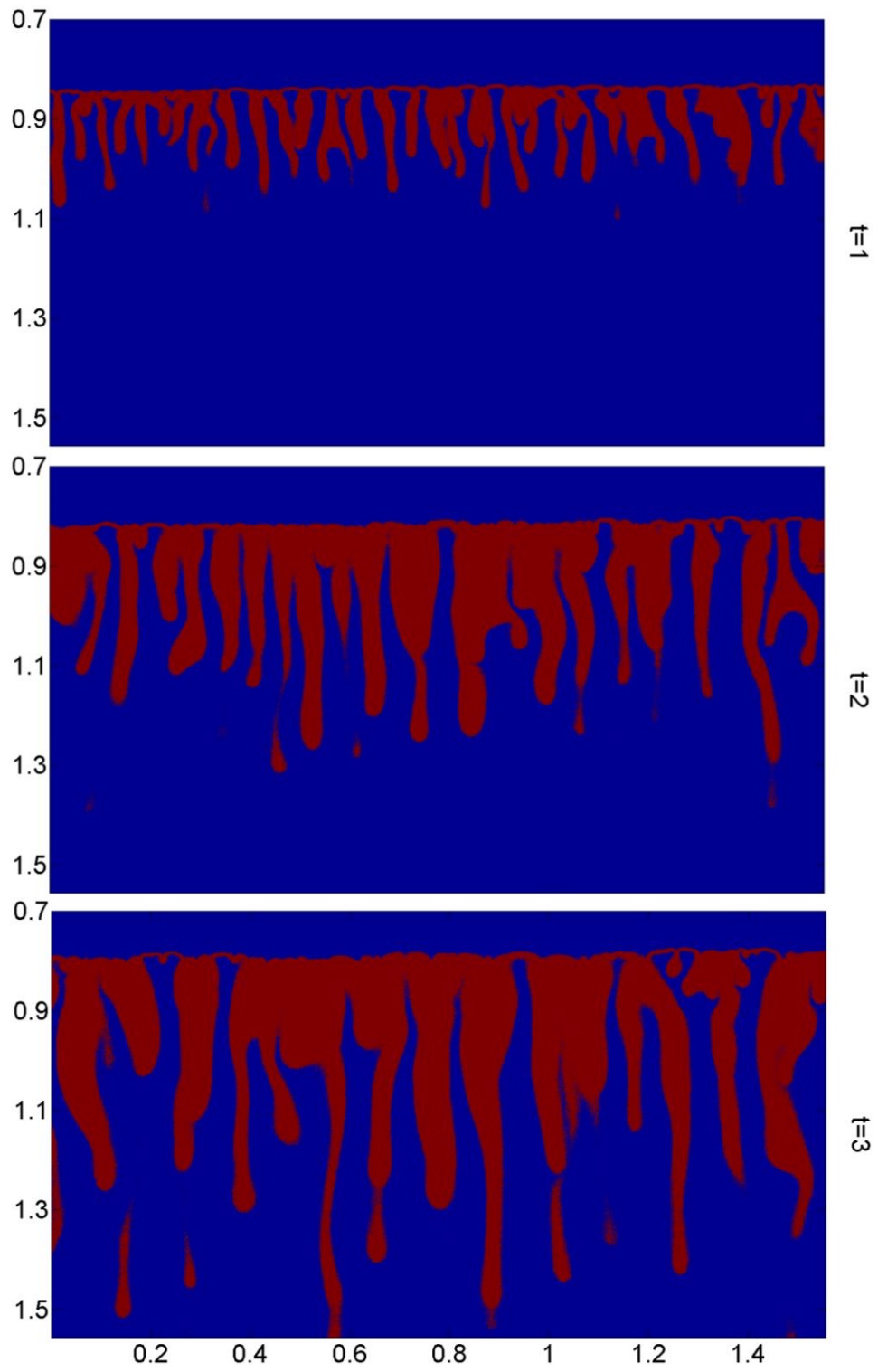
single time also decreases as they move further in the reservoir. At $t=3$ ($t^*=2045$ s), there are close to 30 fingers at the interface while this number at a distant 25 mm from the initial interface is around 15.

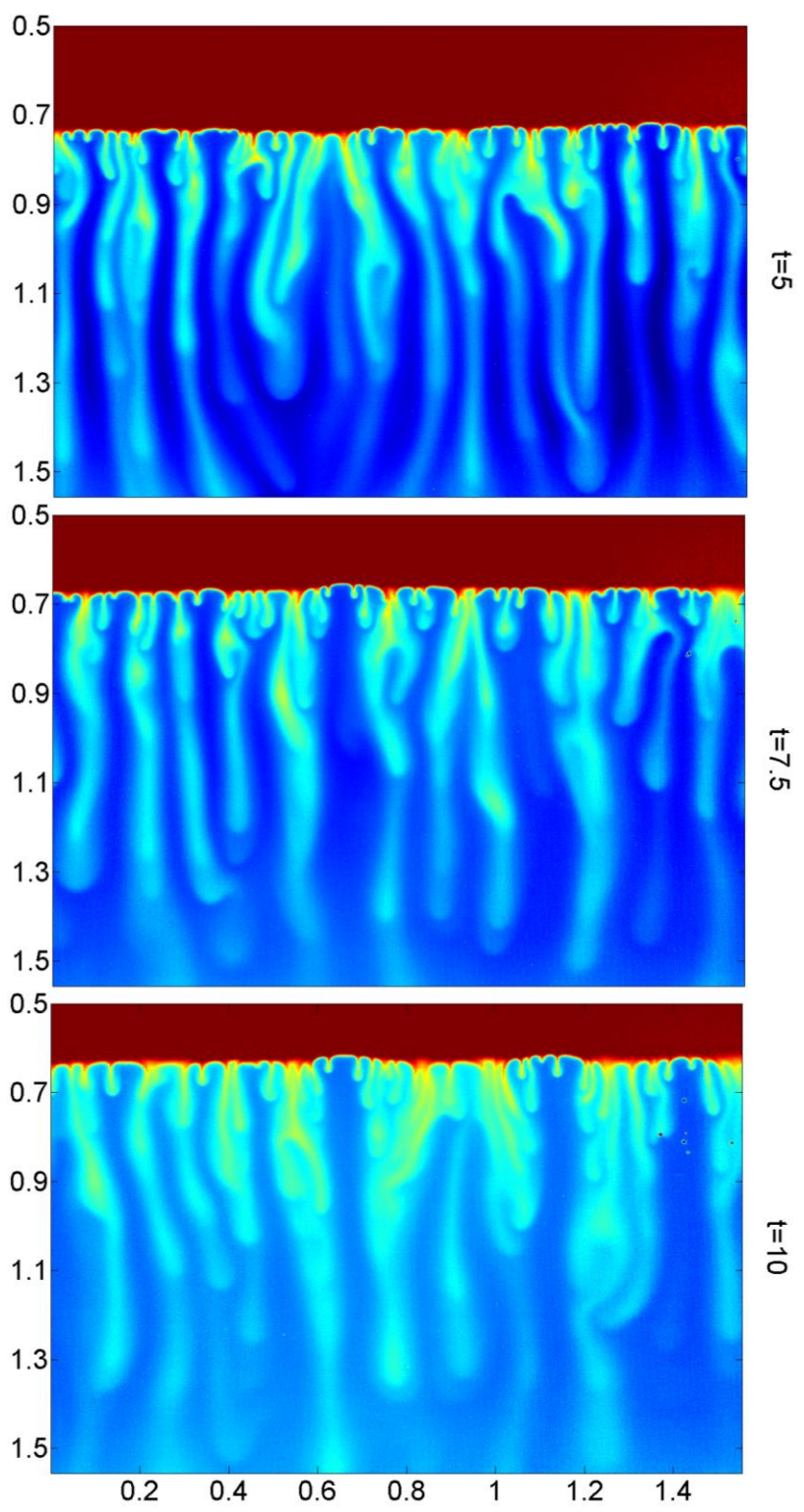
Newly developing fingers yield the existing flow pattern and are swept aside, eventually merging to the older descending streams. Although these streams are exceedingly dynamic close the interface, they are less active farther down. They mostly act as paths to transport MEG from the top layer to the bottom boundary. Fingers are usually wider at their tip comparing to their body and a few of them split at their tip on their way down as an ascending finger cuts through them. This is the case when the tip of the descending finger is not well defined and has a rift due to presence of multiple sub-fingers that previously joined together. Fingers reach the bottom boundary of the cell at about $t=5$ ($t^*=3413$ s) and after this point diluted MEG start to accumulate at the bottom while the dominant streams start to get thicker ($t=7.5$). The evolution of the fingers can be viewed in figure 5.3.

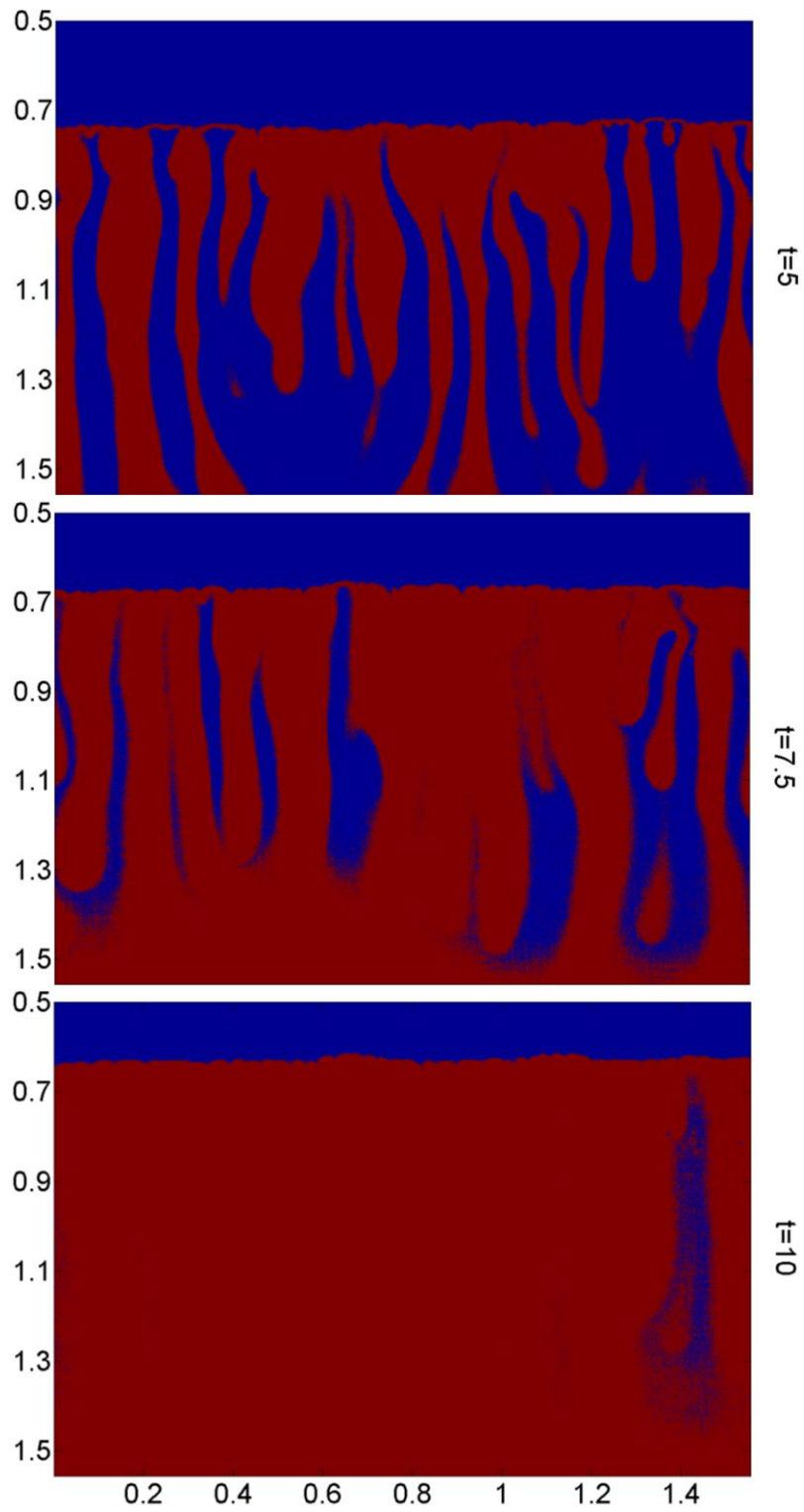












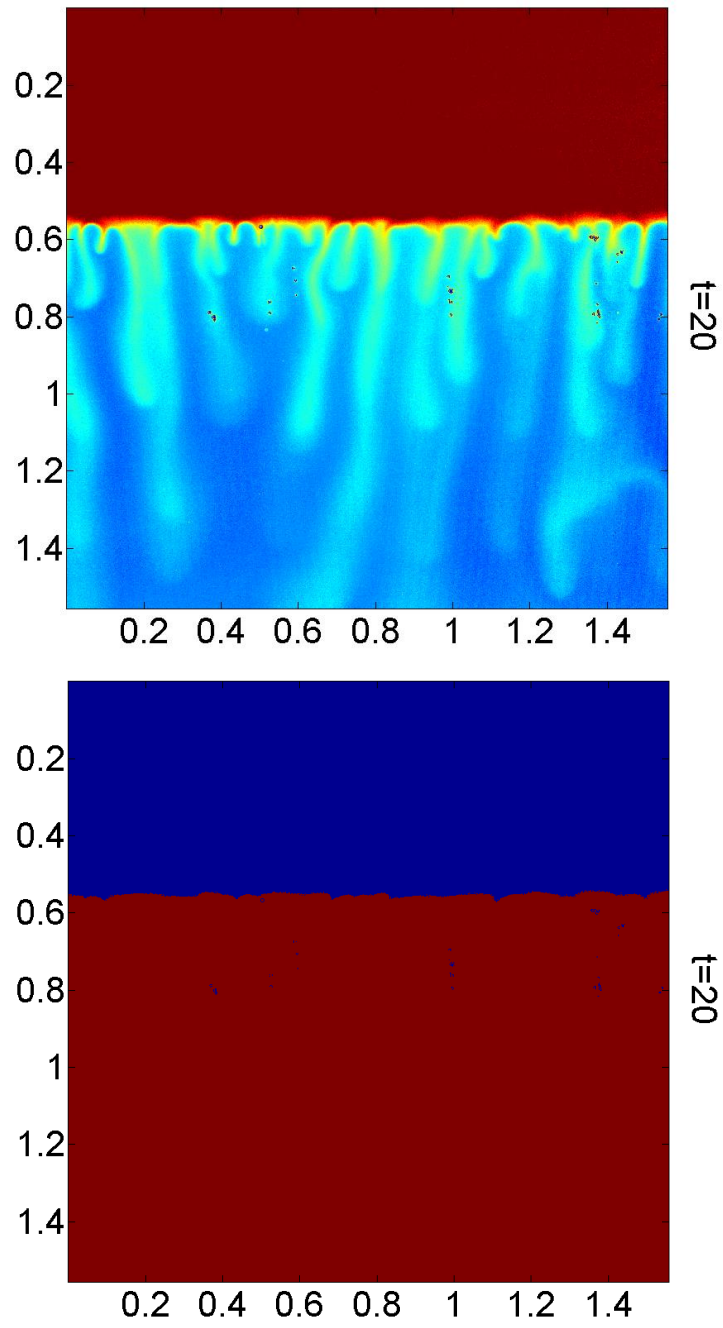


Figure 5.4 Rayleigh-Bénard flow evolution obtained from LIF concentration measurements

As the top layer mixes into the bottom column and pure MEG is consumed, the interface starts to recede from its initial position. By comparing the concentration field at $t=0$ and $t=20$, it can be observed that the interface has receded significantly. The distance between the two interface locations was measured to be around 13.5 mm. To be able to track the interface from the concentration field, a threshold value ($c_f=0.8$) was defined as mentioned earlier. In figure 5.5 the concentration profile from an arbitrary vertical line across the height of the entire field for a snapshot ($t^*=1000$ s) is shown, along with the level defining the interface position. Individual finger can be highlighted by subtracting the base profile from the extracted interface (a quadratic function fit to the elevation profile at each instant in time, giving the fluctuation of the interface about the spatial mean value). The evolution of generated fingers at the interface is presented in figures 5.5-5.6. As it can be observed, the number of fingers generated increases until $t\sim 8$, then fingers generation decelerates as system starts to saturate.

The amount of MEG descending into the reservoir can be determined by measuring the area A between the initial interface and the subsequent interface at a certain time. This value was then normalized by the reservoir height ($H=0.045$ m) and the length in which the fingers are being sampled ($L=0.07$ m). As it can be observed from figure 5.4, the amount of MEG being advected increases linearly until $t\sim 7$. At this time most of the dominant fingers have reached to the bottom of the cell while the front running fingers had reached the bottom boundary at about $t=3$. The flow rate can also be extracted from the interface retraction, figure 5.6 predicts a rise and fall of the flow rate. Flow rate Q^* is defined as:

$$Q^* = \int u_{\text{interface}} dx$$

5.1

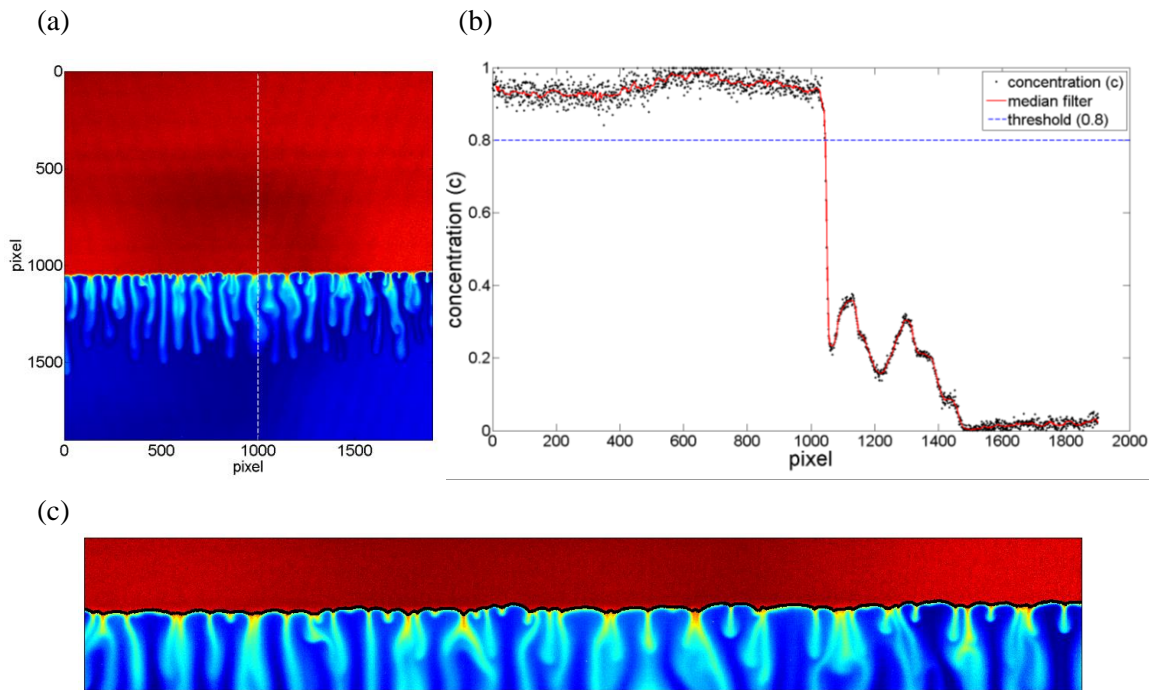
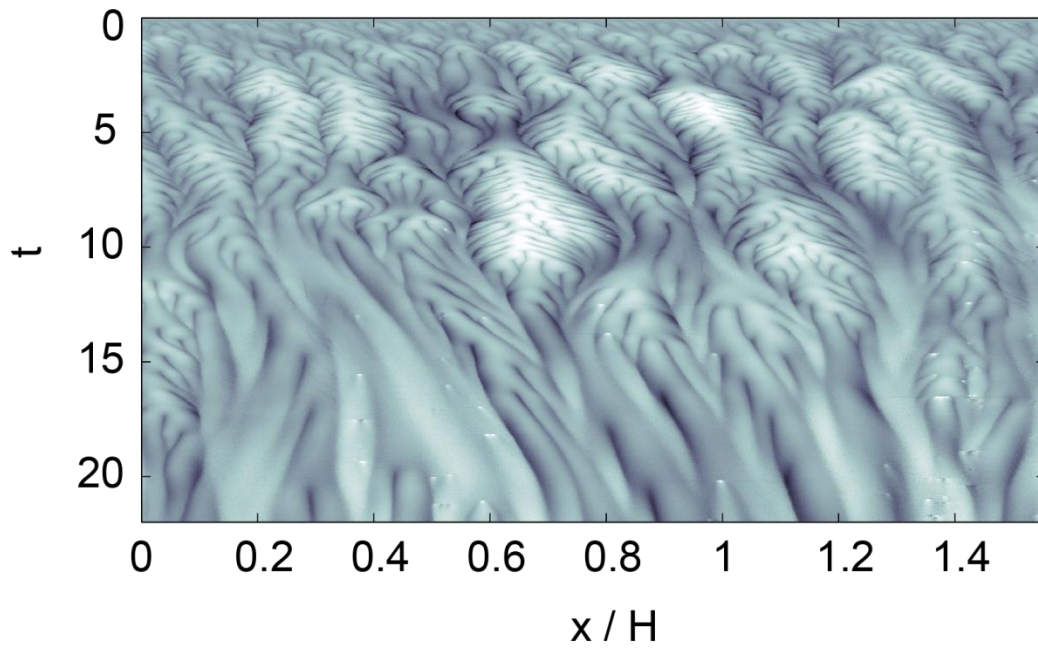


Figure 5.5 interface tracking by thresholding ($c_f=0.8$)



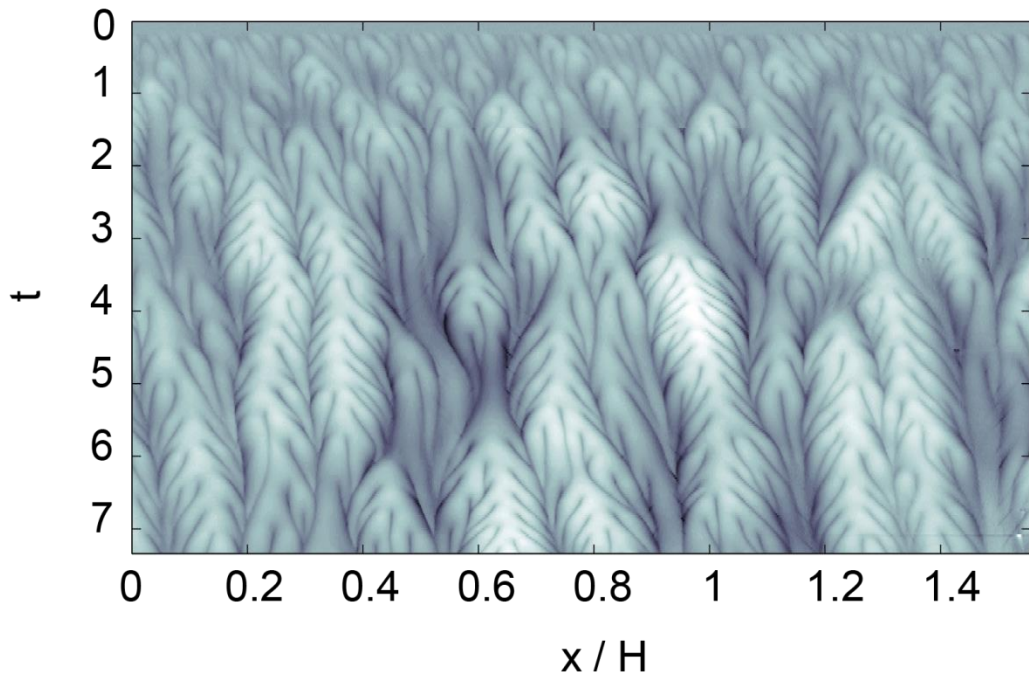


Figure 5.6 temporal fingers generation profile at the interface (a) ($0 < t < 22$) (b) ($0 < t < 7.5$)

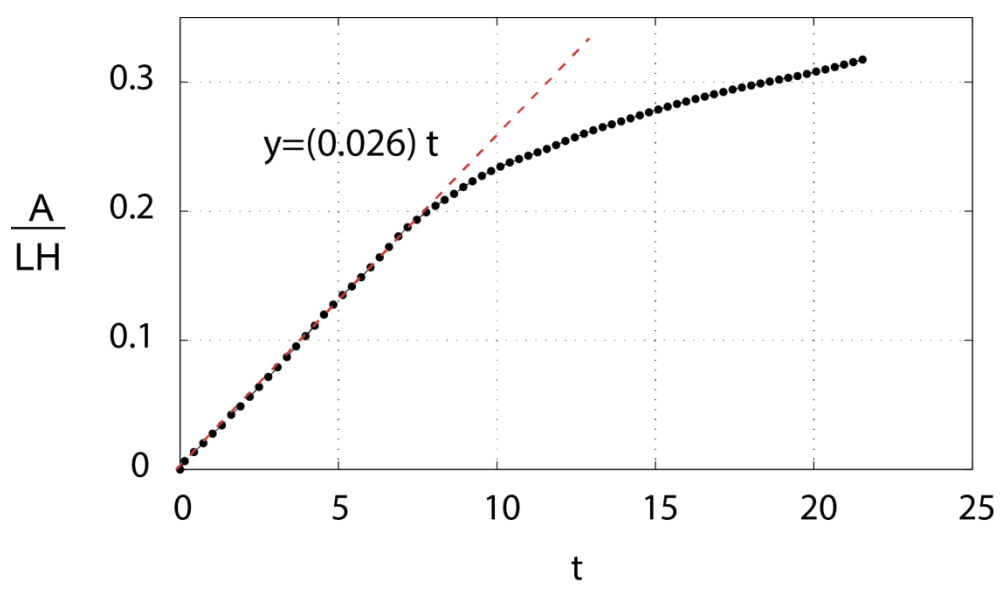


Figure 5.7 normalized amount of MEG convecting into the reservoir

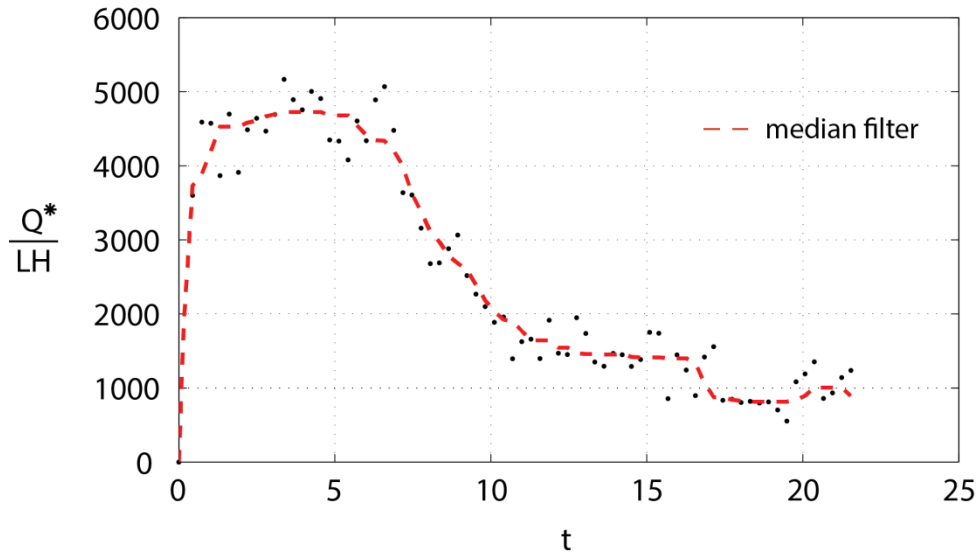


Figure 5.8 Normalized volumetric flow rate of the MEG convecting. The maximum rate of interface retraction reaches to $2 \mu\text{m/s}$

It should be noted that the mean velocity of the convective plumes remains so small that the effect of mechanical dispersion of the fluid components is negligible compared with molecular diffusion and the equations of motion and continuity covered in earlier chapter apply (according to Wooding et al (1960) [42] the condition $(2\delta u/k)^2 < 210$ needs to be met and we are well below this threshold in this study). The conditions in this study ensure In our case By taking the curl of equation 1.12, the pressure term can be eliminated to extract vorticity from the concentration field; equation 5.2 (vorticity is an important parameter in fluid mechanics that represents the angular velocity of fluid elements) [43]. On the other hand, the vorticity can be simply calculated independently from the measured velocity field. A snapshot of the vorticity field derived from the measured velocity and concentration field is

compared in figure 5.7. In the next step, the vorticity fields are used to extract information about the growth and propagation of instability plumes into the reservoir.

$$\omega = -\frac{\partial c}{\partial x} \quad 5.2$$

$$\omega = \frac{\partial u}{\partial x} + \frac{\partial v}{\partial y} \quad 5.3$$

$$\bar{\omega}(x, t) = \int_{y_0}^{y_1} \omega(x, y, t) dy \quad 5.4$$

$$\sqrt{E(\kappa, t)} = \int \bar{\omega}(x, t) e^{-i\kappa x} dx \quad 5.5$$

$$\hat{n} = \frac{\int_0^\kappa \kappa E(\kappa, t) d\kappa}{\int_0^\kappa E(\kappa, t) d\kappa} \quad 5.6$$

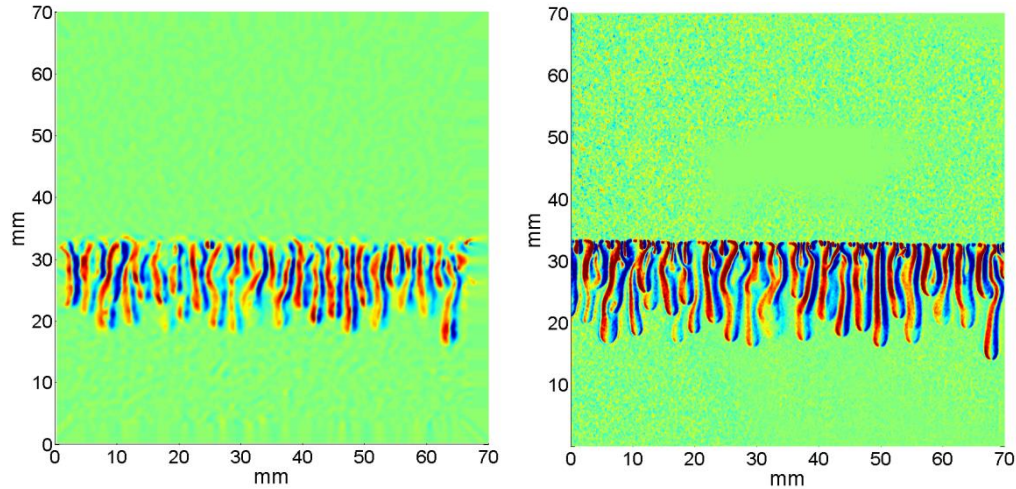


Figure 5.9 vorticity field extracted from velocity measurement (a) and concentration measurement (b) at $t^* = 1000$ s

At each vertical location y_1 , the dominant mode of instability can be extracted by taking Fourier transform of the vorticity $\omega(x, y_1, t)$ at each instant. The dominant wavenumber at each location along the reservoir (y) is demonstrated in figure 5.10.

Although this value converges to a constant rate for different heights below the interface but the wavenumber at the interface is higher and remains dynamic as new smaller fingers keep developing. In order to gain information about the finger growth and a general dominant mode for the entire domain, the average of vorticity is calculated $\bar{\omega}(x,t)$; equation 5.4 and the combined dominant wavenumber is determined from equations 5.6. In this equation $E(k,t)$ is the energy spectrum associated with Fourier transform of the averaged vorticity field. Normalized energy spectrum and dominant mode are demonstrated in figures 5.11 and 5.12. The results from vorticity field from concentration measurements (LIF) are compared with results obtained from vorticity fields extracted from velocity measurements (PIV). The results show similar spatial and temporal scales.

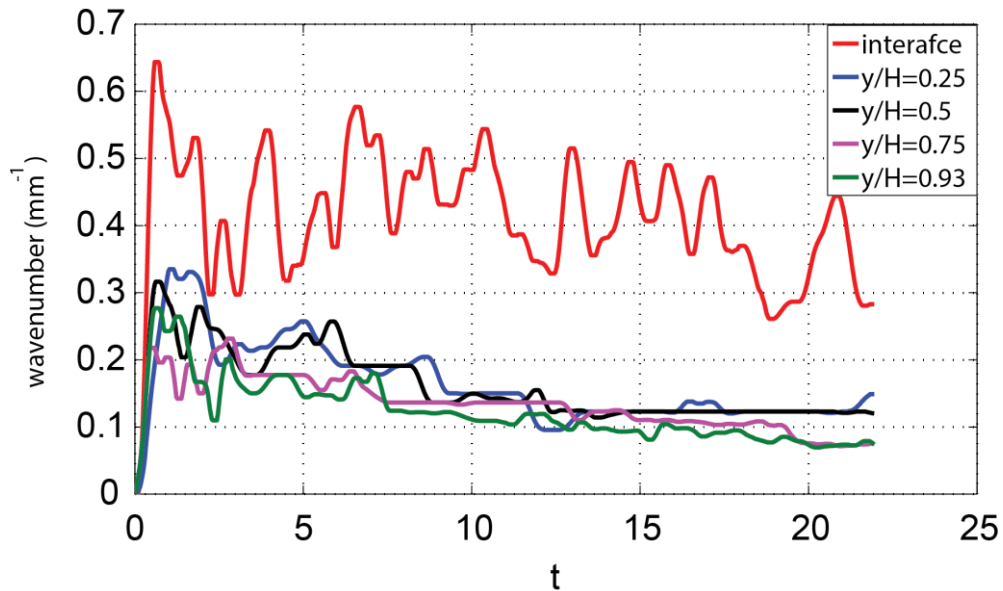


Figure 5.10 dominant wavenumber of the instability plumes at different heights (except the red curve that corresponds to the wavenumber at the interface all the other plots are associated with a fixed vertical positions down the reservoir)

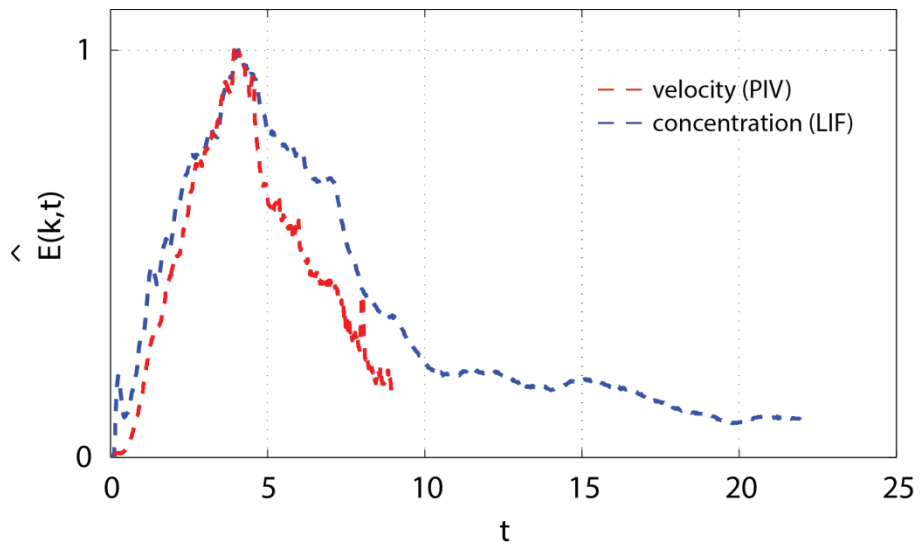


Figure 5.11 energy spectrum associated with Fourier transform of the averaged vorticity fields

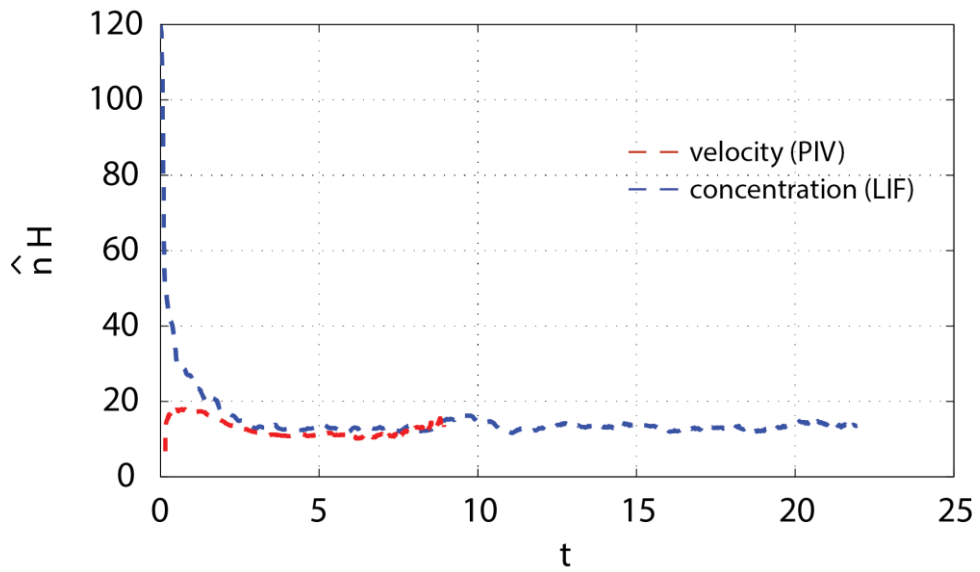


Figure 5.12 Combined dominant mode extracted from the averaged vorticity fields

Chapter 6: Final Thoughts

6.1 Conclusion

An experimental analogue was designed and fabricated to investigate the solute natural convection of a multicomponent fluid system in porous media. The analogue fluid used in the system contains the mixture of ethylene glycol and methanol (MEG) mixing with water. Porous media is also modeled with a vertical Hele Shaw cell that has a permeability of $\delta^2/12$ (δ is the gap thickness). Initially in a different but similar setup performing a large depth of field particle image velocimetry (PIV) in microfluidic systems and Hele Shaw cell was investigated in details. Performing planar laser induced fluorescence (PLIF) was then discussed to quantify the concentration field of the multicomponent convection within narrow channels and a Hele Shaw cell. The simultaneous velocity (PIV) and concentration measurement (LIF) can result in mixing quantification and convecting flux estimation.

Performing a large field of view PIV in a planar narrow device requires a large depth-of-field. If the depth-of-field is maintained larger than the gap thickness, tracer particles across the entire gap are mapped identically on the image plane, contributing equally to the PIV correlation peak. Although this measurement setup is straightforward comparing to micro-PIV implementations, but PIV interpretation in this case depends on the particle concentration distribution profile across the channel gap. If the induced inertial migration of tracer particles remains insignificant throughout the measurement, theoretically PIV correlation peak estimates the maximum displacement across the channel. However in practice, measurements are always impaired by an under-estimation due to smearing of the fluid displacement

PDF and particle image size. For an accurate measurement, this bias error that can be as significant as 33% of the maximum displacement needs to be quantified. Furthermore, due to a broad depth of correlation and large displacement variations in this case, low signal to noise ratio results in high occurrence of spurious displacement vectors. Although correlation averaging may be used to mitigate the issue for steady flows, low valid detection probability remains troublesome for more general transient flows.

In cases where particle migration becomes significant, due to an evolving sampling bias of the fluid displacement PDF across the gap, PIV displacement estimate becomes ambiguous. To perform an accurate measurement under these conditions, the concentration profile of particles across the channel must be identified. This stage can be skipped by changing the flow properties (increasing the effective x') and therefore manipulating particles to reach their equilibrium position prior to measurement. Downstream of this position, the correlation peak remains unchanged, with the peak location predicting a value close to the fluid velocity averaged across the gap ($U_{piv} = 0.64V_{max}$) for the case where $Re_c < 30$. For large Re_c , the equilibrium position will migrate closer to the wall, as noted in the previous work by Roudet et al. (2011) and according to the predictions of Asmolov (1999). This method is highly recommended for transient and spatially varying flows, since it allows for a high valid detection probability in interrogation regions without impractically large volume fraction of particles. However, measurement constraints and particular characteristics of each test setup must be taken into account to identify the most suitable measurement procedure to use for each case. For instance, for small

Peclet number particles, manipulation of the particles becomes cumbersome due to significance of Brownian motion (Pe expresses the relative importance of convection to diffusion). An appropriate seeding concentration should also be used since too high tracer volume fractions result in nonlinear effects as particles segregate, which might negatively affect the measurement accuracy. In the study of diffusive Rayleigh-Bénard convection in a Hele Shaw cell, appropriate parameter design can be used to provide a reliable quantitative measurement of the velocity field.

Due to the difficulties associated with manipulating the particles in both MEG and water columns, the flow pattern for only one Ra number was investigated. The densities of the two layers (MEG and water) are close, however the viscosities are different ($\rho_{\text{MEG}} = 972.5 \text{ kg/m}^3$, $\mu_{\text{MEG}} = 0.003 \text{ kg/m.s}$, $\rho_{\text{H}_2\text{O}} = 997.0 \text{ kg/m}^3$, $\mu_{\text{H}_2\text{O}} = 0.001 \text{ kg/m.s}$). The higher viscosity of the MEG layer required a greater flow rate to have the particles segregated within the required measurement location in the cell, when compared to particles in the water layer. Water flow rate was then set to produce a similar pressure drop in each liquid layer, which was required to maintain a straight interface between the two fluids. The settling velocities of the particles in each layer was still quite small (6.5 and 3.2 $\mu\text{m/s}$ in water and MEG, respectively), which is perceptible, but still significantly smaller than the convective velocities of the flow. The fluid timescales of the flow are on the order of 10 seconds, well below the response time of the particles, so inertial effects are completely unimportant. To minimize this effect neutrally buoyant particles were used in the experiment (Cospheric Inc. Polyethylene microspheres UVPMS-BG) with a density of 1000.1 (kg/m^3). Unfortunately their size variation was large ($\sigma \sim 4\mu\text{m}$) and was difficult to get

them segregated in the experimental setup. The result was a noisy data with a lot of outliers due to their distribution across the gap in the field of view.

Planar LED induced fluorescence (PLIF) uses light source suited to excite the fluorescent dye particles. In this work a known amount of Fluorescein sodium salt was added to MEG and was illuminated with a blue LED light source. The system was then calibrated to relate the detected fluorescence to concentration of the dye particles. The main difficulty of the method is light sensitivity and photobleaching effect for long durations. Correction methods were used to take into account these undesirable effects. The flow pattern from Rayleigh-Benard convective plumes were investigated after obtaining the temporal concentration field.

Condensed results and highlights of the velocity measurement by means of PIV are published in the journal of “Experiments of Fluids, 2014” [44] and were also presented in 10th international symposium on Particle Image Velocimetry [45]. The concentration measurement calibration and coupled results of PIV-LIF will be the subject of a future article.

6.2 Future work ideas

Results from simultaneous velocity and concentration fields can be combined to estimate the flux of MEG into the water column. This information can be used to quantify the fingers behavior along and also prediction of the convected flux in long durations comparable to time scale of the solution trapping in actual reservoirs.

In the Hele-Shaw cell geometry, as discussed in previous chapters, the effective permeability is constant everywhere due to a constant spatial gap thickness; $k_{ij}=\delta^2/12$ ($i, j=1, 2$). If the local gap thickness is now allowed to be a function of the two-dimensional space $\delta(x, y)$, the test cell can be given a variable permeability field. In the literature, most of the investigations have been conducted within a uniform cell gap thickness while porous medium in nature is seldom homogeneous and heterogeneity has a significant contribution to the behavior of the flow pattern observed. Toth et al. (2006) [46] performed experiments in a heterogeneous cell gap thickness pattern to investigate the density fingers propagation in the spatially modulated Hele shaw cell. They demonstrated experimentally that resonance amplification can take place if the imposed heterogeneity can amplify spatial modes with matching wave numbers. The idea of a variable permeability can be extended to the current work to quantify the concentration field through the calibrated LIF in a periodic heterogeneous permeability field. In the simplest case, this can be done through the use of modern rapid prototyping methods to fabricate and implement an extra piece into the current experimental setup (figure 6.1). A set of custom pieces can be produced that systematically vary the wavelength of the permeability both in one and two dimensions.

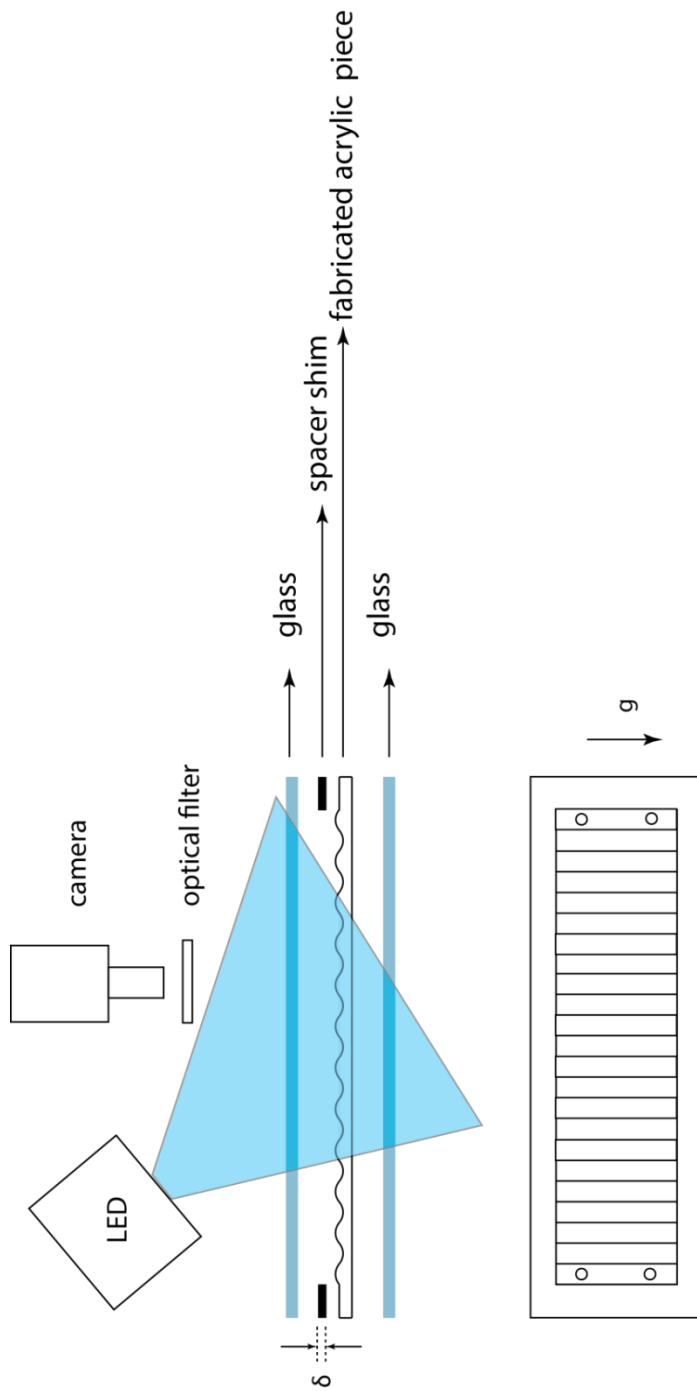


Figure 6.1 the proposed experimental setup to investigate the effect of a variable permeability

Appendix A



Bibliography

- [1] IPCC Special Report on Carbon Dioxide Capture and Storage; Technical summary
- [2] IPCC Special Report on Carbon Dioxide Capture and Storage; 2005
- [3] van der Meer, L. G. H. 1992 Investigations regarding the storage of carbon dioxide in aquifers in the Netherlands. *Energy Conserv. Mgmt* 33, 611–618
- [4] Ennis-King, J. & Paterson, L. 2003 Role of convective mixing in the long-term storage of carbon dioxide in deep saline formations. *SPE* 84344 pp. 1–12
- [5] Neufeld JA, Hesse MA, Riaz A, Hallworth MA, Tchelepi HA, Huppert HE (2010) Convective dissolution of carbon dioxide in saline aquifers. *Geophys Res Let* 37:L22404
- [6] Backhaus S, Turitsyn K, Ecke RE (2011) Convective instability and mass transport of diffusion layers in a Hele-Shaw geometry. *Phys Rev Let* 106(10), 104501:1-4
- [7] J. Ennis-King, I. Preston, and L. Paterson. Onset of convection in anisotropic porous media subject to a rapid change in boundary conditions. *Phys. Fluids*, 17:Article no. 084107, 2003
- [8] Riaz A, Hesse M, Tchelepi HA, Orr FM (2006) Onset of convection in a gravitationally unstable diffusive boundary layer in porous media. *J Fluid Mech* 548:87-111
- [9] Tilton N, Riaz A, (2014) Nonlinear stability of gravitationally unstable, transient, diffusive boundary layers in porous media. *J Fluid Mech* 745:251-278

- [10] P. Vennemann, K. T. Kiger, R. Lindken, B. C. W. Groenendijk, S. Stekelenburg-de Vos, T. L. M. ten Hagen, N. T. C. Ursem, R. E. Poelmann, J. Westerweel and B. P. Hierck, *Journal of Biomechanics*, 2006, 39, 1191–1200
- [11] Adrian RJ, Westerweel J (2011) *Particle Image Velocimetry*. Cambridge University Press, London
- [12] Santiago JG; Wereley ST; Meinhart CD; Beebe DJ; Adrian RJ(1998) A micro particle image velocimetry system. *Exp Fluids* 25: 316-319
- [13] Olsen MG, Adrian RJ (2000) Out-of-focus effects on particle image visibility and correlation in microscopic particle image velocimetry. *Exp Fluids*, [Suppl.] S166-S174
- [14] Kloosterman A, Poelma C, Westerweel J (2011) Flow rate estimation in large depth-of-field micro-PIV. *Exp Fluids* 50:1587-1599
- [15] Rossi M, Segura R, Cierpka C, Kähler CJ (2012) On the effect of particle image intensity and image preprocessing on the depth of correlation in micro-PIV. *Exp Fluids* 52:1063-1075
- [16] Segré G, Silberberg A (1962) Behaviour of macroscopic rigid spheres in Poiseuille flow: Part 2. Experimental results and interpretation. *J Fluid Mech* 14:136-157
- [17] Ho B, Leal L (1974) Inertial migration of rigid spheres in two-dimensional unidirectional flows. *J Fluid Mech* 65:365-400
- [18] Asmolov ES (1999) The inertial lift on a spherical particle in a plane Poiseuille flow at large channel Reynolds number. *J Fluid Mech* 381:63-87
- [19] Roudet M, Billet A-M, Risso F, Roig V (2011) PIV with volume lighting in a narrow cell: An efficient method to measure large velocity fields of rapidly varying flows. *Exp Them Fluid Sci* 35:1030-1037
- [20] Roig V, Roudet M, Risso F, Billet AM (2012) Dynamics of a high-Reynolds-number bubble rising within a thin gap. *J Fluid Mech* 707:444–466

- [21] Meinhart C D, Wereley S T and Santiago J G 1999 PIV measurements of a microchannel flow *Exp. Fluids* 27 414–19
- [22] Meinhart CD, Wereley ST, Santiago JG (2000) A PIV algorithm for estimating time-averaged velocity fields. *J Fluids Eng*, 122:285-289
- [23] Wereley ST, Whitacre I (2007) Particle dynamics in a dielectrophoretic microdevice. *BioMEMS and Biomedical Nanotechnology* (series ed. M. Ferrari): Vol. 4: Biomolecular Sensing, Processing and Analysis (vol. eds R. Bashir and S.T. Wereley), Kluwer, Boston
- [24] Meinhart CD, Wereley ST, Santiago JG (2000) A PIV algorithm for estimating time- averaged velocity fields. *J Fluids Eng*, 122:285-289
- [25] Fouras A, Dusting J, Lewis R and Hourigan K (2007) Three-dimensional synchrotron x-ray particle image velocimetry. *J Appl. Phys.*102:064916
- [26] Westerweel J (2000) Theoretical analysis of the measurement precision in particle image velocimetry. *Exp Fluids* 29:S3–S12
- [27] Keane RD, Adrian RJ (1992) Theory of cross-correlation analysis of PIV images. *Appl Sci Res* 49:191–215
- [28] Matas JP, Glezer V, Guazzelli E, Morris JF (2004) Trains of particles in finite-Reynolds-number pipe flow. *Phys. Fluids* 16:4192-4195
- [29] Mielnik MM, Saetran LR (2006) Selective seeding for micro-PIV. *Exp Fluids* 41:155-159
- [30] Cierpka C, Kahler CJ (2012) Particle imaging techniques for volumetric three-component (3D3C) velocity. *J Vis* 15:1–31
- [31] Fernandez J, Kurowski P, Petitjeans P, Meiburg E (2002) Density-driven unstable flows of miscible fluids in a Hele-Shaw cell. *J Fluid Mech* 451:239-260

- [32] Wieneke B, Pfeiffer K (2010) Adaptive PIV with variable interrogation window size and shape, 15th Int Symp App Laser Tech Fluid Mech, Lisbon, Portugal, July 5-8
- [33] B Hartline and C Lister. Thermal convection in a hele-shaw cell. *J. Fluid Mech.*, 79(2):379-389, Jan 1977
- [34] Walker DA (1987) A fluorescence technique for measurement of concentration in mixing liquids. *J Phys* 20: 217–24
- [35] Koochesfahani MM, Dimotakis PE. 1986. Mixing and chemical reactions in a turbulent liquid mixing layer. *J. Fluid Mech.*170:83–112
- [36] Ferrier, A. J., D. R. Funk, and P. J. W. Roberts. 1993. Application of optical techniques to the study of plumes in stratified fluids. *Dyn. Atmos. Oceans* 20: 155–183
- [37] Lakowicz, J. R. (1999) “Principles of Fluorescence Spectroscopy”, 2nd Ed. Lakowicz, J. R., ed), Plenum Press, NY
- [38] Guilbault, G. (1973). "Practical Fluorescence: Theory, Methods and Techniques," Dekker, New York
- [39] Ware B R (1983) Electrophoretic and frictional properties in complex media measured by laser light scattering and fluorescence photobleaching recovery
- [40] Z.J. Derlacki, A.J. Eastal, A.V.J. Edge, L.A. Woolf, Z. Roksandic, Diffusion coefficients of methanol and water and the mutual diffusion coefficient in methanol–water solutions at 278 and 298 K, *J. Phys. Chem.* 89 (1985) 5318–5322
- [41] Ternstrom, G., Sjostrand, A., Aly, G., & Jernqvist, A. (1996). Mutual diffusion coefficients of water+ethylene glycol and water+glycerol mixtures. *Journal of Chemical and Engineering Data*, 41(4), 876–879

- [42] Wooding, R.A., 1960. Instability of a viscous liquid of variable density in a vertical Hele-Shaw cell. *J. Fluid Mech.* 7, 501–515
- [43] G. K. Batchelor, *An Introduction to Fluid Dynamics*, Cambridge University Press, Cambridge, 1967
- [44] Ehyaei D., Kiger K. (2014) Quantitative velocity measurement in thin gap Poiseuille flows. *Exp Fluids* (2014) 55:1706
- [45] Ehyaei D., Kiger K. Quantitative velocity measurement in thin-gap Poiseuille flows, PIV13; 10th International Symposium on Particle Image Velocimetry, Delft, The Netherlands, July 1-3, 2013
- [46] D. Horváth, T. Tóth, Á. Tóth, (2006), Density fingering in spatially modulated Hele-Shaw cells. *Phys. Rev. Lett.* 97